Vibration Damping using Low-Wave-Speed Media with Applications to Precision Machines

by

Kripa K. Varanasi

B.Tech., Indian Institute of Technology Madras, 1998
M.S., Mechanical Engineering
Massachusetts Institute of Technology, Cambridge, 2002
M.S., Electrical Engineering and Computer Science
Massachusetts Institute of Technology, Cambridge, 2002

submitted to the Department of Mechanical Engineering
in partial fulfillment of the requirements for the degree of
Doctor of Philosophy in Mechanical Engineering

at the

MASSACHUSETTS INSTITUTE OF TECHNOLOGY
June 2004

Author _____
Department of Mechanical Engineering
May 8, 2004

Certified by _____
Samir A. Nayfeh
Assistant Pr ing

Accepted by _____
min
Chairman, Department Committee on Graduate Students

Vibration Damping using Low-Wave-Speed Media with Applications to Precision Machines

by

Kripa K. Varanasi

submitted to the Department of Mechanical Engineering
on May 8, 2004 in partial fulfillment of the requirements for the
degree of Doctor of Philosophy in Mechanical Engineering

Abstract

Vibration and noise are an ever-present problem in the majority of mechanical systems, from consumer products to precision manufacturing systems. But most approaches for vibration suppression are expensive and invasive, so only a small subset of the techniques developed in research labs are widely used.

In this thesis, we present a novel wave-based damping approach for the suppression of vibration in machines and structures. Our studies show that significant broad-band damping can be attained with little added mass via dynamic interaction between a structure and a low-density, low-wave-speed medium (such as a foam or powder). This damping phenomenon has great promise for many applications because it is robust (that is, not tuned), does not introduce significant creep into a structure, can accommodate large strains, and can be realized using materials that are light weight, low cost, durable, insensitive to temperature, and easy to package.

We report on several experiments in which flexural and longitudinal vibration are attenuated using this approach. Experiments on flexural vibration of structures filled with low-density powder show that high damping is obtained (with loss factors as high as 12 percent for a powder fill whose mass is 2.3 percent of that of the beam) over a broad frequency range. Somewhat surprisingly, the response is found to be linear over a wide range of amplitudes. We propose that the powder can be modeled as a fluid in which pressure waves can propagate and find that such a model matches the experiments well.

These findings suggest that any moderately lossy medium in which the speed of wave propagation is sufficiently low can be used to obtain similar

responses. We find that low-density foams coupled to structures exhibit comparable attenuations over a somewhat broader frequency range, and that the responses can be accurately predicted if dilatation and shear waves are included in the model.

We develop simplified models for these phenomena, and thence obtain guidelines for design of structures incorporating low-wave-speed media. The approach is compared to other damping techniques, and applications to belt-driven positioning systems and precision flexure assemblies are described.

Thesis Supervisor: Samir A. Nayfeh
Title: Assistant Professor of Mechanical Engineering

Thesis Committee:
Prof. Samir A. Nayfeh
Prof. Warren P. Seering
Prof. Alexander H. Slocum
Prof. David L. Trumper

ACKNOWLEDGMENT

I thank God for his constant guidance, support, help, and for everything he has given me.

I express my sincerest gratitude to my advisor Prof. Samir Nayfeh for his invaluable guidance, support, and encouragement. I consider it a great privilege to work with him. Samir is a dedicated teacher and is like an elder brother to me; motivating, instructing, and inspiring me to do my best. His creativity in practical design matters or theoretical formulations has always left me in awe. Through his own example, he has instilled in me the zeal for perfection and deep understanding. I have never met a person in my life who is as profound and as humble as he is. I am indeed indebted to him for all that he has done for me.

I thank my thesis committee members: Prof. Seering, Prof. Slocum, and Prof. Trumper for their invaluable guidance and support. I thank Prof. Trumper for taking a lot of interest in my work, reading through my thesis, and providing me several valuable inputs and suggestions. I have greatly benefited from my discussions with him over the past few years at MIT. He has helped me refine my ideas on mechatronics and feedback design. I am grateful to him for his instruction and advice. I thank Prof. Slocum for providing me with the energy, drive, and momentum during my Ph.D. Meeting him once would leave me with dozens of ideas and lots of excitement about my work. His inputs in the application parts of the thesis, especially the flexure chapter have been very useful. I am grateful to him for instilling in me curiosity, positive attitude, excitement, enthusiasm about research, and for all his advice. I thank Prof. Seering for asking me some really great questions on the modeling part of my work that led me to think deeper. His inputs on several part of the thesis have been valuable and I am grateful for his advice.

I am extremely grateful to Prof. Sanjay Sarma for all his help, encouragement, and advice. Sanjay's enthusiasm, and vibrant personality always motivates me to be at my best. I am grateful to Profs. Dahleh, Kong, Sonin, and Zahn for providing me with great education. Their lectures have always left me inspired and discussions with them were thoroughly enjoyable. I want to express my heart-felt thanks to my undergraduate advisor Prof. Ramamurti for instructing me on the design, dynamics, and control of machines.

The past few years in the lab has been a great experience, and the people here have made it so. I would like to thank my lab mates (in chronological order): Perry Banks, Andreas Athanassopolos, Paolo Morfino, Andrew Wilson, Lei Zuo, Pablo Valdivia, Nader Farzaneh, Greg Radighieri, Justin Verdirame, Mauricio Diaz, Dhanushkodi Mariappan, Jonathan Rohrs, Emily Warmann, Sappinandana Akamphon for their help and support. I thank Justin for his efforts in the initial experiments on granular materials, Andrew for helping me with all the computer-related issues, Lei for all the enlightening discussions, Dhanush for all the help in building the belt drive, and Mauricio and Jonathan for explaining to me the workings of the Bias Weaving Machine.

Next, I thank Mark Belanger, Gerry Wentworth, and Victor Lerman for their support in the LMP shop. I have learnt a lot from Mark and am grateful to him for his patient and thorough instruction. I want to thank Leslie Regan, Maureen Lynch, Maggie Sullivan, and David Rodriguera for all the help and support.

I thank Shorya Awtar, Mahadevan Balasubramaniam, Eberhard Bamberg, Perry Banks, David Chargin, Taejung Kim, Georgios Kotsalis, Elmer Lee, Stephen Ludwick, Rick Montesanti, Osamah El Rifai, Omar Roushdy, Sridevi Sarma, Pradeep Subrahmanyan, and Xiaodong Lu for their help and support. I thank Shorya and Jason for lending me their double-parallelogram flexure hardware to test my wave-based damping concept. I thank Rick for helping me with the compressed air and air bearing set up.

I thank my friends Ajay, Amit, Dhanush, Kishore, Krishnan, Jayant, Nishanth, Prahladh, Pavithra, Prashanti, Ramesh, Shorya, Shobhna, Sridhar, Sriram, Surana, Vijay, and Venkatesh for their wonderful company and support. I thank Ajay, Amit, Prahladh, and Pavithra for being such great friends and for all their help and support. Ajay is like a brother and a great companion. I thank Shorya and Shobhna for everything they have done for me.

Most of all, I thank my parents, Kanthi and Mohan Varanasi, and my sister Chandana Varanasi, for their constant love, support, and encouragement. Their affection, instruction, and inspiration have always provided me the means to excel and have given a direction to my life. I also want to thank my grandparents, aunts, uncles, and cousins for their constant support. Finally, I thank Manasa for her constant love and affection and for the joy, happiness, and excitement she has brought into my life.

Contents

List of Figures

List of Tables

Chapter 1

Introduction

The interplay between the kinetic and potential energies in a machine or structure gives rise to resonances in which the system undergoes large oscillations and possible instability. Damping is the dissipation of this energy; it limits the magnitude of vibration and improves the stability, performance, and life of a machine. Therefore the study of damping is essential for one who designs and builds machines. Moreover, damping plays a critical role in several areas such as motion control, vibration and noise suppression and isolation.

The energy dissipated in traditional materials of construction (such as steel, cast iron, or aluminum) is usually negligible (e.g., Lazan [27]) compared to that dissipated by micro-slip at material interfaces. This damping is difficult to predict and often varies with temperature, state of lubrication, surface conditions, assembly tolerances, and so on. But considerable performance gains can be achieved in many machines by introducing relatively high and predictable damping to meet dynamic-related specifications (e.g., Book [9]; Varanasi [51]). Hence in the present study, we develop methods to economically and robustly augment damping in machines.

1.1 Available Damping Treatments

Damping of vibration and noise has been an active area of research for many years. Broadly, damping treatments can be divided into two classes: active and passive. Active damping treatments usually employ piezoelectric actuators (e.g., Hagood *et.al.* [19]), electrorheological fluids (e.g., Kim *et.al.* [25]), magnetorhelogical fluids (e.g., Spencer *et.al.* [47]), electromagnetic actuators or others to provide a controlled force for vibration suppression. However, active methods are usually expensive and not robust unless they are used in conjunction with passive damping (e.g., Gueler *et.al* [18]).

Passive damping treatments usually incorporate one of the following: viscoelastic materials (e.g., Nashif *et.al.* [31]), passive piezoelectricity (e.g., Hagood and von Flowtow [20]), magnetic coupling, and tuned-mass dampers. Among these the most widely used damping method is the inducement of strain into viscoelastic materials (e.g., Johnson [22]; Nashif *et.al.* [31]). Several researcher in the past have studied this strain-based viscoelastic damping (e.g., Kerwin [24]; Ross *et.al.* [42]; Mead and Markus [30]; Torvik [50]). Most of these studies focus almost exclusively on the damping of bending vibration in one plane. Nayfeh [32] presents new methods for damping three-dimensional flexural and torsional vibrations of elastic-viscoelastic beams. Nayfeh and Varanasi [33] present analytical and experimental studies on damping of torsional vibration of slender thin-walled tubes with constrained-layer dampers. Nayfeh [32] and Varanasi and Nayfeh [52] partially constrain the usually freely floating end of a lead screw using a viscoelastic damper and thrust bearing to induce significant damping into drive resonance of lead-screw drives. Other references of interest in this area are Ruzicka [44] and Marsh and Slocum [29] which provide simplified analyses for design along with fabrication methods for internal shear dampers.

Some of the disadvantages of the viscoelastic damping are temperature sensitivity, material creep, and the cost of fabrication for constrained-layer dampers. There is a need for damping mechanisms that have the following favorable properties:

- lack of creep
- low cost
- durability

- light weight
- robustness (i.e., not tuned)
- insensitivity to temperature
- packaging ease
- accommodation of large strains

1.2 Wave-Based Damping Approach: An Overview

This novel damping approach is the subject of this thesis. It has the potential to satisfy most of the requirements described in the previous section: When a lossy low-wave-speed medium (such as powder or foam) is coupled to a vibrating structure, significant broadband damping can be achieved at low cost and without introducing creep. This damping phenomenon primarily occurs because of energy dissipation via the establishment of wave propogation in the low-wave-speed medium.

Damping using Low-Density Granular Media

Heavy structures (such as machine-tool bases) are sometimes filled with granular materials (such as sand, gravel, or lead shot) to increase their damping. Traditionally, relatively dense granular fills have been selected for such applications in order to obtain strong coupling between the structure and the granular material. But these high-density fills add significant mass to a structure and are not attractive where weight is a concern.

In Chapter 2, we show that, as originally studied by Fricke [17], a low-density fill can provide high damping of structural vibration if the speed of sound in the fill is sufficiently low. We describe a set of experiments in which aluminum beams are filled with a granular material whose total mass is 2.3% of that of the unfilled beam and damping coefficients as high as 6.0% are obtained. The experiments indicate that the damping is essentially a linear phenomenon. Next, we provide a simple model in which the powder is treated as a compressible fluid in which two-dimensional pressure waves can propagate and find that the model is in good agreement with experiments. Upon review of the literature, we find that the models developed in this chapter are the only

ones that can be used to quantitatively predict the damping that arises from coupling to low-density granular media. Next, we ask the question: Can this damping mechanism work with other low-wave-speed media? In Chapter 3, we document experiments on structures coupled to low-wave-speed foams and find similar damping behavior. This confirms that wave-based damping phenomenon is quite a universal phenomenon and can work with a variety of media.

Damping using Low-Wave-Speed Foams

In Chapter 3, we detail several experiments in which flexural vibration of aluminum beams is damped over a broad frequency range by the introduction of a layer of lossy low-wave-speed foam. Next, we provide a simple model for such vibration in which the foam is treated as a two-dimensional continuum in which waves of dilatation and distortion can propagate. Approximate solutions for the frequency response of the primary beam are obtained by means of a modal expansion, and the results are in close agreement with measured responses.

Next, we extend this approach to damp other forms of vibrations such as longitudinal waves in a rod and stretching of thin steel belts. We describe experiments in which longitudinal modes of a bar are damped when coupled to foam. Likewise, we find that significant damping can be introduced into the resonant mode arising from the stretching of a belt clamped to two masses (as shown in Figure 4.4) when foam is attached to the belt. Next models are presented in each case to explain the phenomena.

Simplified Models and Dimensional Analysis

Our studies in Chapters 2 and 3 show that the damping phenomenon can be adequately modeled by treating the damping medium as a continuum in which waves can propagate. However, these "full" (modal-expansion-based) models are too complicated to yield useful design formulas. Therefore, in Chapter 5, we develop simplified models and characterize the achievable damping in terms of key non-dimensional parameters of the system. To this end, we consider wave propagation in beam-foam or bar-foam systems of infinite extent and use energy and "complex-wave-number" approaches to obtain estimates for the loss factor.

Damping in Belt Drives

Flat steel belt drives are attractive for high-speed, high-acceleration, precision positioning systems because they can incorporate a drive reduction with low inertia and very smooth power transmission. But as the speeds of operation increase, the flexible dynamics of these drives poses important limitations on performance and stability. In Chapter 6, we use a layer of foam to enhance the dynamics of such systems.

Enhancing the Dynamics of Flexure Mechanisms

Flexures are typically used in applications such as kinematic mounts, and to provide smooth and precise motion. But it is very often found that such systems suffer from very lightly damped modes. In Chapter 7, we use foam to damp the vibratory modes of flexure assemblies in both the compliant and stiff directions. We demonstrate this method on single- and double-parallelogram flexure stages and provide guidelines for the design of these damping treatments.

1.3 Summary of Contributions

1. Novel wave-based damping mechanism: We document several experiments in which coupling a vibrating structure to a low-wave-speed medium results in significant broadband damping. We develop models that can accurately capture this phenomenon and provide design rules in terms of non-dimensional parameters of the system. Based on these studies, we conclude that the phenomenon can arise in any lossy material with sufficiently low speed of sound.

2. Low-density granular media: We develop a model and approximate solution that can be used to quantitatively predict the damping arising from the coupling of a structure to low-density granular media.

3. Methods to measure material properties: We have developed methods to measure the speed of sound, loss factor, and elastic moduli for the damping materials used in this work.

4. Applications to various types of vibration: We show that by "proper coupling" the method can be used to damp flexural and longitudinal waves and quasi-static stretching of a thin belt.

5. Enhancing belt-drive dynamics: We present a new method to damp longitudinal vibration of a flat steel belt drive by coupling the belt to foam. This method also damps the transverse modes of the belt thereby making it difficult to excite parametric resonances that can occur at high amplitudes.

6. Enhancing dynamics of flexure stages: We show that by coupling low-wave-speed foams to the flexure blades high damping can be introduced into several modes that can potentially destabilize controllers. This method is a very simple and low-cost approach to achieve significant performance gains in such mechanisms.

7. Combined acoustic and thermal shield and vibration damper: We present a new method in which a low-wave-speed medium covered with a thin aluminum or steel layer can shield a structure from acoustic and thermal radiation and at the same time damp structural vibrations.

CHAPTER 2

Damping Flexural Waves By Coupling to Low-Density Granular Media

2.1 Introduction

To improve dynamic performance, heavy structures are often filled with granular materials such as sand, gravel, lead shot, or steel balls. Traditionally, relatively dense granular fills have been selected for such applications in order to obtain strong coupling between the structure and the granular material. These "particle dampers" cost very little, and over years of trial-and-error use, have been observed to dissipate energy over a broad range of frequencies and temperatures. Several researchers in the past have studied the use of granular materials for vibration damping. Panossian [36, 37] carries out several experiments in which structures are filled with various types of particles (metallic, non-metallic, and even liquid particles) of various shapes and sizes at appropriate locations for attenuation of sound and vibration. Papalou and Masri [38, 39] and Fowler *et al.* [16] show that a container filled with granular material and coupled to a structure can be designed to achieve relatively high damping for a given added mass.

Based on extensive experimental results, Papalou and Masri develop an

approximate method to predict the damping attained by dampers filled with steel balls of various sizes [38, 39]. Fowler *et al.* employ a particle-dynamics simulation to model the behavior of a particle damper [16]. In these studies involving relatively large, high-density particles, the damping mechanism is strongly nonlinear because it is the result of impacts and sliding among the particles. As reported by Fowler *et al.* [16], little damping is obtained at very low amplitudes of vibration.

Cremer and Heckl [12] suggest that a granular material such as sand can be modeled as a continuum. According to their model, vibratory energy in the structure is transmitted into the granular material and dissipated within it. They also suggest that tuning the natural frequencies of a structure to those of the contained granular material will give greater damping coefficients. Sun *et al.* [48] model sand as a fluid and use statistical energy analysis to predict the damping in structures coupled to sand.

Richards and Lenzi [41] carry out several experiments on sand-filled tubes and study the influence of the quantity of sand, grain size, cavity shape and size, and the direction and amplitude of excitation. They report that damping attains a maximum at frequencies where resonances can be set up in the granular medium. Bourinet and Le Houédec [10] expand on the ideas of Cremer and Heckl and develop a quantitative model for the vibration of beams filled with granular materials. They model compressive waves in the granular material in the direction transverse to the vibration of the beam to develop an "apparent mass," which they couple to a Timoshenko beam. They present a numerical technique to solve for the dynamics of the coupled system and show that a great deal of damping can be attained at frequencies large enough to establish standing-wave resonances in the granular material. However, all of these prior studies deal with high-density fills that add a great deal of mass to a structure and hence are rarely used where weight is a concern.

Wave propagation and flow of granular materials has been an active research area for many years [21]. Nearly 175 years ago, Faraday studied the interaction between a vibrating body and a granular material and found that heavy particles move to the nodes of vibration, but light particles move to the antinodes [15]. Such low-density particles were found by Fricke [17] and Nayfeh *et.al.* [34] to produce relatively high damping if the speed of sound in the fill is sufficiently low. Further, Varanasi and Nayfeh [54] capture this damping phenomenon using a simple linear model.

In this chapter, we study the flexural dynamics of beams coupled to granu-

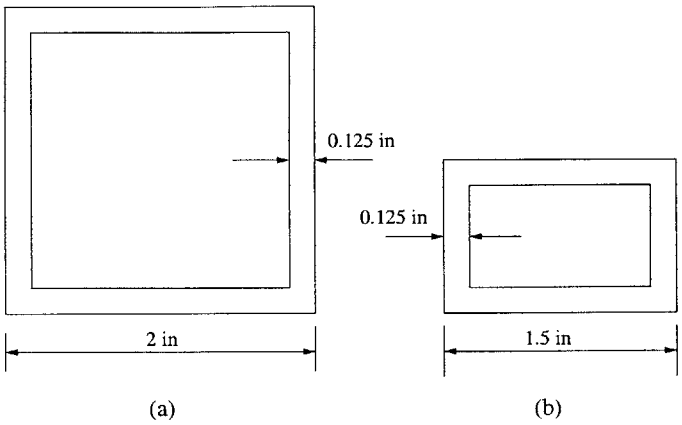

Figure 2.1: Cross section of aluminum box beams: (a) overall length of 28.25 inches, and (b) overall length of 72 inches.

lar material in which the speed of sound propagation is much lower than that in the beam. In Section 2.2, we report on experiments in which aluminum beams filled with low-density granular material exhibit significant damping (as high as 6%). Next, in Section 2.3, we develop a simple, linear model in which an Euler–Bernoulli beam is coupled to a granular material treated as a compressible fluid in which two-dimensional waves can propagate. Using the model developed in Section 2.3 and the properties of the powder (such as its speed of sound and loss factor) documented in the Appendix A, we obtain the accelerance (that is, the ratio of acceleration to force) of the beam under various boundary conditions. The results of the model are in agreement with the measured responses.

2.2 Experiments

This section describes experiments conducted on aluminum box and U-channel beams whose cross sections are sketched in Figures 2.1 and 2.2. The beams are filled with 3M Glass K1 Microbubbles (3M Corporation [2]). A photograph of the glass particles is shown in Figure 2.3 and that of a U-channel beam filled with such particles is shown in Figure 2.4. The average diameter of a particle is 65 microns, and the density of the powder is 140 kg/m^3. Because the speed of sound and loss factor of the powder are not precisely known, we conduct a

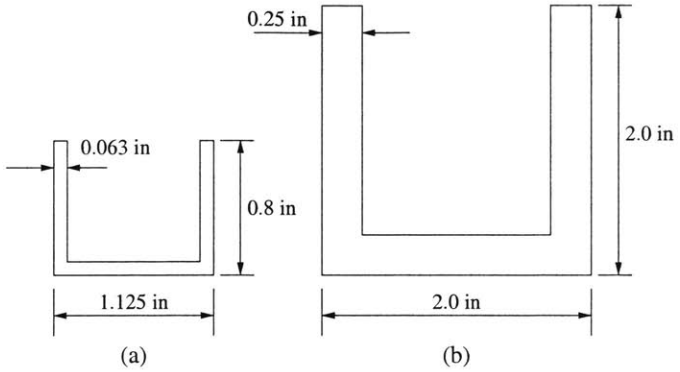

Figure 2.2: Cross section of U-channel aluminum beams: (a) overall length of 23.25 inches, and (b) overall length of 91 inches.

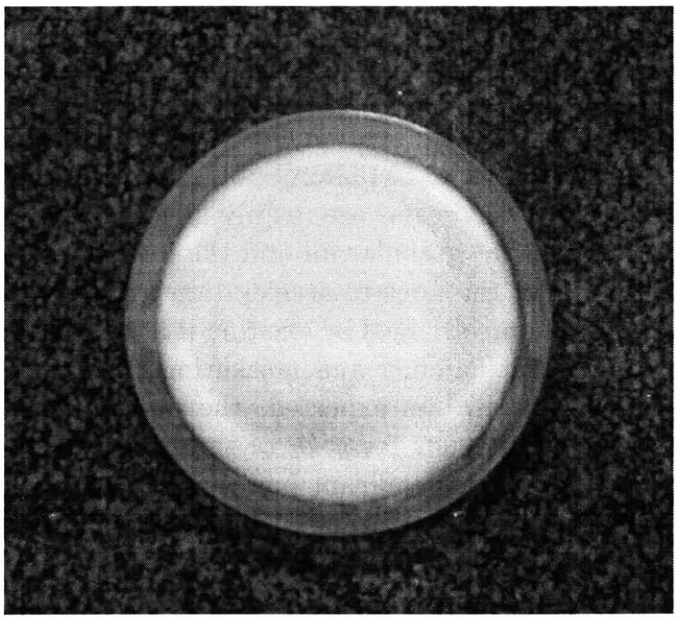

Figure 2.3: Photograph of the powder used in experiments

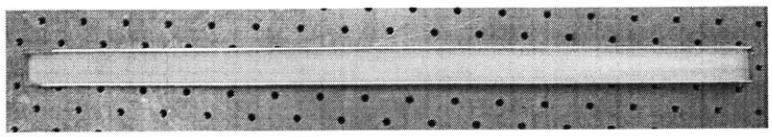

Figure 2.4: Photograph of a U-channel beam filled with powder

set of experiments to measure these properties (see Appendix A). From these measurements, we find that the speed of sound does not vary appreciably with the frequency and is approximately 58 m/s. Likewise, we find that the loss factor does not exhibit a strong dependence on frequency and is approximately 0.20.

In all of the experiments, the beams are suspended by soft elastic strings to simulate free-free boundary conditions. An impulsive excitation is provided by an impact hammer (PCB 333A30 [40]) at one end of the beam in the transverse direction, and the response is measured by an accelerometer (PCB 333A30 [40]) located at either the same or other end of the beam.

2.2.1 Box Beams

We present frequency-response measurements obtained from the box beams of Figure 2.1 filled completely with 3M Microbubbles. Due to the compressibility of the granular material, the beams are readily filled to an extent that no free surface remains between the granular fill and the interior of the beam wall.

In Figure 2.5, we plot the force-to-acceleration frequency response for the box beam of length 718 mm obtained by exciting it at one end in the transverse direction using an impact hammer and measuring the response at the same end using an accelerometer. As expected, the unfilled beam exhibits very little damping, with $\zeta < 0.0001$ for each of the first two modes. When the particles are added, we see a significant increase in damping in these modes. The effect on the first mode of the beam is more pronounced: A new mode has appeared, leading to behavior much like that of a tuned-mass damper. The critical damping ratios for the first three modes of the filled beam are found to be 0.04, 0.05, and 0.01, respectively.

Similarly, Figure 2.6 shows force-to-acceleration frequency response for the the box beam of length 1829 mm obtained by exciting it (in the transverse direction) at one end using an impact hammer and measuring the response at

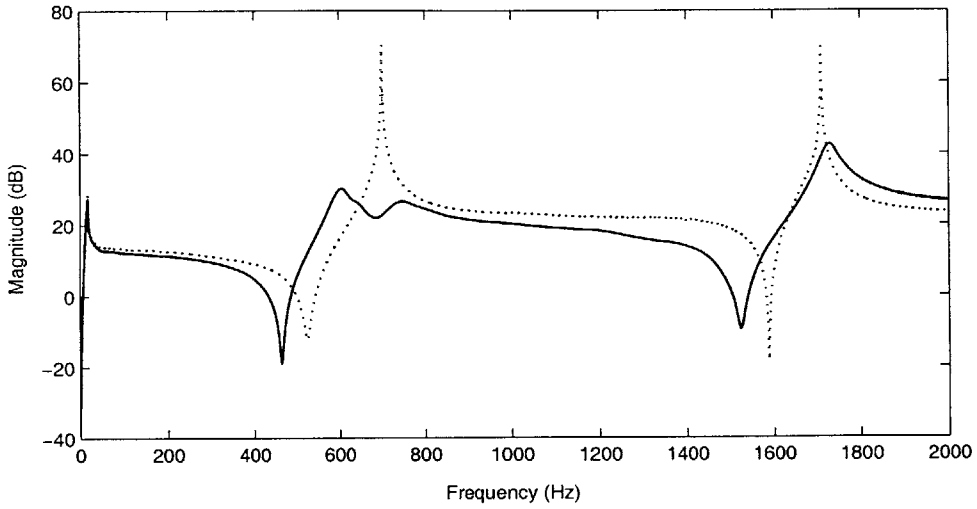

Figure 2.5: Measured force-to-acceleration frequency responses of the box beam of length 718 mm under hammer excitation: unfilled (dotted), filled (solid). The accelerometer and excitation locations are at the same end of the beam. The excitation and measurement are in the transverse direction.

the other end using an accelerometer. In this case the increase in damping is strongest from the seventh mode onward. The effect on the eighth and ninth modes of the beam is most pronounced, where a new mode has appeared with the addition of the powder, exhibiting behavior much like that of a tuned-mass damper. The attenuation decreases from modes ten to thirteen and then increase from thirteen to sixteen. This suggests that damping is strongest in frequency bands where standing waves can be set up through the thickness of powder.

2.2.2 U-channel Beams

A second set of experiments were conducted on the U-channel beams sketched in Figure 2.2 to ascertain the effects of a free surface and of variation in the thickness of the layer of granular material. In Figure 2.7, we plot the force-to-acceleration frequency response for the U-channel beam of length 591 mm obtained by exciting it at one end using an impact hammer and measuring the response at the same end using an accelerometer. The thickness of the granular

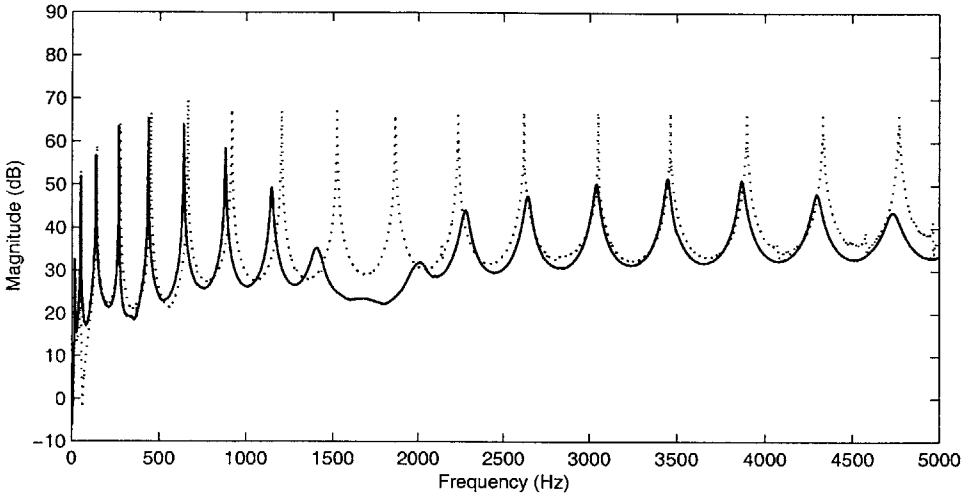

Figure 2.6: Measured force-to-acceleration frequency responses of the box beam of length 1829 mm under hammer excitation: unfilled (dotted), filled (solid). The accelerometer and excitation locations are at different ends of the beam. The excitation and measurement are in the transverse direction.

fill is 17 mm. As in the measurements on the short box beam, we find that the filled U-channel beam exhibits significant damping in each of its first two modes. In this case, the tuned-mass damper effect appears close to the second resonance of the beam. The critical damping ratios for the first three modes of the filled beam are found to be 0.005, 0.05, and 0.06, respectively.

Next, we study the effect of the variation in the thickness of the layer of the granular fill by exciting the U-channel beam of length 2311 mm at one end using an impact hammer and measuring the response at the other end using an accelerometer for granular fills of thicknesses 0.55", 0.90", and 1.55". Figures 2.8, 2.9, and 2.10 show plots of the corresponding force-to-acceleration transfer functions. As the thickness of the granular fill increases the damping at the lower modes improves. These measurements once again indicate that the damping arises from a strong interaction between the beam and powder via the establishment of standing waves in powder.

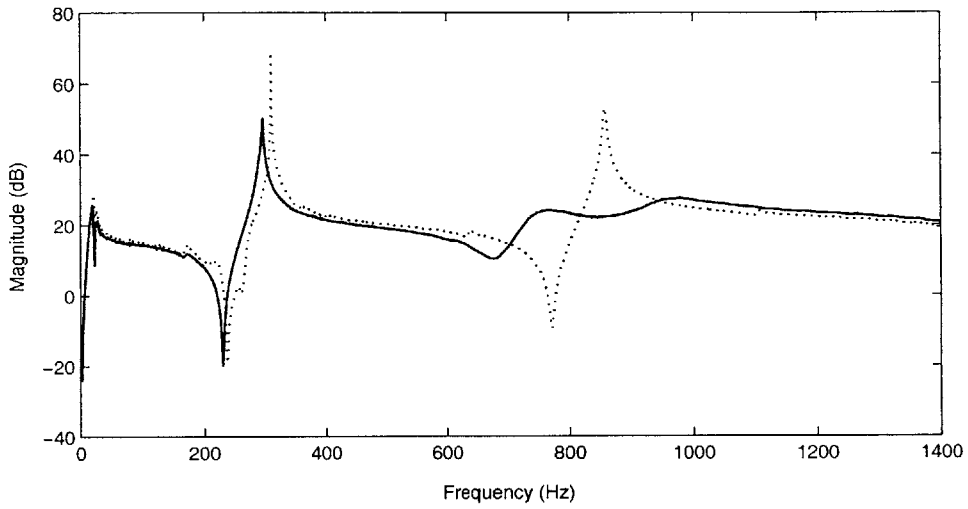

Figure 2.7: Measured force-to-acceleration frequency responses of the U-channel beam of length 591 mm under hammer excitation: unfilled (dotted), filled (solid). The accelerometer and excitation locations are at the same end of the beam. The excitation and measurement are in the transverse direction.

2.3 Model

In this section, we develop a model to predict the dynamics of the powder-filled beams described in Section 2.2. We consider a beam of length L, flexural stiffness EI, and mass m per unit length. A layer of granular material of thickness h and width b is coupled to the U-channel and box beams as shown in Figures 2.11 and 2.12. The beam is excited by a point-harmonic force in the y direction at a frequency ω and distance x_f from one end of the beam. We employ a simple Euler-Bernoulli model for the beam and consider the granular fill to be a compressible fluid in which two-dimensional pressure waves can propagate. While the mechanism of dissipation within the granular material is not completely understood, we characterize it by a complex speed of sound c_p defined by

$$c_p = c_0\sqrt{1 + j\eta \operatorname{sgn}\omega} \tag{2.1}$$

where η_p is the loss factor of the granular material and it is necessary to multiply the loss factor η_p by $\operatorname{sgn}\omega = \omega/|\omega|$ to avoid fallacious results in the inverse Fourier transform (Crandall [11]; Nashif *et al.* [31]).

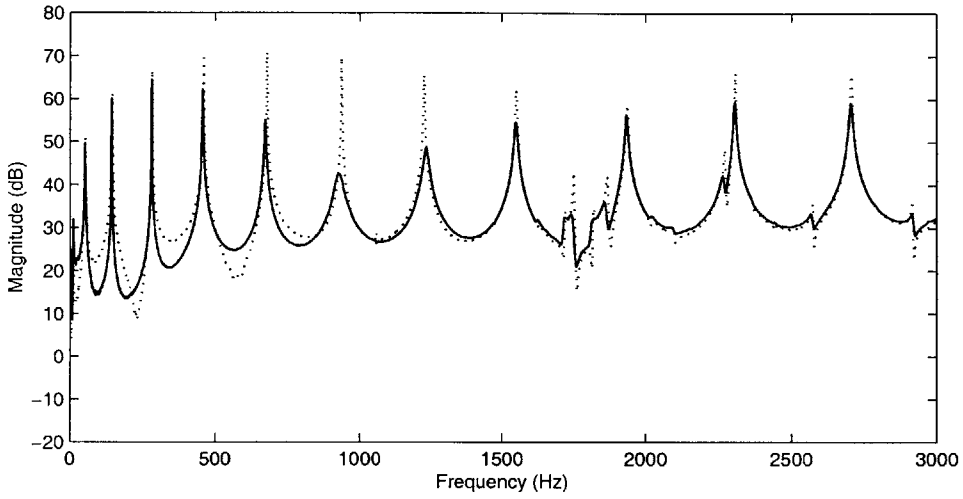

Figure 2.8: Measured force-to-acceleration frequency responses of the U-channel beam of length 2311 mm under hammer excitation: unfilled (dotted), filled with 0.55 inch thick powder (solid). The accelerometer and excitation locations are at different ends of the beam. The excitation and measurement are in the transverse direction.

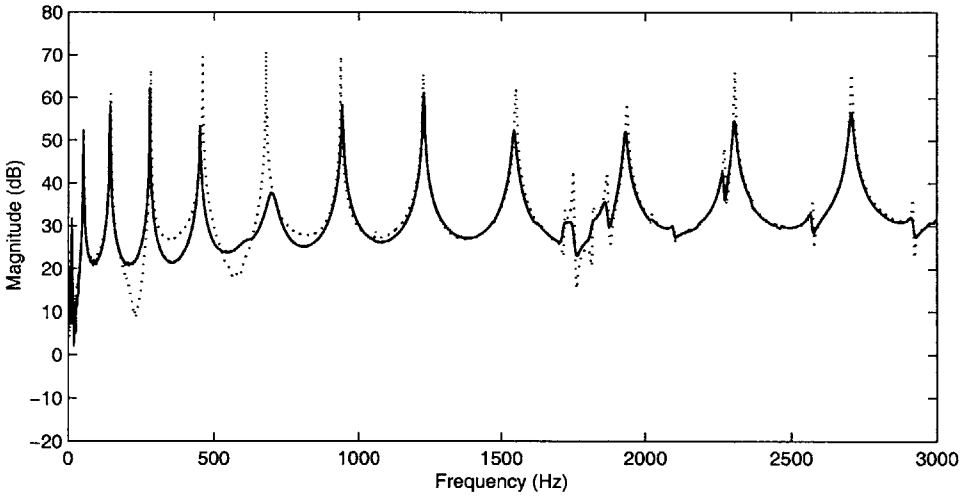

Figure 2.9: Measured force-to-acceleration frequency responses of the U-channel beam of length 2311 mm under hammer excitation: unfilled (dotted), filled with 0.90 inch thick powder (solid). The accelerometer and excitation locations are at different ends of the beam. The excitation and measurement are in the transverse direction.

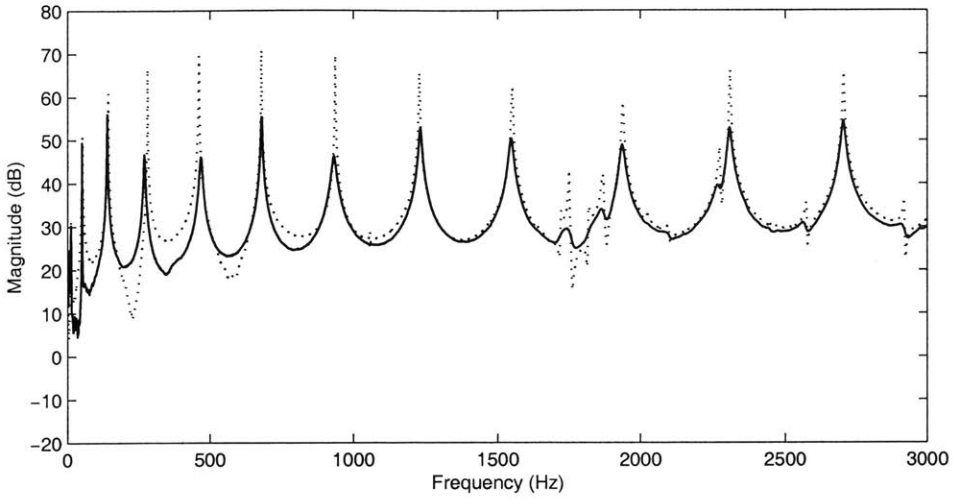

Figure 2.10: Measured force-to-acceleration frequency responses of the U-channel beam of length 2311 mm under hammer excitation: unfilled (dotted), filled with 1.55 inch thick powder (solid). The accelerometer and excitation locations are at different ends of the beam. The excitation and measurement are in the transverse direction.

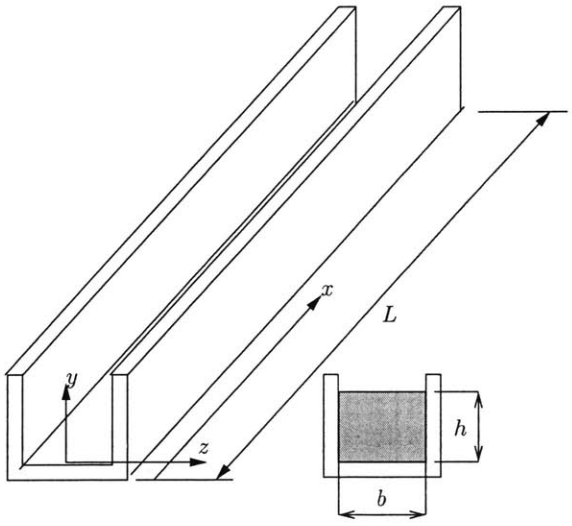

Figure 2.11: Diagram showing the parameters used in the model for a U-channel beam: The beam has length L and is partially filled with granular material over a width b and to a height h.

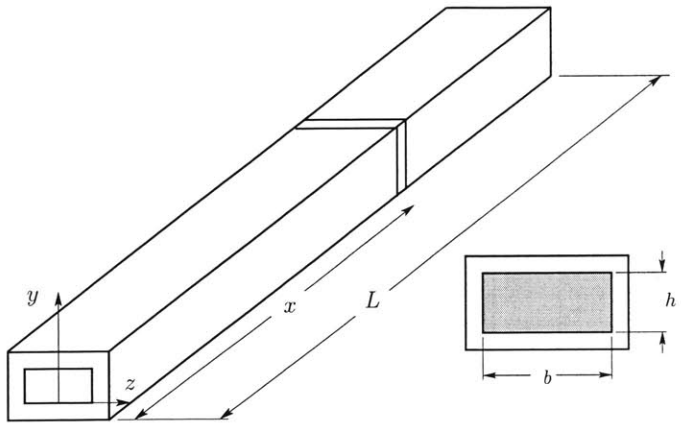

Figure 2.12: Diagram showing the parameters used in the model for a box beam: The beam has length L and is completely filled with granular material over a width b and height h.

2.3.1 Equations of Motion and Boundary Conditions

Consider steady vibration of the powder-filled beams of Figures 2.11 and 2.12 under harmonic excitation at a frequency ω by a point force $\mathrm{Re}(F\delta(x-x_f)e^{j\omega t})$. We denote the transverse vibratory displacement of the beam under such an excitation by $\mathrm{Re}(V(x,\omega)e^{j\omega t})$ and the pressure in the granular material by $\mathrm{Re}(p(x,y,\omega)e^{j\omega t})$. The pressure $p(x,y,\omega)$ in the granular material is assumed to be governed by the following familiar two-dimensional wave equation of a compressible fluid (e.g., Lighthill [28]; Kinsler *et.al.* [26])

$$\frac{\partial^2 p}{\partial x^2}+\frac{\partial^2 p}{\partial y^2}+\frac{\omega^2}{c_p^2}p=0 \tag{2.2}$$

U-Channel Beam

At the free surface of the powder (at $y=h$), the pressure must vanish. At the interface with the beam (at $y=0$), the pressure gradient $\partial p/\partial y$ is proportional to the acceleration of the beam. Hence we have the boundary conditions

$$p(x,h,\omega)=0 \qquad \text{and} \qquad \frac{\partial p}{\partial y}(x,0,\omega)=\rho\omega^2 V(x,\omega) \tag{2.3}$$

where ρ is the density of the powder. At the interface of the beam and powder (at $y=0$), the pressure $p(x,0,\omega)$ acting over the width b gives rise to a normal

force on the beam. Combining this interaction of the beam and powder, we write the Euler-Bernoulli equation governing the vibratory motion of the U-channel beam in the form

$$EI\frac{d^4V}{dx^4} - m\omega^2 V + bp(x,0,\omega) = F\delta(x - x_f) \tag{2.4}$$

Box Beam

For the box beam of Figure 2.12, we assume the powder to be in contact with the top (at $y = h$) and bottom (at $y = 0$) surfaces of the beam so that the respective pressure gradients are proportional to the acceleration of the beam. Therefore, we obtain the following boundary conditions on the powder

$$\frac{\partial p}{\partial y}(x,0,\omega) = \rho\omega^2 V(x,\omega) \qquad \text{and} \qquad \frac{\partial p}{\partial y}(x,h,\omega) = \rho\omega^2 V(x,\omega) \tag{2.5}$$

As in the case of the U-channel beam, we make use of the interaction between the powder and beam to write the following Euler-Bernoulli equation of motion for the powder-filled box beam

$$EI\frac{d^4V}{dx^4} - m\omega^2 V + b\left[p(x,0,\omega) - p(x,h,\omega)\right] = F\delta(x - x_f) \tag{2.6}$$

2.3.2 Solution Approach

Because closed-form solutions for the wave equation (2.2) subject to (2.3)–(2.4) or (2.5)–(2.6) are generally difficult to obtain, we seek approximate solutions to the coupled beam-powder problem. To this end, we expand the deflection of the beam in terms of the eigenfunctions of an undamped beam as

$$V(x,\omega) = V_{01}(\omega) + V_{02}(\omega)f(x) + \sum_{n=1}^{\infty} V_n(\omega)(\alpha_n(x) + \beta_n(x)) \tag{2.7}$$

The first two terms in the above expansion represent pure translational and rotational modes of the beam and $f(x)$ is a function linear in x. The remaining terms in the expansion represent the flexible modes of the beam where $\alpha_n(x)$ and $\beta_n(x)$ are, respectively, the propagating and evanescent components of the

nth flexible mode of the beam. As an example $f(x)$, $\alpha_n(x)$, and $\beta_n(x)$ take the following form for a free-free beam:

$$f(x) = x - L/2 \tag{2.8}$$
$$\alpha_n(x) = \sin(k_n x) + p_n \cos(k_n x) \tag{2.9}$$
$$\beta_n(x) = \sinh(k_n x) + p_n \cosh(k_n x) \tag{2.10}$$

where k_n is the wave number of the nth mode of the beam and p_n is a constant given by

$$p_n = \frac{\sin(k_n L) - \sinh(k_n L)}{\cosh(k_n L) - \cos(k_n L)} \tag{2.11}$$

The values of $k_n L$ for a free-free beam are provided in Table 2.1.

In the following sections, we compute the contributions from the flexible and rigid-body modes to the accelerance of the beam-powder systems. In order to do so we postulate a compatible pressure distribution in the powder based on the boundary conditions (2.3) or (2.5) and then solve for the wave propagation in powder and accelerance of the combined beam-powder system. The computed accelerance shows the validity of the assumed pressure distribution.

Contribution of Beam Flexible Modes

The form of the boundary conditions (2.3) and (2.5) suggest that the dependence of the pressure on x be of the same form as that of the deflection of the beam V. Hence we seek solutions for the pressure p in the form:

$$p(x, y, \omega) = \sum_{n=1}^{\infty} \phi_n(y, \omega)\alpha_n(x) + \sum_{n=1}^{\infty} \psi_n(y, \omega)\beta_n(x) \tag{2.12}$$

Substituting the above expression for p into the wave equation (2.2), we obtain the following differential equations for ϕ_n and ψ_n:

$$\phi_n'' - \lambda_{n1}^2 \phi_n = 0 \tag{2.13}$$
$$\psi_n'' - \lambda_{n2}^2 \psi_n = 0 \tag{2.14}$$

where $\lambda_{n1}^2 = -k_p^2 + k_n^2$ and $\lambda_{n2}^2 = -k_p^2 - k_n^2$ are the effective wave numbers through the thickness of the powder and $k_p = \omega/c_p$ is the complex wave number in the powder. The boundary conditions in (2.3) take the following form:

$$\phi_n'(0) = \rho\omega^2 V_n \quad ; \quad \phi_n(h, \omega) = 0 \tag{2.15}$$
$$\psi_n'(0) = \rho\omega^2 V_n \quad ; \quad \psi_n(h, \omega) = 0 \tag{2.16}$$

Table 2.1: Numerical values of the wave numbers for a free-free beam for various modes

mode number n	$k_n L$
1	4.73004074486270
2	7.85320462409584
3	10.99560783800167
4	14.13716549125746
5	17.27875965739948
6	20.42035224562606
7	23.56194490204046
8	26.70353755550819
9	29.84513020910325
10	32.98672286269282
11	36.12831551628263
12	39.26990816987242
13	42.41150082346221
14	45.55309347705200
15	48.69468613064180
16	51.83627878423159
17	54.97787143782139
18	58.11946409141117
19	61.26105674500097
20	64.40264939859077

We then solve (2.13) and (2.14) subject to the boundary conditions (2.15) and (2.16) to obtain the following expressions for ϕ_n and ψ_n for the U-channel beam

$$\phi_n(y,\omega) = \frac{\rho\omega^2 V_n}{\lambda_{n1}}\left(\frac{e^{\lambda_{n1}y} - e^{\lambda_{n1}(2h-y)}}{1+e^{2\lambda_{n1}h}}\right) \tag{2.17}$$

$$\psi_n(y,\omega) = \frac{\rho\omega^2 V_n}{\lambda_{n2}}\left(\frac{e^{\lambda_{n2}y} - e^{\lambda_{n2}(2h-y)}}{1+e^{2\lambda_{n2}h}}\right) \tag{2.18}$$

Likewise ϕ_n and ψ_n take the following form for the box beam:

$$\phi_n(y,\omega) = \frac{\rho\omega^2 V_n}{\lambda_{n1}}\left(\frac{e^{\lambda_{n1}y} - e^{\lambda_{n1}(h-y)}}{1+e^{\lambda_{n1}h}}\right) \tag{2.19}$$

$$\psi_n(y,\omega) = \frac{\rho\omega^2 V_n}{\lambda_{n2}}\left(\frac{e^{\lambda_{n2}y} - e^{\lambda_{n2}(h-y)}}{1+e^{\lambda_{n2}h}}\right) \tag{2.20}$$

Next, we use the above expressions for ϕ_n and ψ_n to compute the pressure at the beam-powder interface for the U-channel and box beam, respectively, as

$$\begin{aligned} p(x,0,\omega) &= \sum_{n=1}^{\infty}\frac{\rho\omega^2 V_n}{\lambda_{n1}}\left(\frac{1-e^{2\lambda_{n1}h}}{1+e^{2\lambda_{n1}h}}\right)\alpha_n(x) \\ &\quad + \sum_{n=1}^{\infty}\frac{\rho\omega^2 V_n}{\lambda_{n2}}\left(\frac{1-e^{2\lambda_{n2}h}}{1+e^{2\lambda_{n2}h}}\right)\beta_n(x) \end{aligned} \tag{2.21}$$

$$p(x,0,\omega) = \sum_{n=1}^{\infty}\frac{\rho\omega^2 V_n}{\lambda_{n1}}\left(\frac{1-e^{\lambda_{n1}h}}{1+e^{\lambda_{n1}h}}\right)\alpha_n(x) \tag{2.22}$$

$$+ \sum_{n=1}^{\infty}\frac{\rho\omega^2 V_n}{\lambda_{n2}}\left(\frac{1-e^{\lambda_{n2}h}}{1+e^{\lambda_{n2}h}}\right)\beta_n(x) \tag{2.23}$$

We then substitute the above expressions into (2.4) and (2.6) to solve for the respective V_n. In order to do so, we multiply the corresponding beam-deflection equations (2.4) and (2.6) by $\alpha_n(x)+\beta_n(x)$ and integrate the resulting expressions between 0 and L to obtain a system of linear equations in V_n. The nth equation in this system of equations has the following form:

$$\begin{aligned} &b\int_0^L \left[p(x,0,\omega) - p(x,h,\omega)\right]\left(\alpha_n(x)+\beta_n(x)\right)dx \\ &+(EIk_n^4 - m\omega^2)V_n\int_0^L(\alpha_n+\beta_n)^2\,dx = F(\alpha_n(x_f)+\beta_n(x_f)) \end{aligned} \tag{2.24}$$

The order of these linear systems is equal to the number of terms in the expansion (2.7) and their solution yields the respective V_n. In the next section, we obtain similar expressions for V_{01} and V_{02} corresponding to the rigid-body modes of the beam-powder system.

Contribution of Rigid-Body Beam Modes

When the beam undergoes pure translational motion, plane waves are excited in the y direction in the powder and the wave equation (2.2) reduces to the following simple form

$$p'' + k_p^2 p = 0 \tag{2.25}$$

Solving the above equation subject to the boundary conditions (2.3) and (2.5), we obtain the pressure distribution in the powder. Next, we substitute the pressure at the beam-powder interface into the beam-deflection equations (2.4) and (2.6) to obtain the following expressions for the response V_{01} of the U-channel beam:

$$V_{01} = -\frac{F}{-\rho c_p \omega b L \tan(k_p h) + m\omega^2} \tag{2.26}$$

and for the box beam:

$$V_{01} = -\frac{F}{2\rho\omega c_p b L \tan(k_p h/2) + m\omega^2} \tag{2.27}$$

When the beam undergoes a pure rotational motion as described by the second term in (2.7), the boundary conditions on the powder require the pressure p at the powder-beam interface to be linear in x. Based on the motion of the beam we can safely approximate the pressure distribution elsewhere to be linear in x. Therefore, we write the following compatible pressure distribution in the powder:

$$p(x, y, \omega) = f(x)\phi_0(y) \tag{2.28}$$

On substituting the above expression for p into the wave equation (2.2) and imposing the boundary conditions, we obtain the pressure distribution in the powder. Next, we use the beam-deflection equations (2.4) and (2.6) to obtain the following expressions for the response V_{02} of the U-channel beam:

$$V_{02} = \frac{6F}{m\omega^2 L + \rho c_p \omega b L^2 \tan(k_p h)} \tag{2.29}$$

and for the box beam:

$$V_{02} = -\frac{6F}{m\omega^2 L + 2\rho\omega c_p b L^2 \tan(k_p h/2)} \tag{2.30}$$

The Total Response

Next, after computing the contributions to the deflection V of the beam from the flexible and rigid-body modes, we write the non-dimensional accelerance R at the location of the sensor x_s as

$$R = \frac{m\omega^2 VL}{F} = \left(\frac{m\omega^2 L}{F}\right)\left(V_{01} + V_{02} f(x_s) + \sum_{n=1}^{\infty} V_n \left[\alpha_n(x_s) + \beta_n(x_s)\right]\right) \tag{2.31}$$

Finally, we plot in Figures 2.13–2.18 the force-to-acceleration frequency responses for the U-channel and box beams of various configurations and compare them with the measured results. From these figures we find that the resonant frequencies of the higher modes occur at lower frequencies than that predicted by the Euler-Bernoulli beam model. This discrepancy arises from shear deformation, which becomes important even in low-order modes for such thin-walled beams but is not taken into account in the beam model. Despite the simplicity of the beam model, we find that the predicted damping is roughly in accordance with the measurement, lending some confidence to our approach to the modeling of the behavior of the powder.

2.4 Chapter Summary

This chapter describes the damping of flexural vibrations using low-density granular media in which the speed of sound is low. We conduct several experiments and find that high damping can be obtained over a broad range of frequencies and that the phenomenon behaves linearly over a wide range of amplitudes. We propose that the powder can be modeled as a fluid in which pressure waves can propagate and find that such a model matches the experiments well.

Next, we ask: Can this damping mechanism work with other low-wave-speed media? In the next chapter we apply this approach to low-density foams in which the speeds of wave propagation are small and find a similar

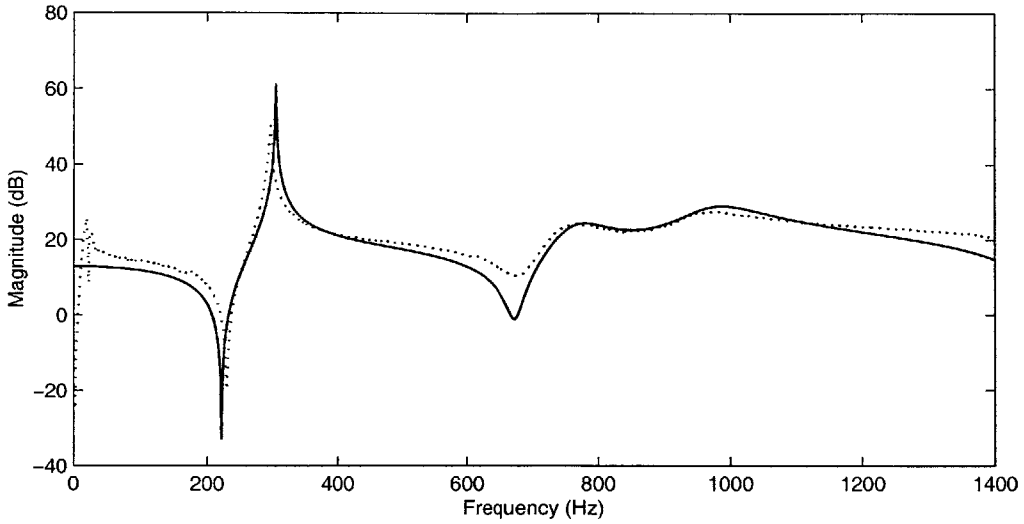

Figure 2.13: Comparison of measured and predicted force-to-acceleration frequency responses of the U-channel beam of length 591 mm: measured (dotted), predicted (solid)

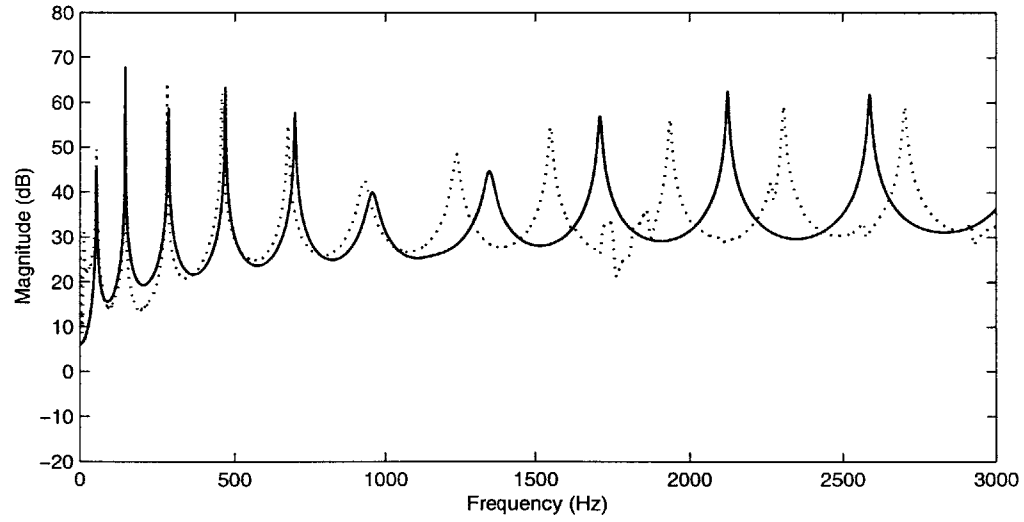

Figure 2.14: Comparison of measured and predicted force-to-acceleration frequency responses of the U-channel beam of length 2311 mm with a 0.52 inch thick granular fill: measured (dotted), predicted (solid)

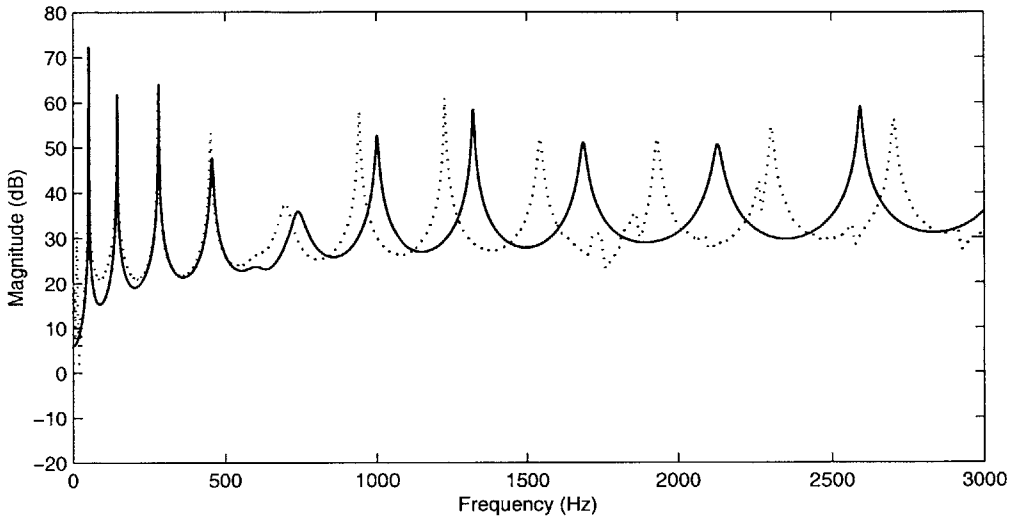

Figure 2.15: Comparison of measured and predicted force-to-acceleration frequency responses of the U-channel beam of length 2311 mm with a 0.90 inch thick granular fill: measured (dotted), predicted (solid)

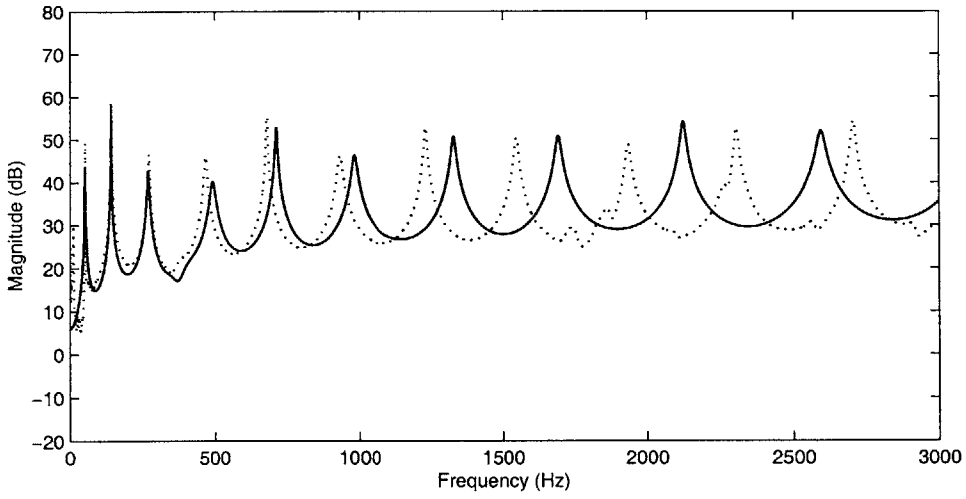

Figure 2.16: Comparison of measured and predicted force-to-acceleration frequency responses of the U-channel beam of length 2311 mm with a 1.55 inch thick granular fill: measured (dotted), predicted (solid)

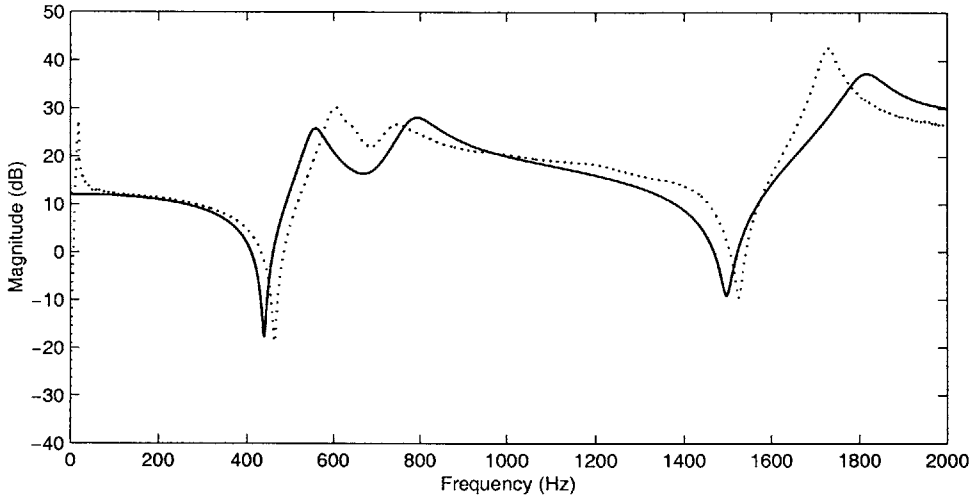

Figure 2.17: Comparison of measured and predicted force-to-acceleration frequency responses of the box beam of length 718 mm: measured (dotted), predicted (solid)

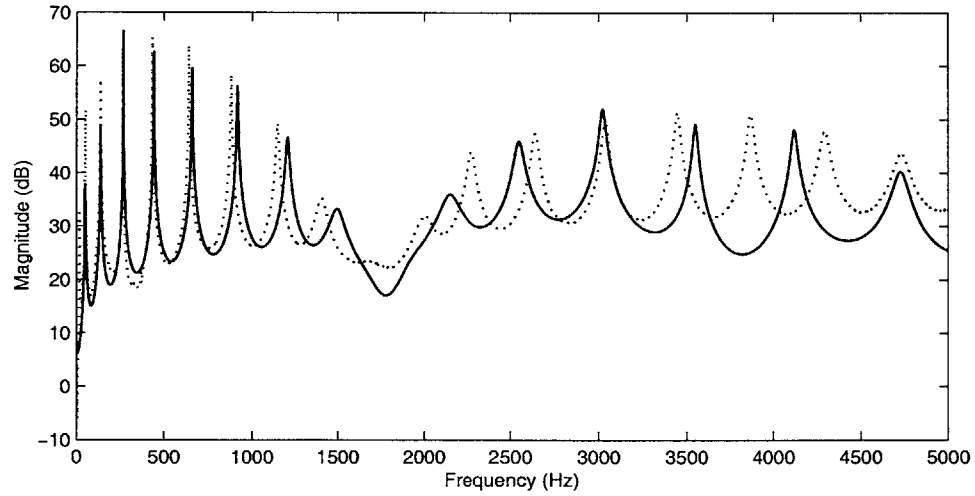

Figure 2.18: Comparison of measured and predicted force-to-acceleration frequency responses of the box beam of length 1829 mm: measured (dotted), predicted (solid)

damping behavior. This confirms that these damping treatments can work with a variety of media.

CHAPTER 3

Damping Flexural Waves By Coupling to Lossy Low-Wave-Speed Foams

3.1 Introduction

The studies in the previous chapter on powder-beam systems show that large damping can be attained whenever there is a strong coupling between the vibration of the beam and wave propagation in powder. In this chapter, we extend this approach to other low-wave-speed media such as foams. Foam materials are commonly employed for sound absorption and noise control (e.g., Kinsler *et. al.* [26]; Beranek and Ver [6]) in aircraft and automobiles. They are also widely used as absorptive liners in anechoic chambers, air conditioning systems, intake and exhaust ducts of turbines, and large industrial fans among other applications. In this chapter, we study on the flexural dynamics of beams coupled to foams in which the speed of sound propagation is much lower than that in the beam. Section 3.2 describes experiments where such coupling provides significant damping (as high as 7%) over a broad band of frequencies for a relatively low (3.9%) increase in mass. Next, experiments on sandwich beams formed by coupling the above described beam-foam system to a thin beam or membrane are presented.

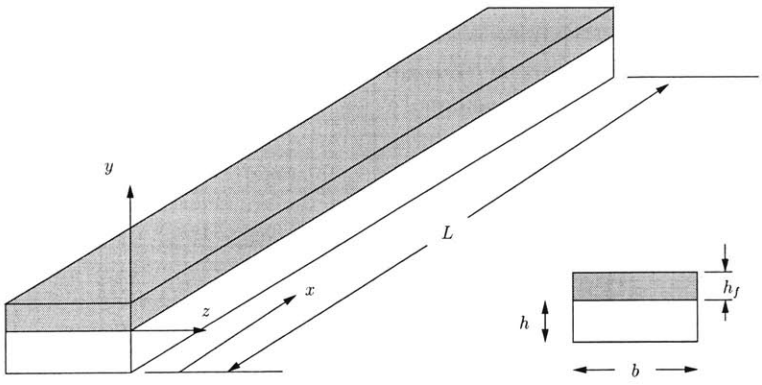

Figure 3.1: Schematic of the beam-foam system

The focus of Section 3.3 is to develop a simple, linear model of an Euler-Bernoulli beam that is coupled to a foam material in which dilatation and shear waves can propagate. Next, modal expansion techniques are used to obtain the accelerance of such a beam under various boundary conditions. The results of the model are found to be in close agreement with the responses measured in the experiments.

3.2 Experiments

We study beam-foam systems of the configuration shown in Figure 3.1. A photograph of the aluminum beam with and without foam is shown in Figure 3.2. An aluminum beam of rectangular cross section 38.1×12.7 mm is coupled to a 12.7 mm thick layer of EAR C-3201 (EAR Corporation [14]) energy-absorbing foam using 3M Contact 80 neoprene adhesive (3M Corporation [1]). The density of the foam is 104.1 kg/m^3, and the Appendix details a set of measurements performed to determine the complex extensional and shear moduli of the foam. In all of the experiments, the beams are suspended by soft elastic strings to simulate free-free boundary conditions. An impulsive excitation is provided by an impact hammer (PCB333A30 [40]) at one end of the beam in the transverse direction, and the response is measured by an accelerometer (PCB353B11 [40]) located at the other end of the beam.

In Figure 3.3, we plot the force-to-acceleration frequency response obtained for a beam of length 1448 mm with and without the foam layer. As expected,

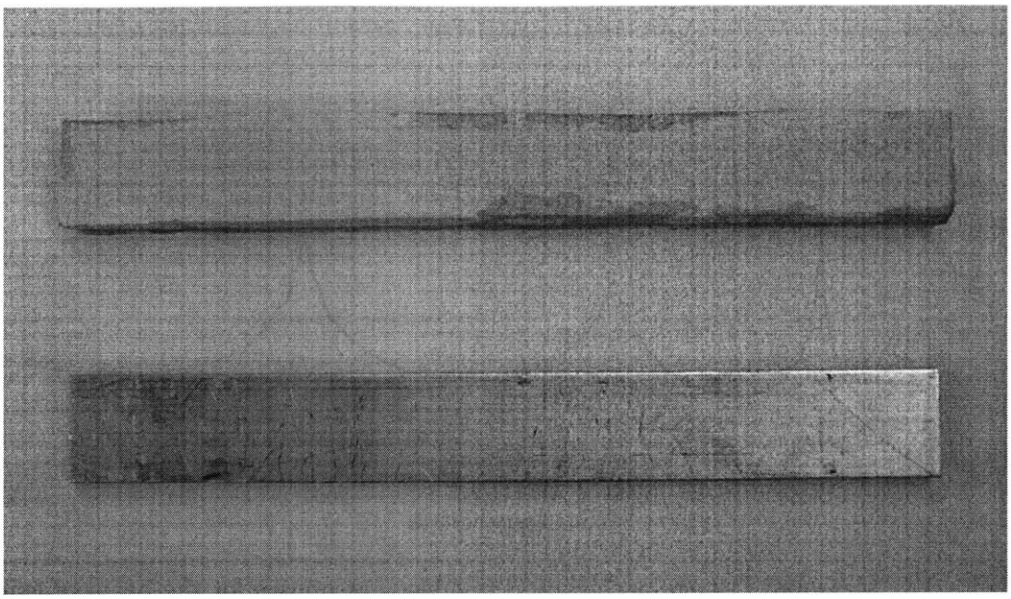

Figure 3.2: Photograph of an aluminum beam coupled to foam

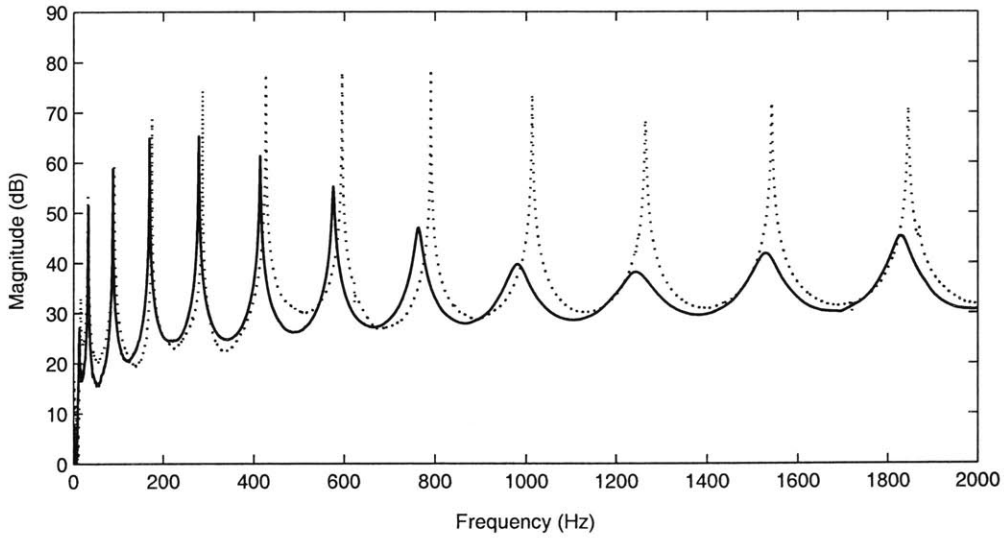

Figure 3.3: Measured force-to-acceleration frequency responses for a beam of length 1448 mm under impact excitation: without foam (dotted) and with foam (solid). The excitation and measurement are in the transverse direction.

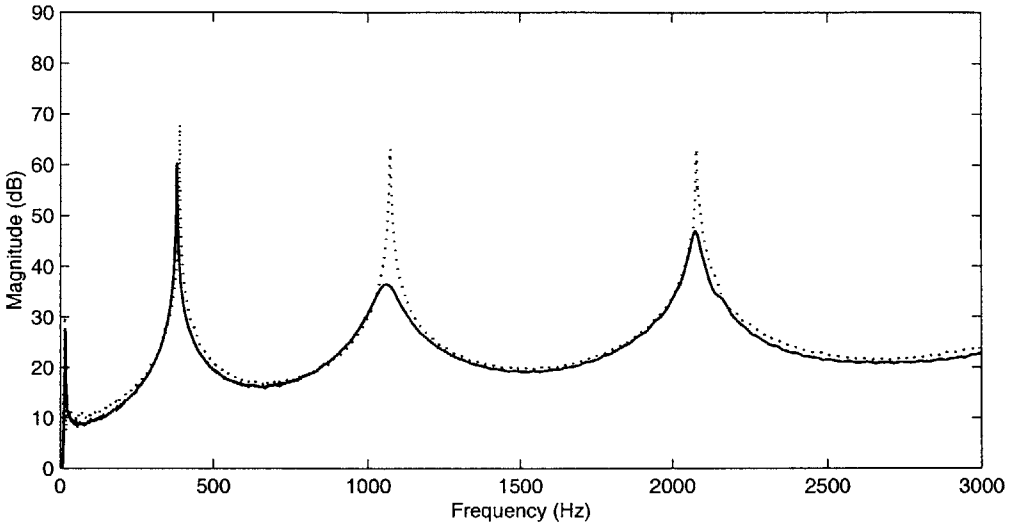

Figure 3.4: Measured force-to-acceleration frequency responses for the beam of length 585 mm under impact excitation: without foam (dotted) and with foam (solid). The excitation and measurement are in the transverse direction.

the beams without foam exhibit very little damping, with $\zeta < 0.0001$ for each of the modes. When a layer of foam of thickness 12.7 mm is glued to the beam, the increase in damping in the first four modes is very small, but there is a significant increase of damping in the fifth and higher modes. Based on the speeds of sound in the foam, we find that the sixth mode occurs in a frequency range where quarter-wavelength dilatation and half-wavelength shear waves can be set up through the thickness of the foam.

In Figure 3.4, we plot the force-to-acceleration frequency response for a beam of length 585 mm. In this case, there is moderate damping in the first mode but a significant increase in damping in the second and third modes. This suggests that the high damping observed in the frequency band of 400 Hz to 2 kHz is the result of strong coupling between the beam and foam arising from the establishment of standing waves through the thickness of the foam.

Next, in Figures 3.5, 3.6, and 3.7, we plot the force-to-acceleration frequency-response curves measured for sandwich beams formed by the addition of thin "auxiliary" metal layers atop the layer of foam. With the addition of the steel layers with thicknesses of 0.05 and 0.10 mm, the damping is further increased in the fifth to eighth and fifth to seventh modes, respectively, when compared

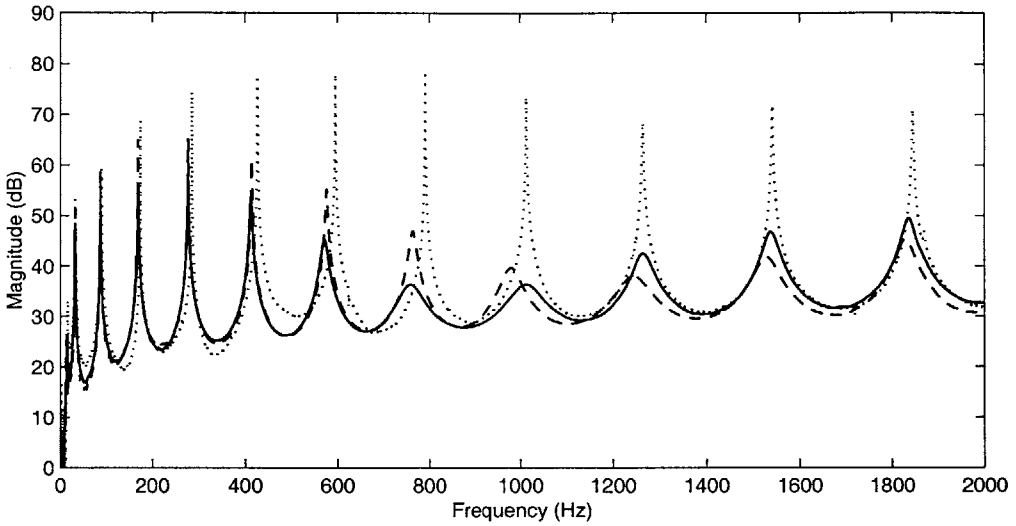

Figure 3.5: Measured force-to-acceleration frequency responses under impact excitation: without foam (dotted), with foam (dashed), and with an auxiliary 0.05 mm thick steel layer (solid). The excitation and measurement are in the transverse direction.

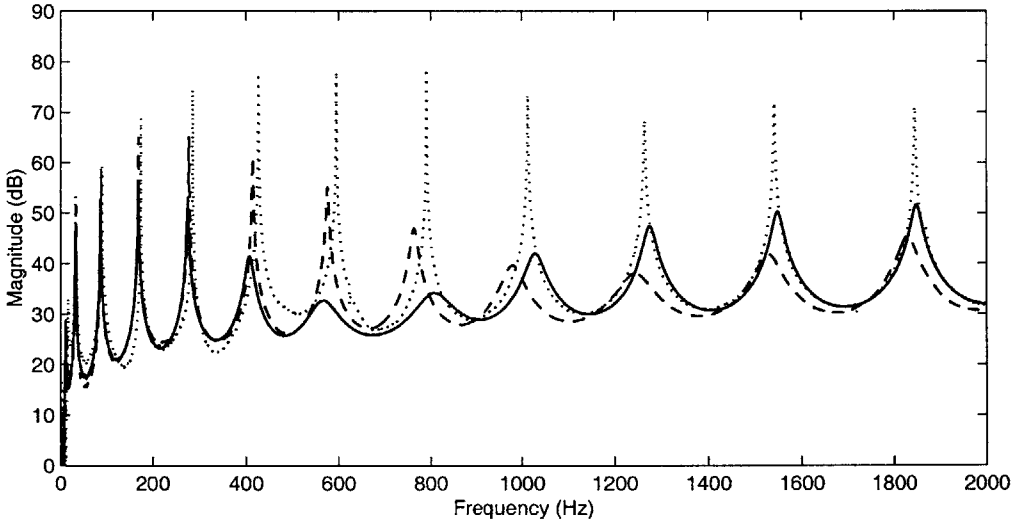

Figure 3.6: Measured force-to-acceleration frequency responses under impact excitation: without foam (dotted), with foam (dashed), and with an auxiliary 0.10 mm thick steel layer (solid). The excitation and measurement are in the transverse direction.

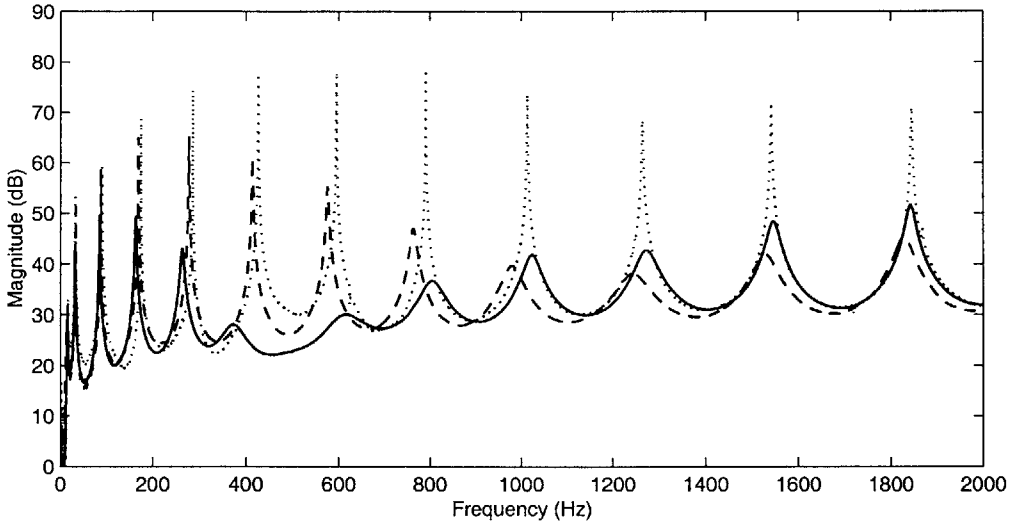

Figure 3.7: Measured force-to-acceleration frequency responses under impact excitation: without foam (dotted), with foam (dashed), and sandwich beam with a 0.81 mm thick aluminum auxiliary layer (solid). The excitation and measurement are in the transverse direction.

to the corresponding beam-foam system without auxiliary layers. The addition of these steel layers results in a significant increase in damping at lower frequencies with a relatively small increase in mass (1.2% and 2.4% for the 0.05 mm and 0.10 mm thick steel layers, respectively). In the case of an aluminum auxiliary layer with a thickness of 0.81 mm (6.4% of the mass of the beam), the damping is further increased in the third to seventh modes when compared to the corresponding beam-foam system without the auxiliary layer.

3.3 Model

In this section, we develop a model by which the responses measured in Section 3.2 can be predicted. We consider a beam of length L, flexural stiffness EI, and mass per unit length m. A layer of foam is coupled to the beam as shown in Figure 3.1. The beam is excited by a point-harmonic force at a frequency ω and distance x_f from one end of the beam in the y direction. We employ a simple Euler-Bernoulli model for the beam and consider the foam to be a lossy and isotropic continuum in which waves of dilatation and distortion can propagate.

The foam material used in the experiments described in Section 3.2 is an elastic-porous medium. It is known that three types of waves can propagate in such media: two types of dilatation waves and a shear wave (e.g., Biot [7]; Bolton *et.al.* [8]). The dilatation waves that depend largely on the bulk elastic properties of the material are referred to as frame-borne waves, whereas those which depend on the acoustical properties of the fluid in the pores, the porosity, and the flow resistivity are known as air-borne waves. The stress induced on the beam by the air-borne waves scales as the product of the bulk modulus of the air in the pores times the volumetric strain in air. Hence although these waves can have a significant influence on sound and noise transmission, we can safely neglect their effect on the vibration of the beam. Therefore, we treat the foam as an isotropic continuum in which waves of dilatation and distortion arising from the bulk properties of the foam can propagate. The foam is characterized by a complex Young's modulus of elasticity $E_f = \hat{E}_f(1 + j\eta \text{ sgn } \omega)$, loss factor η, and Poisson ratio ν (e.g., Timoshenko and Goodier [49]).

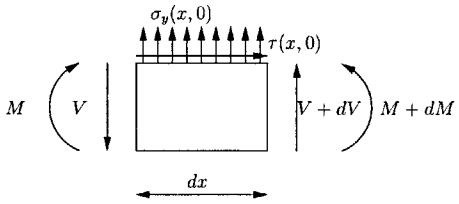

Figure 3.8: Free-body diagram of an infinitesimal beam element of length dx

3.3.1 Equations of Motion

Consider steady vibration of the beam-foam system of Figure 3.1 under harmonic excitation at a frequency ω by a point force $\mathrm{Re}(F\delta(x-x_f)e^{j\omega t})$ in the y direction. We denote the transverse vibratory displacement of the beam under such an excitation by $\mathrm{Re}(V(x,\omega)e^{j\omega t})$ and the displacements of the foam in the x and y directions by $\mathrm{Re}(u(x,y,\omega)e^{j\omega t})$ and $\mathrm{Re}(v(x,y,\omega)e^{j\omega t})$, respectively. The displacements $u(x,y,\omega)$ and $v(x,y,\omega)$ in the foam are governed by the following second-order wave equations of a linear and isotropic continuum (e.g., Timoshenko and Goodier [49]):

$$(\lambda+2G)u_{xx}+Gu_{yy}+(\lambda+G)v_{xy}+\rho\omega^2 u = 0 \qquad (3.1)$$

$$Gv_{xx}+(\lambda+2G)v_{yy}+(\lambda+G)u_{xy}+\rho\omega^2 v = 0 \qquad (3.2)$$

where the subscripts denote partial differentiation and ρ, $\lambda=\nu E_f/(1+\nu)(1-2\nu)$, and G are respectively, the density, complex Lame constant, and complex shear modulus of the material of the foam. To obtain the equation governing flexural vibration of the beam, we consider an infinitesimal element of the beam of length dx as shown in Figure 3.8. At the interface of the beam and foam (that is, at $y=0$), the normal stress $\sigma_y(x,0,\omega)$ contributes to a force in y direction whereas the shear stress $\tau_{xy}(x,0,\omega)$ results in a moment about the neutral axis. Making use of the above interaction between the foam and beam, we write the Euler-Bernoulli equation governing the transverse deflection V of the beam in the form

$$EI\frac{d^4V}{dx^4}-m\omega^2V-b\sigma_y(x,0,\omega)-\frac{bh}{2}\frac{\partial\tau_{xy}(x,0,\omega)}{\partial x}=F\delta(x-x_f) \qquad (3.3)$$

where b and h are, respectively, the width and height of the beam's cross section.

3.3.2 Boundary Conditions for the Foam

At the interface between the foam and beam (at $y = 0$), the displacements in the foam must match those of the surface of the beam. Hence we obtain

$$v(x, 0, \omega) = V(x, \omega) \tag{3.4}$$

$$u(x, 0, \omega) = -\frac{h}{2}\frac{\partial V}{\partial x} \tag{3.5}$$

At the free surface of the foam (at $y = h_f$), the normal and shear stresses must vanish. Hence we have

$$\lambda u_x(x, h_f, \omega) + (\lambda + 2G) v_y(x, h_f, \omega) = 0 \tag{3.6}$$

$$u_y(x, h_f, \omega) + v_x(x, h_f, \omega) = 0 \tag{3.7}$$

Likewise, at the free surfaces in the x direction (at $x = 0$ and $x = L$) the normal and shear stresses must vanish. Because the foam layers used in the experiments are long and slender, and strong damping is observed at frequencies at or above the frequencies at which the lengths of waves in the foam are on the order of the thickness of the foam, we do not impose boundary conditions on the ends of the foam (at $x = 0$ and L). This simplification allows us to reasonably approximate the behavior of the foam over most of the length of the beam and to obtain relatively simple predictions of the effect of the foam on the vibration of the beam.

3.3.3 Approximate Solution

Because closed-form solutions for (3.1)–(3.3) along with the boundary conditions (3.4)–(3.7) are generally difficult to obtain, we seek approximate solutions to the coupled beam-foam problem. To this end, we expand the deflection of the beam in terms of the eigenfunctions of an undamped beam as

$$V(x, \omega) = V_{01}(\omega) + V_{02}(\omega) f(x) + \sum_{n=1}^{\infty} V_n(\omega)(\alpha_n(x) + \beta_n(x)) \tag{3.8}$$

The first two terms in the above expansion represent pure translation and rotation of the beam and $f(x)$ is a function linear in x. The remaining terms in the expansion represent the flexible modes of the beam where $\alpha_n(x)$ and $\beta_n(x)$ are, respectively, the propagating and evanescent components of the nth

flexible mode of the beam. As an example, we find that $f(x)$, $\alpha_n(x)$, and $\beta_n(x)$ take the following form for a free-free beam:

$$f(x) = x - L/2 \tag{3.9}$$

$$\alpha_n(x) = \sin(k_n x) + p_n \cos(k_n x) \tag{3.10}$$

$$\beta_n(x) = \sinh(k_n x) + p_n \cosh(k_n x) \tag{3.11}$$

where k_n is the wave number of the nth mode of the beam (values provided in Table 2.1) and p_n is a constant given by

$$p_n = \frac{\sin(k_n L) - \sinh(k_n L)}{\cosh(k_n L) - \cos(k_n L)} \tag{3.12}$$

In the following sections, we compute the contributions from the flexible and rigid-body modes to the accelerance of the beam-foam systems. As in the case of powder-beam systems discussed in Chapter 2, we postulate compatible foam displacements based on the boundary conditions (3.4)–(3.7) and then solve for the wave propagation in foam and accelerance of the combined beam-foam system.

Contribution of Beam Flexible Modes

As in the case of the solution procedure for beam-powder systems of Chapter 2 (Section 2.3.2), the form of the boundary conditions (3.4)–(3.7) suggests that the dependence of the deformations in the foam on x be of the same form as that of the deflection of beam V. Hence we seek solutions for the foam displacements u and v in the following form

$$v(x, y, \omega) = \sum_{n=1}^{\infty} \chi_n(y, \omega)\alpha_n(x) + \sum_{n=1}^{\infty} \xi_n(y, \omega)\beta_n(x) \tag{3.13}$$

$$u(x, y, \omega) = \sum_{n=1}^{\infty} \phi_n(y, \omega)\alpha_n'(x)/k_n + \sum_{n=1}^{\infty} \psi_n(y, \omega)\beta_n'(x)/k_n \tag{3.14}$$

where the primes denote the first derivative, and χ, ξ, ϕ, and ψ are yet to be determined functions of y and ω. Substituting the above expansions for u and v into the wave equations (3.1) and (3.2), we obtain the system of first-order ordinary differential equations

$$X_n' = A_n X_n \tag{3.15}$$

Table 3.1: Form of the coefficient matrix A_n in (3.15)

$$\begin{bmatrix}
0 & 1 & 0 & 0 & 0 & 0 & 0 & 0 \\
-\frac{\rho\omega^2 - k_n^2(\lambda+2G)}{G} & 0 & 0 & 0 & 0 & -\frac{\lambda+G}{G}k_n & 0 & 0 \\
0 & 0 & 0 & 1 & 0 & 0 & 0 & 0 \\
0 & 0 & -\frac{\rho\omega^2 + k_n^2(\lambda+2G)}{G} & 0 & 0 & 0 & 0 & -\frac{\lambda+G}{G}k_n \\
0 & 0 & 0 & 0 & 0 & 1 & 0 & 0 \\
0 & \frac{\lambda+G}{\lambda+2G}k_n & 0 & 0 & -\frac{\rho\omega^2 - k_n^2 G}{\lambda+2G} & 0 & 0 & 0 \\
0 & 0 & 0 & 0 & 0 & 0 & 0 & 1 \\
0 & 0 & 0 & -\frac{\lambda+G}{\lambda+2G}k_n & 0 & 0 & -\frac{\rho\omega^2 + k_n^2 G}{\lambda+2G} & 0
\end{bmatrix}$$

where the vector X_n is of the form

$$X_n = \begin{pmatrix} \phi_n & \phi_n' & \psi_n & \psi_n' & \chi_n & \chi_n' & \xi_n & \xi_n' \end{pmatrix}^T \tag{3.16}$$

and the matrix A_n is given in Table 3.1. Next, we solve (3.15) subject to the boundary conditions (3.4)–(3.7) to obtain

$$X_n = B_n e^{\Lambda_n y} c_n V_n \tag{3.17}$$

where the B_n and Λ_n are, respectively, the matrices of eigenvectors and eigenvalues obtained by diagonalizing the A_n, and the c_n are constant vectors whose elements are determined by enforcing the boundary conditions (3.4)–(3.7). Thus, having obtained the functions χ_n, ξ_n, ϕ_n, and ψ_n, we compute the stresses $\sigma_y(x,0)$ and $\tau_{xy}(x,0)$ at the interface of the foam and the beam as

$$\begin{aligned}
\sigma_y(x,0) &= \sum_{n=1}^{\infty} \left(-k_n\lambda\phi_n(0) + (\lambda+2G)\chi_n'(0)\right)\alpha_n(x) \\
&\quad + \sum_{n=1}^{\infty} \left(\lambda k_n\psi_n(0) + (\lambda+2G)\xi_n'(0)\right)\beta_n(x) \qquad (3.18) \\
\tau_{xy}(x,0) &= \sum_{n=1}^{\infty} \frac{G}{k_n}\left(\phi_n'(0) + k_n\chi_n(0)\right)\alpha_n'(x) \\
&\quad + \sum_{n=1}^{\infty} \frac{G}{k_n}\left(\psi_n'(0) + k_n\xi_n(0)\right)\beta_n'(x) \qquad (3.19)
\end{aligned}$$

Next, we substitute the above expressions for the stresses into (3.3) to solve for the V_n. In order to do so, we multiply (3.3) by $\alpha_n(x)+\beta_n(x)$ and integrate the

resulting expression between 0 and L to obtain a system of linear equations in the V_n whose order is equal to the number of terms in expansion (3.8). The nth equation in these system of equations has the following form:

$$-\int_0^L \left[b\sigma_y(x,0,\omega) + \frac{bh}{2}\frac{\partial \tau_{xy}(x,0,\omega)}{\partial x}\right](\alpha_n(x) + \beta_n(x))\,dx$$
$$+(EIk_n^4 - m\omega^2)V_n \int_0^L (\alpha_n + \beta_n)^2\,dx = F(\alpha_n(x_f) + \beta_n(x_f)) \quad (3.20)$$

By solving the above set of equations we obtain the response V_n corresponding to the flexible modes of the beam. In the next section, we obtain similar expressions for V_{01} and V_{02} corresponding to the rigid-body modes of the beam-foam system.

Contribution of Rigid-Body Beam Modes

When the beam undergoes pure translational motion, the displacement u in the x direction is zero everywhere in the foam. As a result, plane waves are excited in the y direction and the wave equations (3.1)–(3.2) reduce to the following simple form:

$$(\lambda + 2G)v_{yy} + \rho\omega^2 v = 0 \quad (3.21)$$

This equation is solved subject to the boundary conditions (3.4)–(3.7) to obtain the displacement $v(y,\omega)$ in the foam. From the displacement v, we compute the normal stress exerted by the foam at the interface of the foam and obtain the corresponding response $V_{01}(\omega)$ of the beam (as in the case of the rigid-body modes of beam-powder systems of Section 2.3.2).

When the beam undergoes a rotational motion as described by the second term in (3.8), the boundary conditions on the foam require that the displacement u in the x direction in the foam be a constant at the foam-beam interface. We therefore expect the displacement u in the foam to be a function of only the y coordinate. Likewise, the displacement v in the y direction is linear in x at the interface of the foam and the beam. Therefore, we write the following compatible displacements in the foam:

$$v(x,y,\omega) = f(x)\chi_0(y,\omega) \quad (3.22)$$
$$u(x,y,\omega) = \phi_0(y,\omega) \quad (3.23)$$

Substituting these displacements into the wave equations (3.1)–(3.2), we obtain the following differential equations for χ_0 and ϕ_0:

$$(\lambda + 2G)\chi_0'' + \rho\omega^2\chi_0 = 0 \tag{3.24}$$

$$G\phi_0'' + (\lambda + 2G)\chi_0' + \rho\omega^2\phi_0 = 0 \tag{3.25}$$

Imposing the boundary conditions (3.4)–(3.7), we solve for the displacements in the foam and stresses exerted by the foam on the beam and then obtain the coefficient $V_{02}(\omega)$ in the expansion (3.8).

The Total Response

Next, after computing the contributions to the displacement of the beam from the flexible and rigid-body modes, we write the non-dimensional accelerance R at the location of the sensor x_s as

$$R = \frac{m\omega^2 VL}{F} = \left(\frac{m\omega^2 L}{F}\right)\left(V_{01} + V_{02}f(x_s) + \sum_{n=1}^{\infty} V_n\left[\alpha_n(x_s) + \beta_n(x_s)\right]\right) \tag{3.26}$$

Finally, we plot in Figures 3.9 and 3.10 the force-to-acceleration frequency responses for the long and short beams and compare them with the measured responses. We find that there is good agreement between the measured and predicted frequency responses. At each of the resonant frequencies of the beams, we extract the frequency and loss factor from the measurements using the modal curve-fitting software Star Modal [46]. We then compare these results with the theoretical predictions in Tables 3.2 and 3.3, respectively for the long and short beams. These comparisons show that the foam can be adequately modeled as a continuum in which waves can propagate.

3.3.4 Model for Sandwich Beam and Approximate Solutions

In this section, we develop a model for the sandwich beam formed by coupling an auxiliary layer to the foam-beam system discussed in the previous section. The auxiliary layer at $y = h_f$ changes the boundary conditions on the foam given in (3.6) and (3.7). We now require at $y = h_f$ that the deformations $v(x, h_f, \omega)$ and $u(x, h_f, \omega)$ in the foam match those in the auxiliary layer.

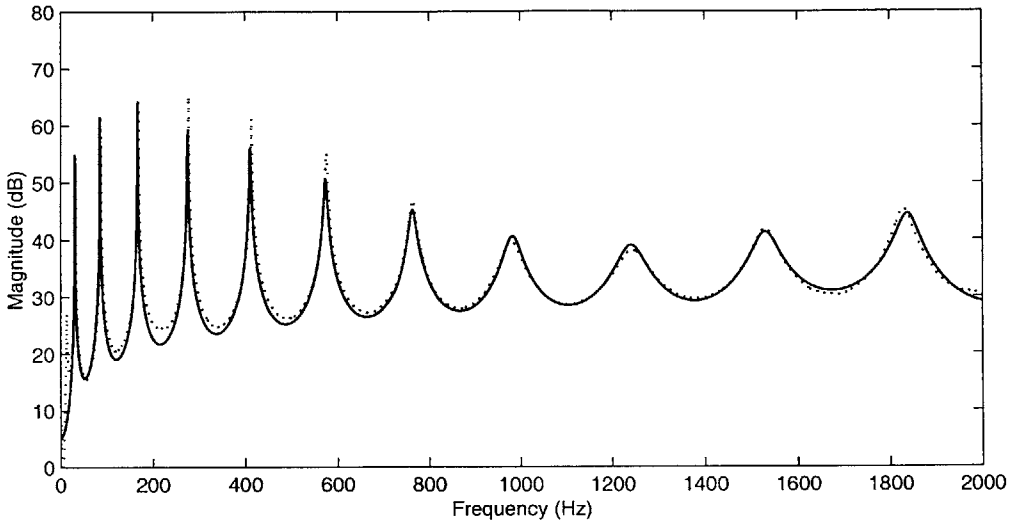

Figure 3.9: Comparison of measured and predicted force-to-acceleration frequency responses for long beam with foam layer: measured (dotted) and predicted (solid)

Table 3.2: Comparison of measured and predicted modal frequencies and damping ratios for the long aluminum beam

Modal Frequencies (Hz)		Damping Ratio	
Measured	Predicted	Measured	Predicted
32.35	31.90	0.0001	0.00004
87.67	87.14	0.0005	0.0001
168.97	168.0	0.0005	0.0005
277.87	277.13	0.0009	0.0010
413.86	413.19	0.0017	0.0024
575.71	574.65	0.0040	0.005
763.13	763.07	0.0090	0.0104
979.87	980.77	0.0212	0.0200
1240.0	1240.0	0.0261	0.0240
1530.0	1530.0	0.0161	0.0174
1830.0	1840.0	0.0103	0.0118

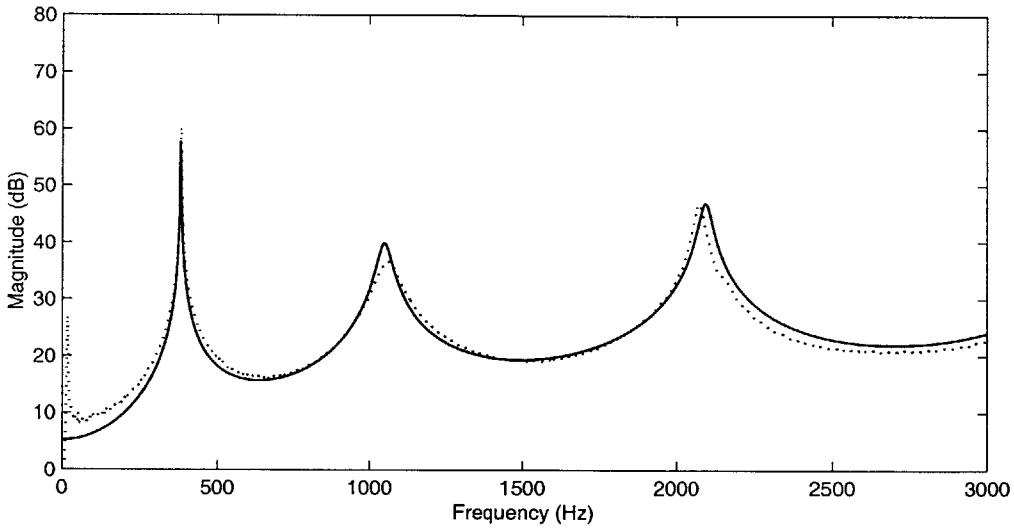

Figure 3.10: Comparison of measured and predicted force-to-acceleration frequency responses for short beam with foam: measured (dotted) and predicted (solid)

Table 3.3: Comparison of measured and predicted modal frequencies and damping ratios for the short aluminum beam

Modal Frequencies (Hz)		Damping Ratio	
Measured	Predicted	Measured	Predicted
380.63	379.25	0.002	0.0024
1060.0	1055.0	0.035	0.030
2070.0	2080.0	0.0075	0.008

Hence, we have

$$v(x, h_f, \omega) = W(x, \omega) \tag{3.27}$$

$$u(x, h_f, \omega) = \frac{h_a}{2} \frac{\partial W(x, \omega)}{\partial x} \tag{3.28}$$

where $\mathrm{Re}(W(x, \omega)e^{j\omega t})$ and h_a are respectively, the deflection and height of the auxiliary beam. By taking into account the normal stress $\sigma_y(x, h_f)$ and shear stress $\tau_{xy}(x, h_f)$ in the foam as in (3.3), we write the Euler-Bernoulli equation governing the deflection W of the auxiliary beam in the form

$$E_a I_a \frac{d^4 W}{dx^4} - m_a \omega^2 W + b\sigma_y(x, h_f, \omega) - \frac{bh_a}{2} \frac{\partial \tau_{xy}(x, h_f, \omega)}{\partial x} = 0 \tag{3.29}$$

where $E_a I_a$ and m_a are respectively, the flexural stiffness and the mass per unit length of the auxiliary beam.

Approximate Solution

To obtain the force-to-acceleration frequency response for the sandwich beam, we must simultaneously solve the wave equations (3.1)–(3.2) and the beam-deflection equations (3.3) and (3.29) subject to the boundary conditions (3.6), (3.7), (3.27), and (3.28). As in Section 3.3.3, we expand the deflection of the principal beam according to (3.8) and find compatible displacements in foam as in Sections 3.3.3 and 3.3.3, and expand the deflection W of the auxiliary beam as

$$W(x, \omega) = W_{01}(\omega) + W_{02}(\omega) f(x) + \sum_{n=1}^{\infty} W_n(\omega)(\alpha_n(x) + \beta_n(x)) \tag{3.30}$$

To obtain the contribution to the accelerance from the flexible modes, we solve (3.15) subject to the boundary conditions (3.6), (3.7), (3.27), and (3.28) to obtain

$$X_n = B_n e^{\Lambda_n y}(c_n V_n + d_n W_n) \tag{3.31}$$

where B_n and Λ_n are, respectively, the matrices of eigenvectors and eigenvalues obtained by diagonalizing A_n, and c_n and d_n are constant vectors whose elements can be determined by enforcing the boundary conditions (3.6), (3.7), (3.27), and (3.28). We then use the above solution to compute the stresses σ_y and τ_{xy} and substitute them in (3.3) and (3.29) to obtain a set of linear

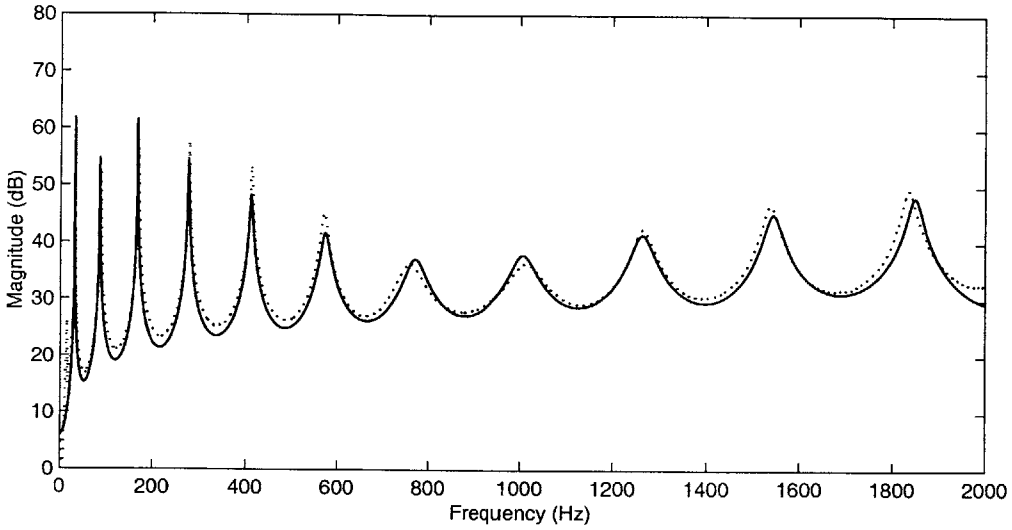

Figure 3.11: Comparison of the measured and predicted force-to-acceleration frequency responses for a sandwich beam with 0.05 mm steel auxiliary layer: measured (dotted), predicted (solid)

equations in V_n and W_n. The order of this system of equations is equal to the sum of the number of terms taken in the expansions (3.8) and (3.30). By solving these equations, we determine the coefficients V_n and W_n in the expansions (3.8) and (3.30). Next, we solve for the coefficients V_{01} and V_{02} of the rigid-body terms in the expansion (3.8) in a manner similar to that described in Section 3.3.3. We then combine the contributions from the rigid-body and flexible modes of the beam and write the non-dimensional accelerance R at the sensor location $x = x_s$ as

$$R = \frac{m\omega^2 VL}{F} = \left(\frac{m\omega^2 L}{F}\right)\left(V_{01} + V_{02}f(x_s) + \sum_{n=1}^{\infty} V_n\left[\alpha_n(x_s) + \beta_n(x_s)\right]\right) \tag{3.32}$$

Finally, we plot the force-to-acceleration frequency responses in Figures 3.11–3.13 and compare them with the measured responses. We again find good agreement between the experiments and model.

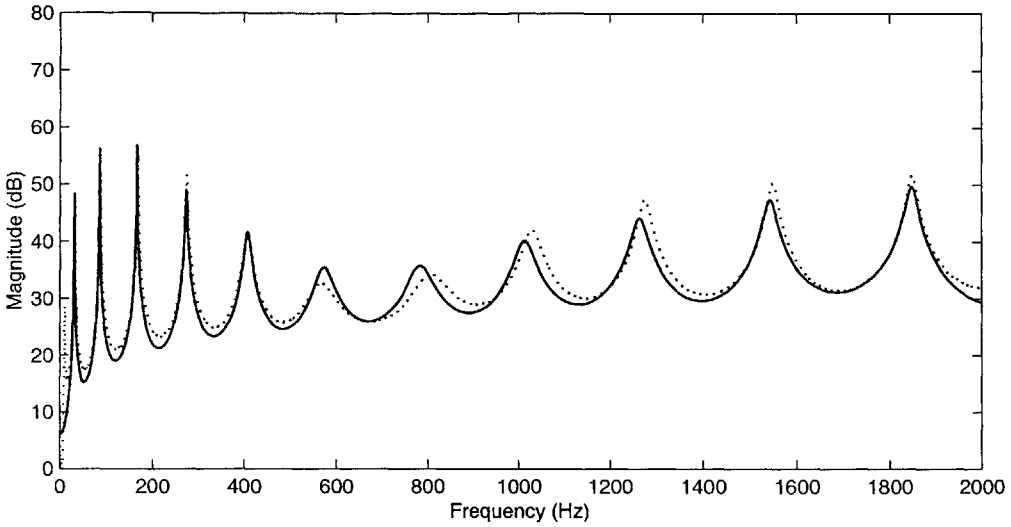

Figure 3.12: Comparison of the measured and predicted force-to-acceleration frequency responses for a sandwich beam with 0.10 mm steel auxiliary layer: measured (dotted), predicted (solid)

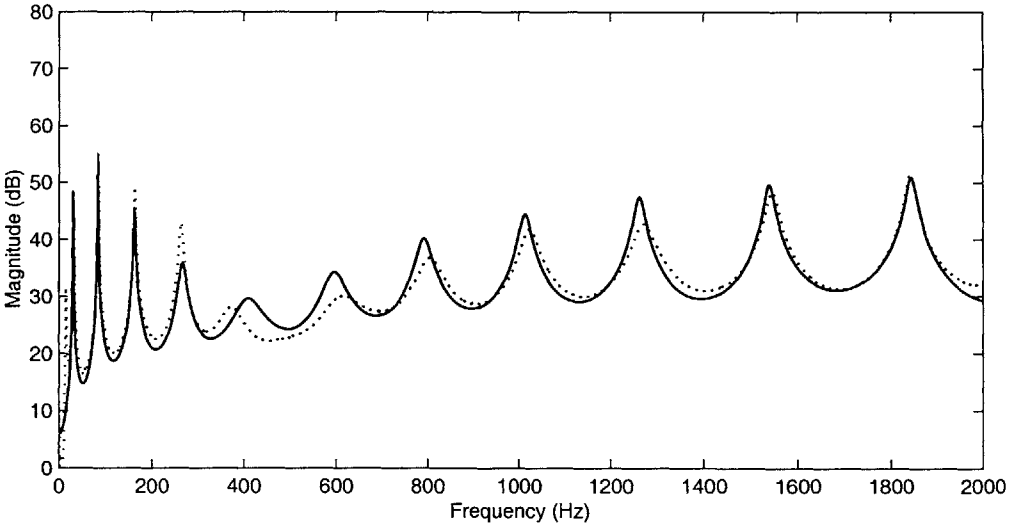

Figure 3.13: Comparison of the measured and predicted force-to-acceleration frequency responses for a sandwich beam with 0.81 mm aluminum auxiliary layer: measured (dotted), predicted (solid)

3.4 Chapter Summary

This chapter extends the ideas of the previous chapter to include low-wave-speed foams. We present results from several experiments in which flexural waves in a beam are damped over a broad range of frequencies. We use simple and linear wave-based continuum models to explain the phenomenon and develop approximate solutions using a complete modal expansion procedure. In the next chapter, we extend this approach to other types of vibration such as longitudinal waves and quasi-static stretching.

Chapter 4

Damping Longitudinal Waves and Quasi-Static Stretching using Low-Wave-Speed Media

4.1 Introduction

Chapters 2 and 3 show that flexural vibration can be significantly attenuated over a wide range of frequencies by coupling a structure to a low-wave-speed medium. This chapter extends that approach to damp longitudinal vibration in structures. These include both longitudinal waves and quasi-static stretching (described in Section 4.5).

In Section 4.2, we report on experiments in which longitudinal waves in a bar and quasi-static stretching of a membrane are damped when they are coupled to foam. Next, in Section 4.3, we develop simple linear models that explain this phenomenon.

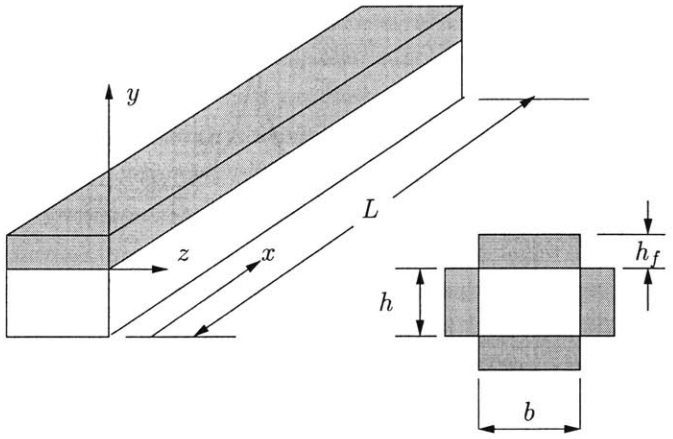

Figure 4.1: Schematic of the bar-foam system

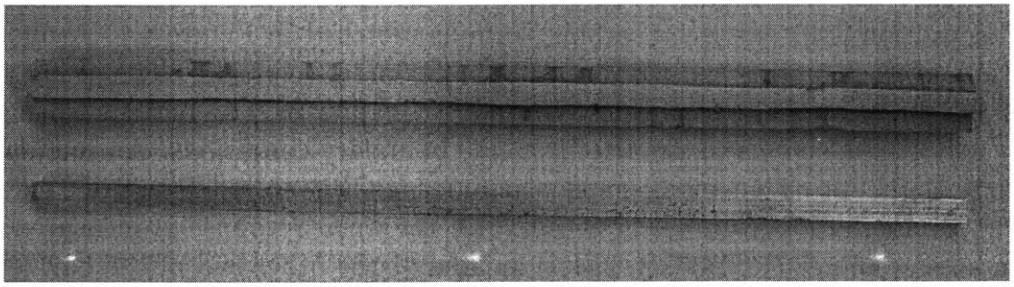

Figure 4.2: Photograph of the bar-foam system used in experiments

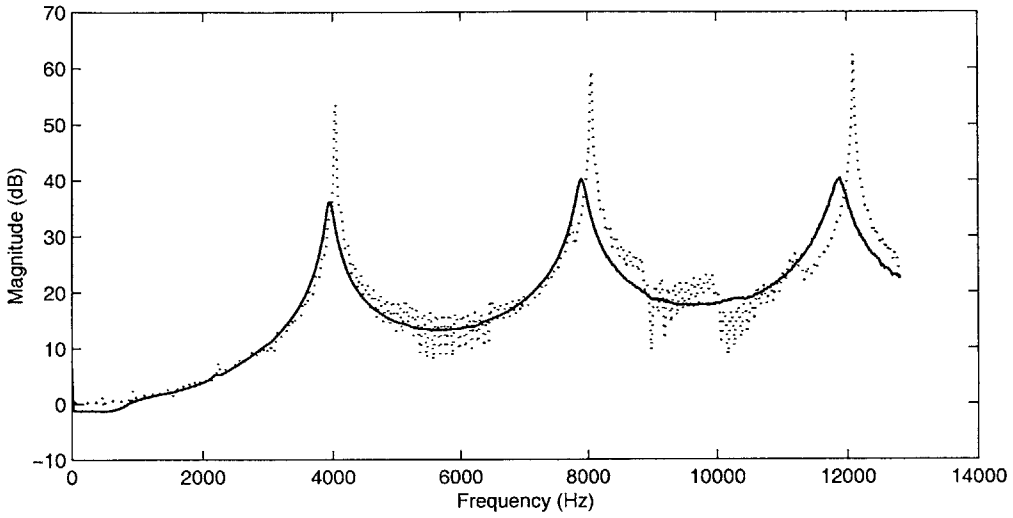

Figure 4.3: Measured force-to-acceleration frequency responses for a bar of length 635 mm under impact excitation: without foam (dotted) and with foam (solid)

4.2 Experiments

In this section, we describe two sets of experiments in which longitudinal modes of structures are damped by coupling them to a layer of low-density low-wave-speed medium. The first set of experiments consist of an aluminum bar (635×12.7×12.7 mm) coupled to 12.7 mm layers of EAR C-3201 (EAR Corporation [14]) energy-absorbing foam as sketched in Figure 4.1. A photograph of the bar with and without foam is shown in Figure 4.2. The properties of the material of the foam are provided in Chapter 3. The bar is suspended by soft elastic strings to simulate free-free boundary conditions. An impulsive excitation is provided by an impact hammer (PCB333A30 [40]) at one end of the bar in the longitudinal direction, and the axial response is measured by an accelerometer (PCB353B11 [40]) located at the other end of the bar.

In Figure 4.3, we plot the force-to-acceleration frequency response obtained for a bar of length 635 mm with and without the foam layer. As expected, the bar without foam exhibits very little damping, with $\zeta < 10^{-4}$ for each of the modes. When layers of foam of thickness 12.7 mm are glued onto the four faces of the bar there is a significant increase in in damping in all the modes.

In the second set of experiments, we study belt-foam systems of the con-

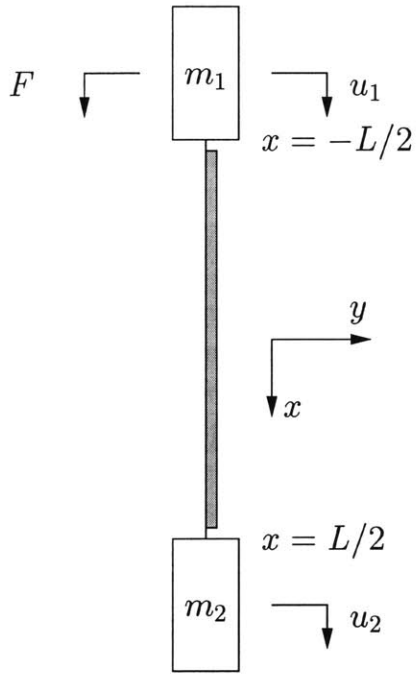

Figure 4.4: Schematic of the belt-foam system

figuration shown in Figure 4.4. The experiments consist of flat steel belts of lengths 1270 mm, 1041 mm, and 762 mm with a cross section 50.8×0.10 mm and clamped to aluminum blocks (76.2×76.2×25.4 mm) at each end. This system is suspended using light elastic strings to simulate free-free conditions. The top aluminum block is excited in the u_1 direction using an impact hammer (PCB333A30 [40]), and the response is measured by an accelerometer (PCB353B11 [40]) located at the top and bottom aluminum blocks.

In Figures 4.5, 4.7, and 4.9, we plot the collocated (i.e., excitation and measurement on the same block) force-to-acceleration frequency response of these systems with and without a foam layer attached to the belt segments. In the absence of the foam layer the resonant mode (complex poles) arising from the compliance of the belt and the inertias of the blocks exhibits very little damping. Likewise, we find that the complex zeros arising from the compliance of the belt and the inertia m_2 are also lightly damped. Several modes corresponding to transverse vibration of the blocks and belt are also apparent in these responses. When a layer of foam is attached to the belt segment as shown in Figure 4.4, significant damping is introduced into both the resonances (poles) and anti-resonances (zeros) of the system.

Next, in Figures 4.6, 4.8, 4.10, we plot the non-collocated (i.e., excitation and measurement on different blocks) force-to-acceleration frequency responses of the above system with and without a foam layer attached to the belt segment. As in the case of the collocated response, the addition of the foam layer results in significant attenuation of the resonant modes of the system. The damping ratios are found to be 3.5%, 3.8%, and 4.5% for the 1270 mm, 1041 mm, and 762 mm long belt segments, respectively.

4.3 Model

In this section, we develop models by which the responses measured in Section 4.2 can be predicted. As described in Section 3.3, we treat the foam as a lossy and isotropic continuum and write the wave equations governing the x-direction displacement u and y-direction displacement v in the frequency domain as:

$$(\lambda + 2G)u_{xx} + Gu_{yy} + (\lambda + G)v_{xy} + \rho\omega^2 u = 0 \quad (4.1)$$

$$Gv_{xx} + (\lambda + 2G)v_{yy} + (\lambda + G)u_{xy} + \rho\omega^2 v = 0 \quad (4.2)$$

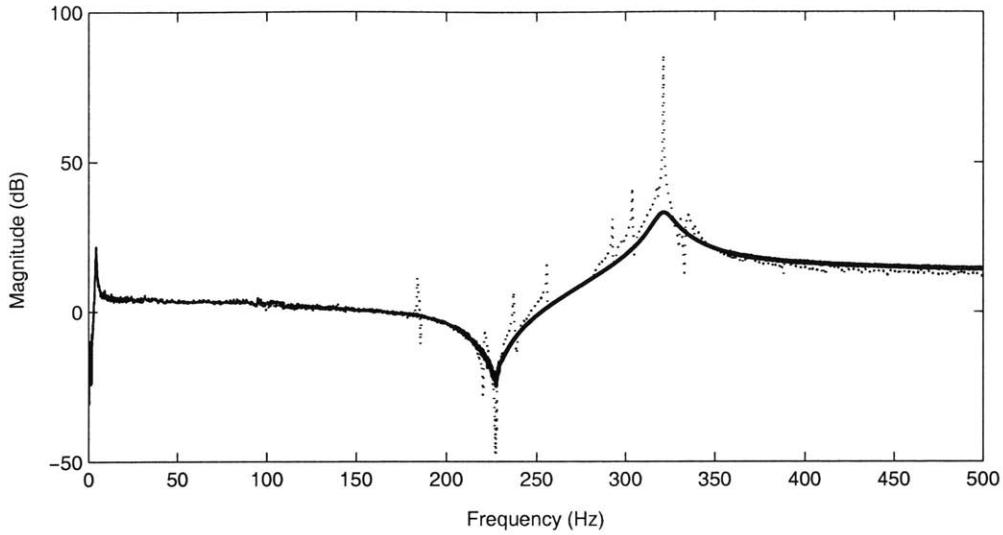

Figure 4.5: Measured collocated force-to-acceleration frequency responses for the belt-foam system of Figure 4.4 with 1270 mm long belt segment: without foam (dotted) and with foam (solid)

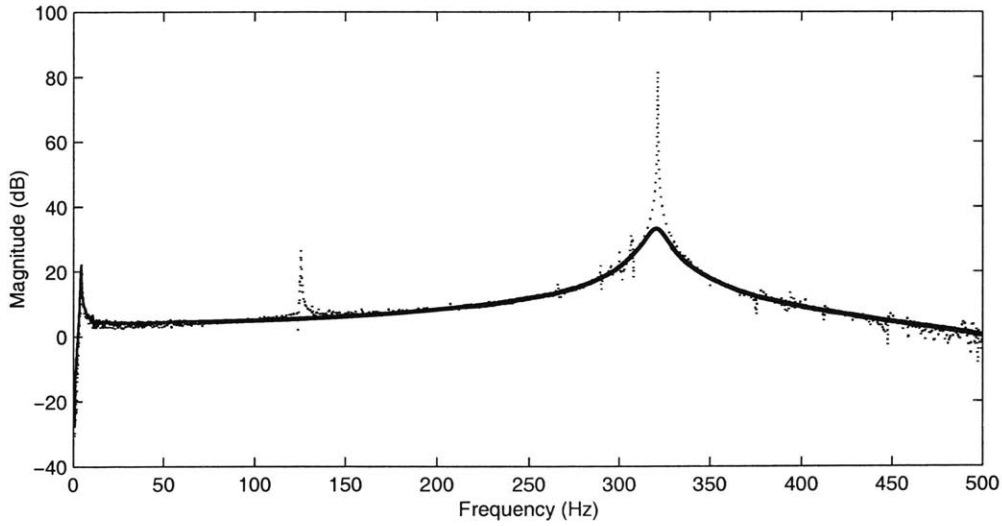

Figure 4.6: Measured non-collocated force-to-acceleration frequency responses for the belt-foam system of Figure 4.4 with 1270 mm long belt segment: without foam (dotted) and with foam (solid)

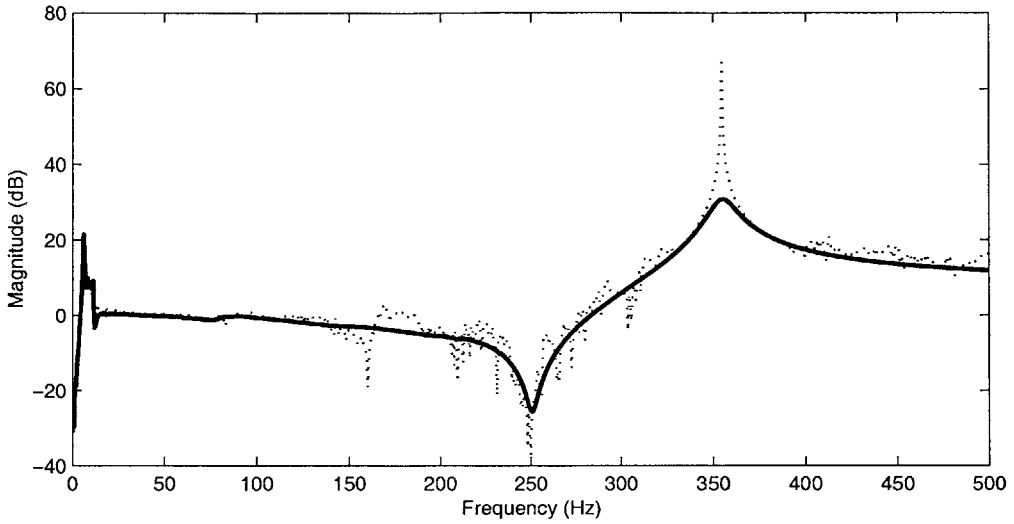

Figure 4.7: Measured collocated force-to-acceleration frequency responses for the belt-foam system of Figure 4.4 with 1041 mm long belt segment: without foam (dotted) and with foam (solid)

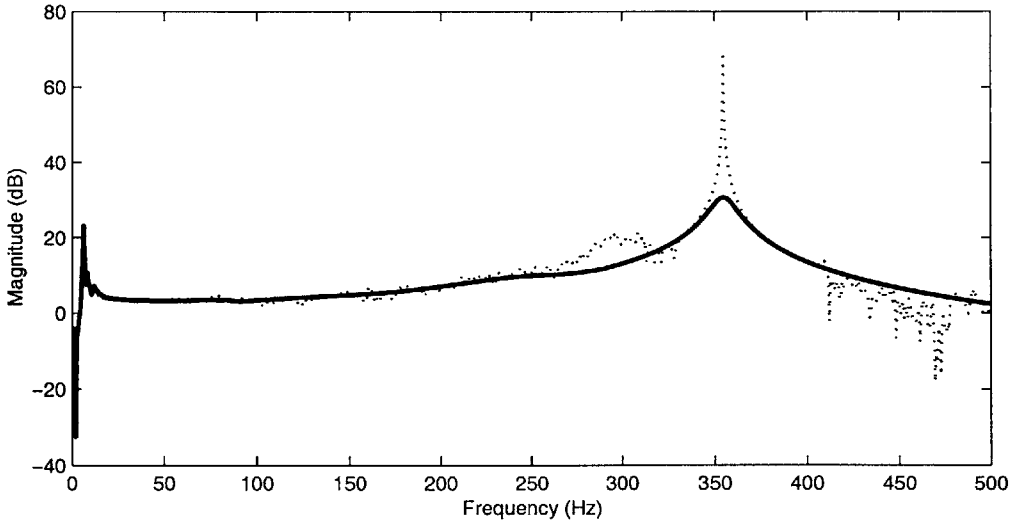

Figure 4.8: Measured non-collocated force-to-acceleration frequency responses for the belt-foam system of Figure 4.4 with 1041 mm long belt segment: without foam (dotted) and with foam (solid)

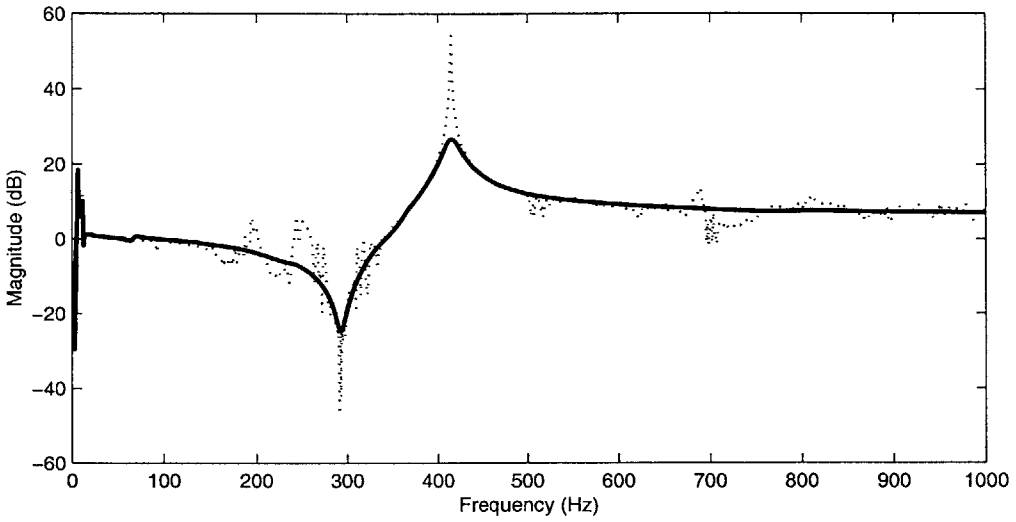

Figure 4.9: Measured collocated force-to-acceleration frequency responses for the belt-foam system of Figure 4.4 with 762 mm long belt segment: without foam (dotted) and with foam (solid)

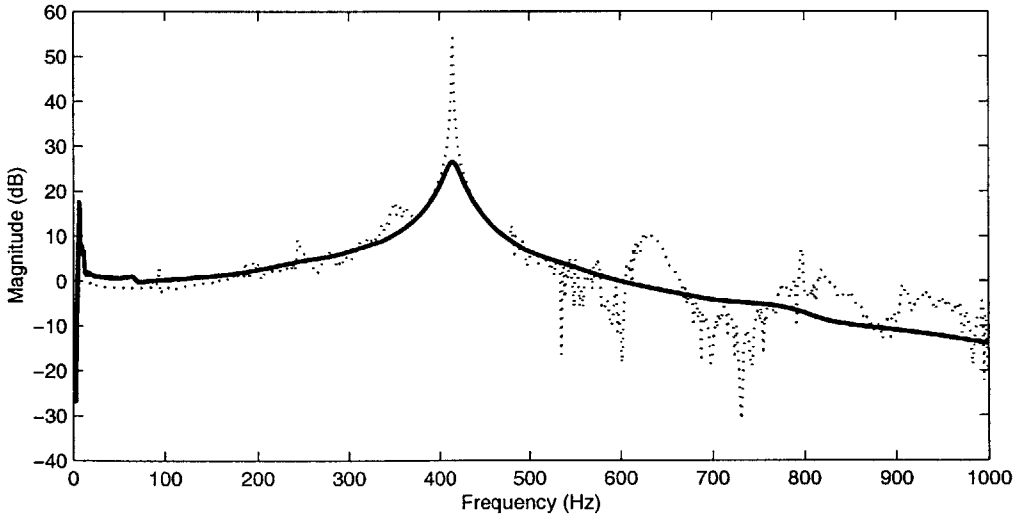

Figure 4.10: Measured non-collocated force-to-acceleration frequency responses for the belt-foam system of Figure 4.4 with 762 mm long belt segment: without foam (dotted) and with foam (solid)

where the subscripts denote partial differentiation and ρ, $\lambda = \nu E_f/(1+\nu)(1-2\nu)$, and G are respectively, the density, complex Lame constant, and complex shear modulus of the material of the foam.

4.4 Model for the Bar-Foam System

Consider steady vibration of the bar-foam system of Figure 4.1 under harmonic excitation at a frequency ω by a point force $\mathrm{Re}(F\delta(x)e^{j\omega t})$ in the x direction. We denote the vibratory displacement of the bar under such an excitation by $\mathrm{Re}(U(x,\omega)e^{j\omega t})$. At the interface between the bar and the foam (that is, at $y = 0$), the shear stress $\tau_{xy}(x,0,\omega)$ contributes to a force in the x direction. Making use of this interaction between the bar and the foam, we write the equation governing the longitudinal displacement U of the bar as:

$$EAU'' + m\omega^2 U + P\tau_{xy}(x,0,\omega) = 0 \tag{4.3}$$

where E is the Young's modulus of the material of the bar, A, m, and P are respectively, the area of cross section, mass per unit length, and perimeter of the cross section of the bar along which the foam is attached.

4.4.1 Boundary Conditions for the Foam

At the interface between the foam and bar (at $y = 0$), the displacements in the foam must match those of the surface of the bar. Hence we write

$$u(x,0,\omega) = U(x,\omega) \tag{4.4}$$
$$v(x,0,\omega) = 0 \tag{4.5}$$

At the free surface of the foam (at $y = h_f$), the normal and shear stresses must vanish. Hence we have

$$\lambda u_x(x,h_f,\omega) + (\lambda + 2G)v_y(x,h_f,\omega) = 0 \tag{4.6}$$
$$G(u_y(x,h_f,\omega) + v_x(x,h_f,\omega)) = 0 \tag{4.7}$$

4.4.2 Approximate Solution

As in the case of beam-powder and beam-foam systems of Chapters 2 and 3, closed-form solutions for (4.1)–(4.3) along with the boundary conditions (4.4)–(4.7) are generally difficult to obtain. Hence, we seek approximate solutions to

the coupled bar-foam system and expand the displacement of the bar in terms of the eigenfunctions of an undamped bar as

$$U(x,\omega) = U_0(\omega) + \sum_{n=1}^{\infty} U_n(\omega)\alpha_n(x) \tag{4.8}$$

The first term in the above expansion represents the pure translational mode of the bar. The remaining terms in the expansion represent the flexible modes of the bar where $\alpha_n(x)$ is the nth eigen mode of the bar. For $\alpha_n(x) = \cos(k_n x)$ for the free-free bar, and $k_n = n\pi/L$ is the wave number of the nth mode of the bar. In the following sections, we compute the contributions from the flexible and rigid-body modes to the accelerance of the bar-foam system in a manner similar to that of the beam-powder and beam-foam systems of Chapters 2 and 3.

Contribution of the Flexible Modes

As in the case of beam-powder and beam-foam systems, we use the form of the boundary conditions (4.4)–(4.7) to obtain the following compatible displacements in the foam:

$$u(x,y,\omega) = \sum_{n=1}^{\infty} \phi_n(y,\omega)\alpha_n(x) \tag{4.9}$$

$$v(x,y,\omega) = \sum_{n=1}^{\infty} \psi_n(y,\omega)\alpha_n'(x)/k_n \tag{4.10}$$

where the prime denotes the first derivative, and ϕ and ψ are yet to be determined functions of y and ω. Substituting the above expansions for u and v into the wave equations (4.1) and (4.2), we obtain the following system of second-order ordinary differential equations:

$$\phi_n'' = k_n\left(\frac{\lambda+G}{G}\right)\psi_n' + \left(\frac{k_n^2(\lambda+2G)-\rho\omega^2}{G}\right)\phi_n \tag{4.11}$$

$$\psi_n'' = -k_n\left(\frac{\lambda+G}{\lambda+2G}\right)\phi_n' + \left(\frac{k_n^2 G-\rho\omega^2}{\lambda+2G}\right)\psi_n \tag{4.12}$$

By solving the above equations subject to the boundary conditions (4.4)–(4.7), we obtain solutions for the functions ϕ_n and ψ_n. We then use these functions

to compute the shear stress τ_{xy} at the interface of the bar and the foam and substitute it into (4.3) to solve for the U_n. In order to do so, we multiply (4.3) by $\alpha_n(x)$ and integrate the resulting expression between 0 and L to obtain the following expression for the contribution from the nth mode of the bar to the non-dimensional accelerance R of the system:

$$\frac{m\omega^2 U_n L}{F} = \frac{2m\omega^2 \alpha_n(0)}{EAk_n^2 - m\omega^2 - PG(\phi_n'(0,\omega) - k_n\psi_n'(0,\omega))} \tag{4.13}$$

Contribution of the Rigid-Body Mode

When the bar undergoes pure translational motion, planes waves of distortion are excited in the foam and the displacement v is zero everywhere in the foam. As a result the wave equations (4.1)–(4.2) reduce to the following simple form:

$$u_{yy} + k_s^2 u = 0 \tag{4.14}$$

where $k_s = \omega\sqrt{\rho/G}$ is the complex wave number associated with the propagation of shear waves in the foam. We then solve the above equation subject to the boundary conditions (4.4)–(4.7) to obtain the displacement $u(y,\omega)$ in the foam. From this displacement, we compute the shear stress exerted by the foam at the bar-foam interface and obtain the following expression for the contribution from the rigid-body translation to the non-dimensional accelerance R of the system:

$$\frac{m\omega^2 U_0 L}{F} = -\frac{m\omega^2}{m\omega^2 + PGk_s \tan(k_s h_f)} \tag{4.15}$$

The Total Response

Next, after computing the contributions to the displacement of the bar from the flexible and rigid-body modes, we write the non-dimensional accelerance R at the location of the sensor L as

$$R = \frac{m\omega^2 UL}{F} = \frac{m\omega^2 U_0 L}{F} + \sum_{n=1}^{\infty} \frac{m\omega^2 U_n L}{F}\alpha_n(L) \tag{4.16}$$

Finally, we plot in Figure 4.11 the force-to-acceleration frequency response and compare it with the measured response. We find that there is good agreement between the measured and predicted frequency responses.

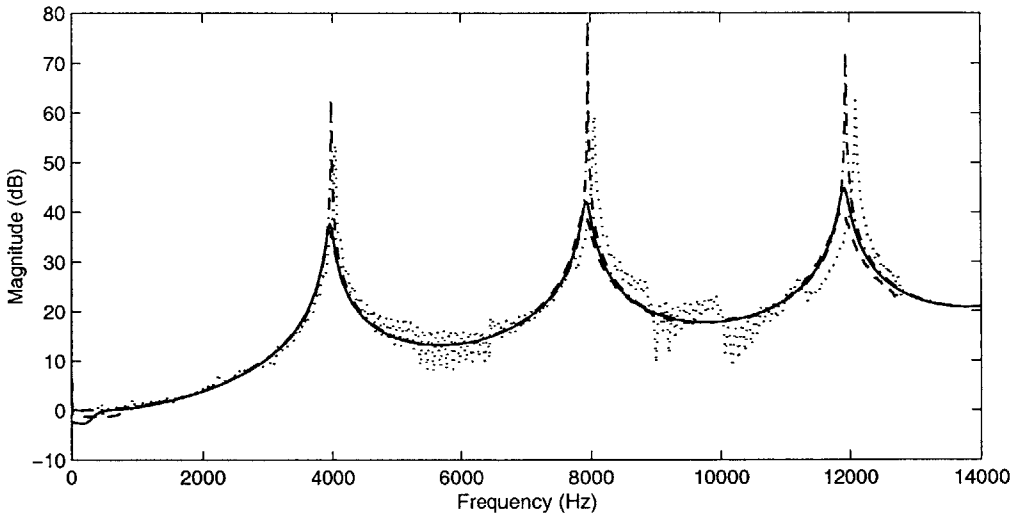

Figure 4.11: Comparison of the measured and predicted force-to-acceleration frequency responses: measured without foam (dotted), measured with foam (dashed), predicted without foam (dash-dot), and predicted with foam (solid)

4.5 Model for Belt-Foam System

Consider steady harmonic vibration of the belt-foam system sketched in Figure 4.4 at a frequency ω, where the vibratory displacements of the inertias m_1 and m_2 in the x direction are given by $\mathrm{Re}(u_1(\omega)e^{j\omega t})$ and $\mathrm{Re}(u_2(\omega)e^{j\omega t})$, respectively. The complex variables $u_1(\omega)$ and $u_2(\omega)$ each represent the magnitude and the phase of motion as a function of the frequency ω. The longitudinal displacement of the belt varies along the length of the belt and hence is written as $\mathrm{Re}(u_b(x,\omega)e^{j\omega t})$. At the interface between the foam and belt (at $y = 0$) the shear stress $\tau_{xy}(x,0,\omega)$ contributes to a force in the x direction. Taking account of this interaction between the belt and foam, we write the equation governing the longitudinal displacement u_b of the belt as:

$$EAu_b'' + m\omega^2 u_b + b\tau_{xy}(x,0,\omega) = 0 \tag{4.17}$$

where E is the Young's modulus of the material of the belt, A, m, and b are respectively, the area of cross section, mass per unit length, and width of the belt.

4.5.1 Boundary Conditions for the Foam

At the interface between the foam and belt (at $y = 0$), the displacements in the foam must match those of the surface of the belt. Hence we obtain

$$u(x, 0, \omega) = u_b(x, \omega) \tag{4.18}$$
$$v(x, 0, \omega) = 0 \tag{4.19}$$

At the free surface of the foam (at $y = h_f$), the normal and shear stresses must vanish. Hence we have

$$\lambda u_x(x, h_f, \omega) + (\lambda + 2G)v_y(x, h_f, \omega) = 0 \tag{4.20}$$
$$G(u_y(x, h_f, \omega) + v_x(x, h_f, \omega)) = 0 \tag{4.21}$$

4.5.2 Equations of Motion for m_1 and m_2

The mass m_1 is subject to a force exerted by the belt (at $x = -L/2$) in addition to an external force $\mathrm{Re}(F(\omega)e^{j\omega t})$. The equation of motion for the mass m_1 therefore takes the form

$$F + EAu_b'(-L/2, \omega) = -m_1\omega^2 u_1 \tag{4.22}$$

Likewise, the mass m_2 is subject to a force exerted by the belt at $x = L/2$. We therefore write

$$EAu_b'(L/2, \omega) = m_2\omega^2 u_2 \tag{4.23}$$

4.5.3 Solution Approach

To obtain the collocated and the non-collocated frequency responses for the belt-foam system, we must simultaneously solve the equations of motion for the belt and two masses ((4.17), (4.22), and (4.23)) and the wave equations (4.1)–(4.2) subject to the boundary conditions (4.18)–(4.18)). As in the case of the previous examples of the bar and beam it is generally difficult to obtain closed-form solutions to the above problem and therefore we seek approximate solutions. To this end, we use the displacement associated with the undamped belt to compute the shear stress $\tau_{xy}(x, 0, \omega)$ imposed by the foam on the belt.

Because the frequency of the first longitudinal resonance of the system is much lower than that of the longitudinal wave propagation in the belt, we can approximate the associated mode shape by that obtained from a quasi-static

deformation of the system. Under such conditions, the displacement $\hat{u}_b(x,\omega)$ of the undamped belt varies approximately linearly with x over the frequency range of interest and is given by

$$\hat{u}_b(x,\omega) = \left(\frac{u_2(\omega) - u_1(\omega)}{L}\right) x + \left(\frac{u_2(\omega) + u_1(\omega)}{2}\right) \tag{4.24}$$

Next, we calculate the shear stress $\tau_{xy}(x,0,\omega)$ when the above displacement is imposed on the foam at the belt-foam interface.

Contribution of the Rigid-Body Term

When the displacement of the belt is given by the constant term of (4.24), plane waves of shear are excited in the foam and the displacement v is zero everywhere in the foam. As a result the wave equations (4.1)–(4.2) reduce to the following simple form:

$$u_{yy} + k_s^2 u = 0 \tag{4.25}$$

Next, we solve the above equation subject to the boundary conditions (4.18)–(4.21) to obtain the displacement $u(y,\omega)$ in the foam . We then calculate the shear stress $\tau^0_{xy}(x,0,\omega)$ at the belt-foam interface arising from the constant term in the displacement of the belt as

$$\tau^0_{xy}(x,0,\omega) = Gu_y = Gk_s \tan(k_s h_f) \left(\frac{u_2(\omega) + u_1(\omega)}{2}\right) \tag{4.26}$$

Contribution from the Stretching Term

When the displacement of the belt is given by the linear term in (4.24), we expect the displacement u in the foam to be linear in the x direction and the displacement v to be a function of only the y coordinate. Therefore, we write the following compatible displacements in the foam:

$$u(x,y,\omega) = x\phi(y) \tag{4.27}$$
$$v(x,y,\omega) = \psi(y) \tag{4.28}$$

where ϕ and ψ are yet to be determined functions of y. Substituting the above expressions for u and v in the wave equations (4.1) and (4.2), we obtain the

following second-order ordinary differential equations ϕ and ψ:

$$\phi'' = -\left(\frac{\rho\omega^2}{G}\right)\phi \tag{4.29}$$

$$\psi'' = -\left(\frac{\lambda+G}{\lambda+2G}\right)\phi' - \left(\frac{\rho\omega^2}{\lambda+2G}\right)\psi \tag{4.30}$$

Next, we solve the above equations subject to the boundary conditions (4.18)–(4.21) to obtain the functions $\phi(y)$ and $\psi(y)$. We then calculate the shear stress $\tau^1_{xy}(x,0,\omega)$ at the belt-foam interface arising from the linear term in the displacement of the belt as

$$\tau^1_{xy}(x,0,\omega) = G(u_y + v_x) = G\phi'(0)x\left(\frac{u_2(\omega)-u_1(\omega)}{L}\right) \tag{4.31}$$

We now obtain the total shear stress $\tau_{xy}(x,0,\omega)$ at the interface of the belt and the foam as:

$$\tau_{xy}(x,0,\omega) = \tau^0_{xy}(x,0,\omega) + \tau^1_{xy}(x,0,\omega) \tag{4.32}$$

Dynamic Equations

Based on the discussion provided in Section 4.5.3, we neglect the inertia of the belt in (4.17) by noting that the frequency range of interest is much smaller than that at which longitudinal waves propagate in the belt. Next, we substitute the shear stress at the belt-foam interface given in (4.32) into the belt-displacement equation (4.17) to obtain

$$EAu_b'' + b\left[G\phi'(0)x\left(\frac{u_2(\omega)-u_1(\omega)}{L}\right) + Gk_s\tan(k_sh_f)\left(\frac{u_2(\omega)+u_1(\omega)}{2}\right)\right] = 0 \tag{4.33}$$

We then integrate the above expression twice with respect to x and use the boundary conditions $u_b(x=-L/2)=u_1$ and $u_b(x=L/2)=u_2$ to obtain the following expressions for the slope of the displacement u_b at the two ends of the belt:

$$EAu_b'(-L/2) = k(u_2-u_1) + \hat{k}(u_2+u_1) \tag{4.34}$$

$$EAu_b'(+L/2) = k(u_2-u_1) - \hat{k}(u_2+u_1) \tag{4.35}$$

where the expressions for k and $\hat{k}$ are given by

$$k = \frac{EA}{L} - \frac{bG\phi'(0)L}{12} \tag{4.36}$$

$$\hat{k} = \frac{Gk_s bL\tan(k_s h_f)}{4} \tag{4.37}$$

Next, we substitute these slopes into (4.22) and (4.23) to obtain the following equations governing the dynamics of the masses m_1 and m_2:

$$-\omega^2 m_1 u_1 + k(u_1 - u_2) - \hat{k}(u_1 + u_2) = F \tag{4.38}$$

$$-\omega^2 m_2 u_2 + k(u_2 - u_1) - \hat{k}(u_2 + u_1) = 0 \tag{4.39}$$

The parameter k represents the complex stiffness of the belt with foam, and the parameter $\hat{k}$ accounts for the "apparent mass" of the foam. The latter is expected to be small except at frequencies where standing shear waves can be set up through the thickness of the foam.

Finally, we plot in Figures 4.12, 4.14, and 4.16 the collocated frequency responses and in Figures 4.13, 4.15, 4.17 the non-collocated frequency responses and compare them with the corresponding experimental results. We find generally good agreement between the measured and predicted responses. But as the length of the belt segment gets shorter the predicted damping is found to be smaller than that of the measured. This increase in damping in the measurements could possibly arise from a length-wise coupling between the foam in addition to the thickness-wise coupling that is outlined in the model.

4.6 Chapter Summary

This chapter presents experimental and analytical results that show significant damping enhancements in the longitudinal modes of structures by coupling them to low-wave-speed foam. The results of the previous chapters can be combined with the present one to design damping treatments for "built-up" structures.

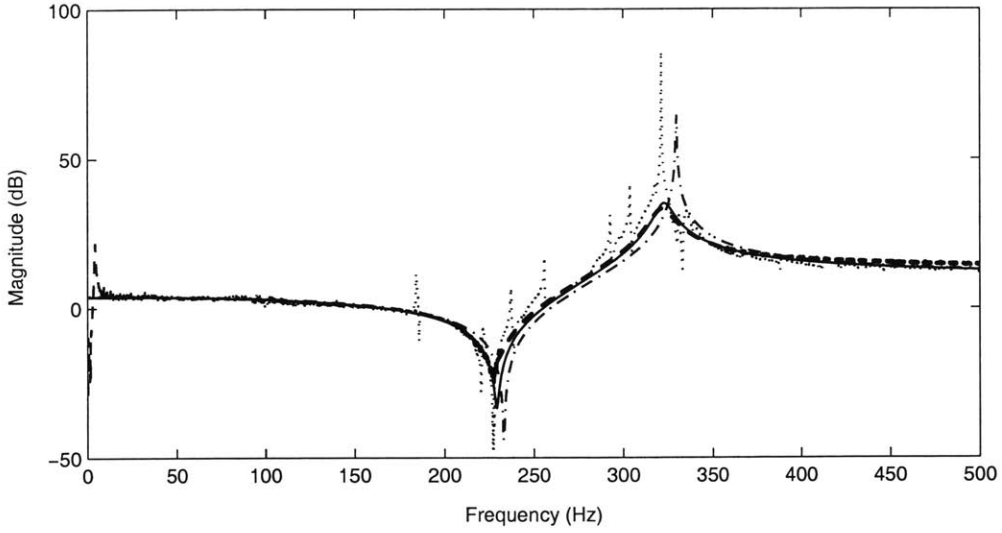

Figure 4.12: Comparison of the measured and predicted collocated force-to-acceleration frequency responses for the 1270 mm long belt segment : measured without foam (dotted), measured with foam (dashed), predicted without foam (dash-dot), and predicted with foam (solid)

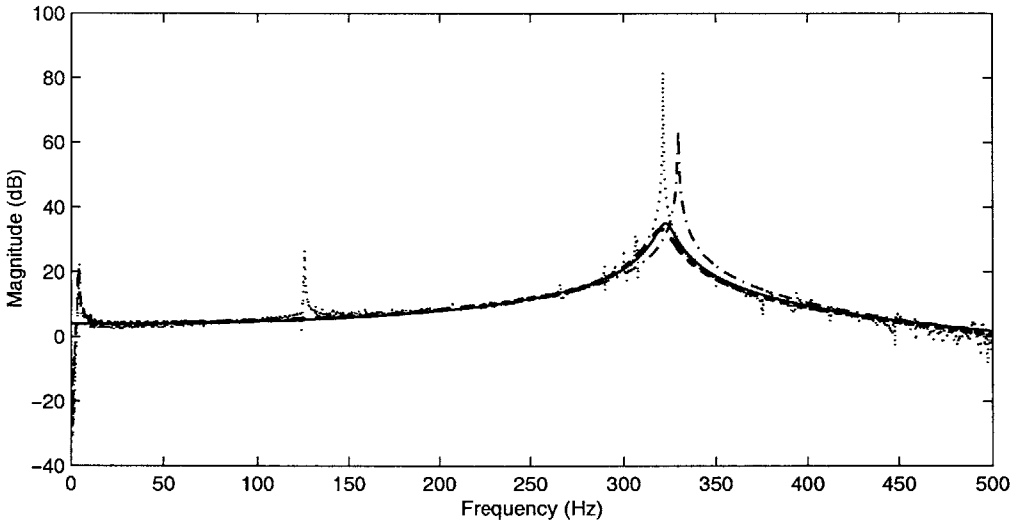

Figure 4.13: Comparison of the measured and predicted non-collocated force-to-acceleration frequency responses for the 1270 mm long belt segment : measured without foam (dotted), measured with foam (dashed), predicted without foam (dash-dot), and predicted with foam (solid)

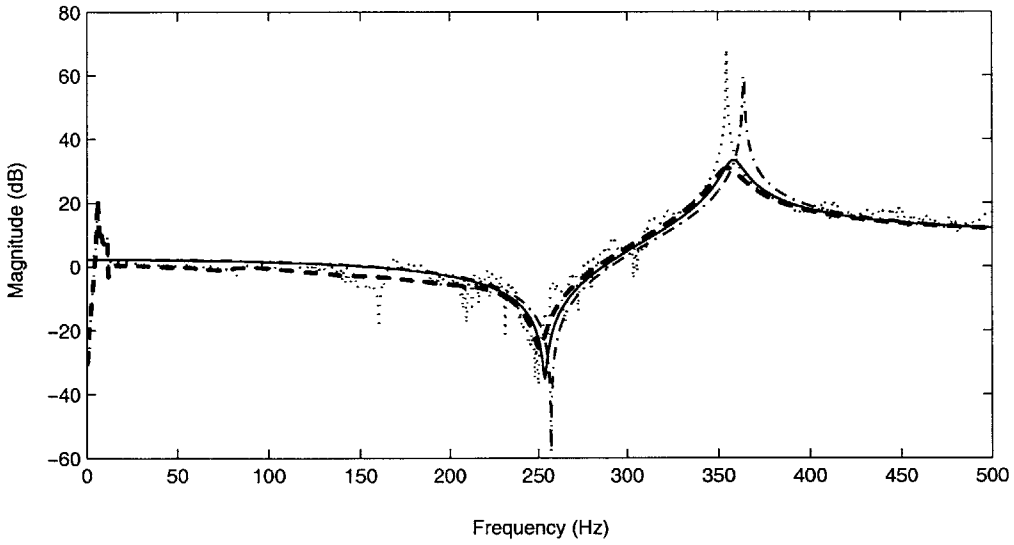

Figure 4.14: Comparison of the measured and predicted collocated force-to-acceleration frequency responses for the 1041 mm long belt segment : measured without foam (dotted), measured with foam (dashed), predicted without foam (dash-dot), and predicted with foam (solid)

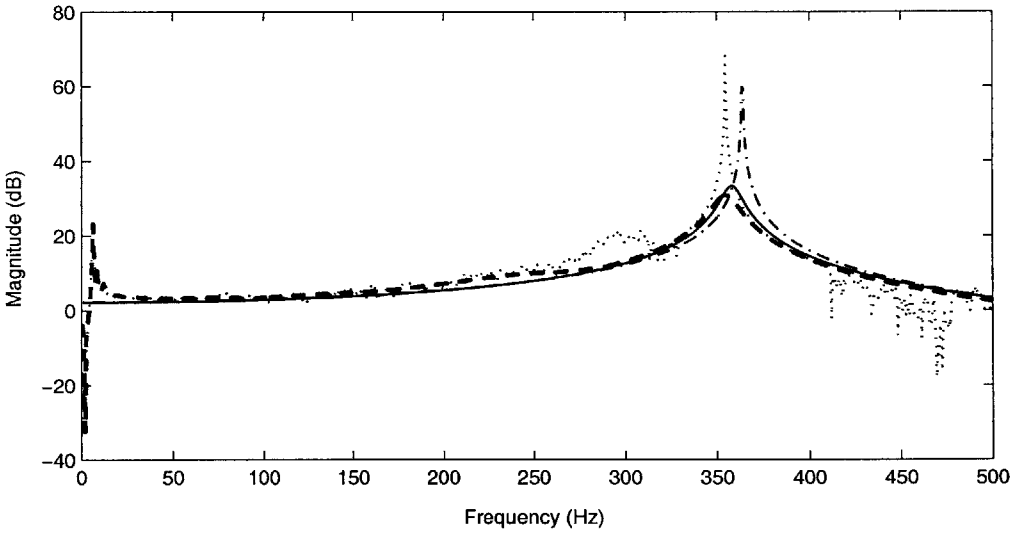

Figure 4.15: Comparison of the measured and predicted non-collocated force-to-acceleration frequency responses for the 1041 mm long belt segment : measured without foam (dotted), measured with foam (dashed), predicted without foam (dash-dot), and predicted with foam (solid)

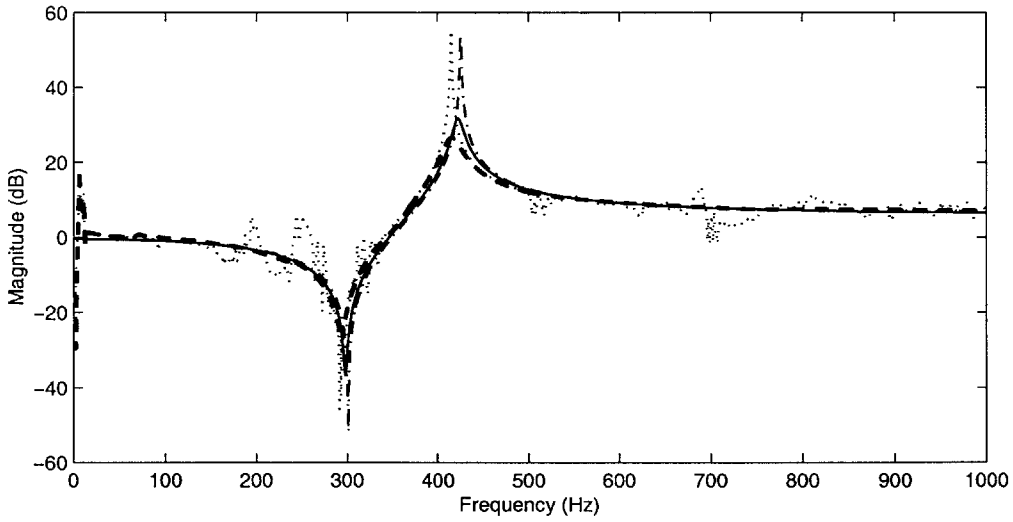

Figure 4.16: Comparison of the measured and predicted collocated force-to-acceleration frequency responses for the 762 mm long belt segment : measured without foam (dotted), measured with foam (dashed), predicted without foam (dash-dot), and predicted with foam (solid)

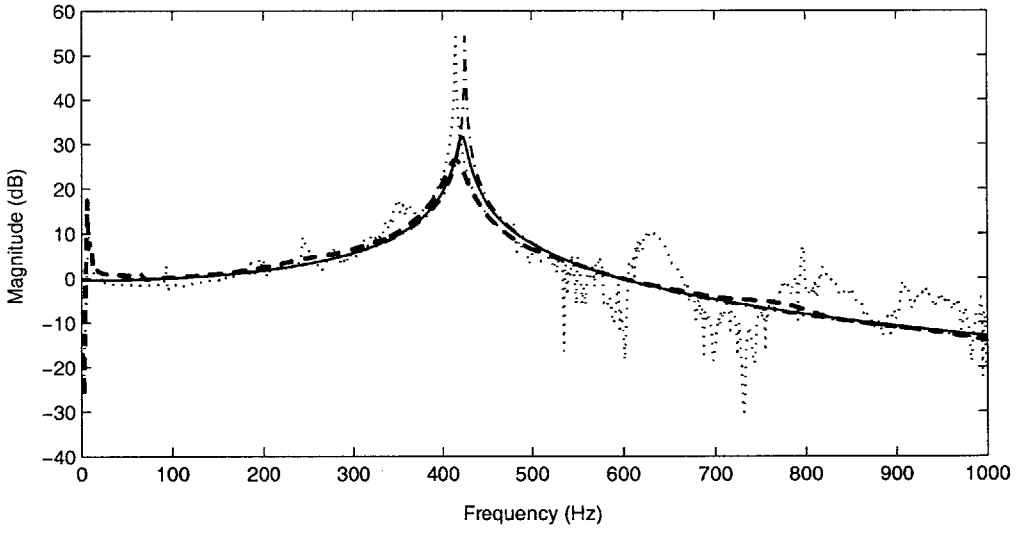

Figure 4.17: Comparison of the measured and predicted non-collocated force-to-acceleration frequency responses for the 762 mm long belt segment : measured without foam (dotted), measured with foam (dashed), predicted without foam (dash-dot), and predicted with foam (solid)

CHAPTER 5

Simplified Models and Scaling Laws for Low-Wave-Speed Media

5.1 Introduction

The models presented in Chapters 2, 3, and 4 capture the physics of the damping phenomenon arising from the coupling of a structure to a low-wave-speed medium reasonably well. This gives confidence to our approach of modeling the behavior of powder or foam as continua in which waves can propagate. However, these models are based on a complete modal expansion and are difficult to use for design. Therefore, in this chapter we provide some simplified methods based on energy and complex-wave-number approaches that can adequately capture the phenomenon and are tractable for design purposes. Finally, we provide scaling laws for the attainable damping in terms of the key non-dimensional parameters of the system.

5.1.1 Loss Factor

Loss factor η is one of the most common measures of energy dissipation. It is defined as the ratio of the average energy dissipated per radian to the peak potential energy during a cycle of steady harmonic motion. It is computed

from

$$\eta = \frac{W}{2\pi U_p} \tag{5.1}$$

where W is the energy dissipated per cycle and U_p is the peak potential energy.

The energy dissipated in traditional materials of construction (such as steel, aluminum, or cast iron) is usually negligible. Hence for the systems coupled to foam (such as the ones described in Chapters 3 and 4), we calculate the loss factor η by considering the energy dissipation to primarily occur in the foam. Under steady harmonic motion at a frequency ω the energy dissipated W in the foam per cycle is obtained by integrating the summation of the products of stress $\mathrm{Re}(\sigma(\mathbf{r},\omega)e^{j\omega t})$ and corresponding rates of strain $\mathrm{Re}(j\omega\epsilon(\mathbf{r},\omega)e^{j\omega t})$ with respect to temporal and spatial coordinates as

$$W = \int_{\mathcal{V}} \int_0^{2\pi/\omega} \sum \left[\mathrm{Re}(\sigma(\mathbf{r},\omega)e^{j\omega t})\mathrm{Re}(j\omega\epsilon(\mathbf{r},\omega)e^{j\omega t})\right]\, dt\, d\mathcal{V} \tag{5.2}$$

where $\mathcal{V}$ is the volume of foam, $\mathbf{r}$ is the position vector of the volume element $d\mathcal{V}$ and the complex quantities σ and ϵ represent the magnitude and phase of stress and strain, respectively, and the summation is over all the components of stress and strain. On performing the integration with respect to time the above equation reduces to the following simple form:

$$W = \pi \mathrm{Im}\left[\int_{\mathcal{V}} \sum \sigma(\mathbf{r},\omega)\bar{\epsilon}(\mathbf{r},\omega)\, d\mathcal{V}\right] \tag{5.3}$$

where the bar denotes complex conjugation and the summation is over all the components of stress and strain.

Alternately, one can define the loss factor in terms of the spatial decay of a wave as it propagates in a lossy medium. For example, when a longitudinal wave propagates in a bar whose complex modulus is $E(1+j\eta)$, the amplitude of the wave decays by a factor of $\exp[2\pi(\sqrt{1+\eta^2}-1)/(\sqrt{1+\eta^2}+1)]$ over one wavelength. Hence we write the following expression for the loss factor

$$\eta = \frac{\mathrm{Im}(1/\tilde{k}_r^2)}{\mathrm{Re}(1/\tilde{k}_r^2)} \tag{5.4}$$

where $\tilde{k}_r$ is the complex wave number associated with the longitudinal wave propagation in the bar. Likewise, when a flexural wave with a complex wave

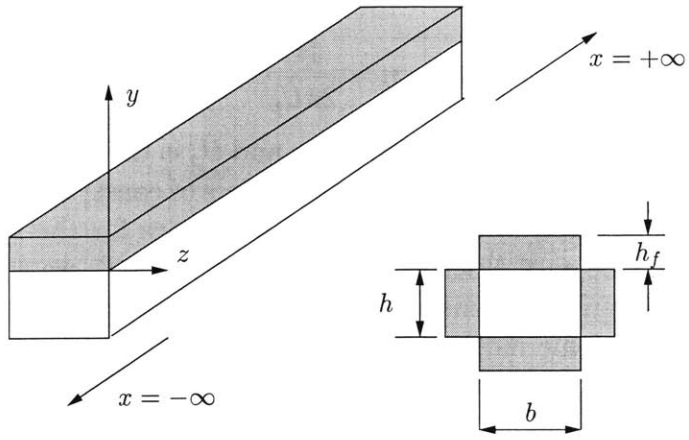

Figure 5.1: Schematic of infinite bar-foam systems

number $\tilde{k}_b$ propagates in a beam, the associated loss factor η can be evaluated as:

$$\eta = \frac{\mathrm{Im}(1/\tilde{k}_b^4)}{\mathrm{Re}(1/\tilde{k}_b^4)} \tag{5.5}$$

Therefore, based on the mode of wave propagation one can use the above relations (5.4) and (5.5) to obtain the corresponding loss factors.

5.2 Simplified Model for Bar-Foam Systems

In this section, we study the dynamics of bar-foam systems of infinite length extending from $x = -\infty$ to $x = +\infty$ (as shown in Figure 5.1) and undergoing steady harmonic vibration at a frequency ω in the longitudinal direction. As described in Chapter 4, we denote the vibratory displacement of the bar undergoing such a motion by $\mathrm{Re}(U(x,\omega)e^{j\omega t})$ and the displacements in the foam in the x and y directions by $\mathrm{Re}(u(x,\omega)e^{j\omega t})$ and $\mathrm{Re}(v(x,\omega)e^{j\omega t})$, respectively. In order to obtain estimates for damping in such systems, we must solve the coupled wave equations (4.1) and (4.2) subject to the boundary conditions (4.4)–(4.7).

As described in Section 4.4.2, closed-form solutions are generally difficult to obtain for such problems and therefore we seek approximate solutions. To this end, we use the displacement of the undamped bar to solve for the wave

propagation in the foam and then compute the loss factor using either the energy or wave approach. Hence, we write the displacement U of the bar as

$$U(x,\omega) = U_+(\omega)e^{-jk_r x} + U_-(\omega)e^{jk_r x} \tag{5.6}$$

where the first and second terms represent forward and backward traveling longitudinal waves in the bar and k_r is the associated wave number, given by the following familiar dispersion relation of the bar:

$$k_r^2 = \frac{\omega^2 m}{EA} \tag{5.7}$$

where m, E, and A are respectively the mass per unit length, Young's modulus, and area of cross section of the bar. Next we write compatible displacements in the foam as

$$u(x,y,\omega) = (U_+(\omega)e^{-jk_r x} + U_-(\omega)e^{jk_r x})\phi(y) \tag{5.8}$$

$$v(x,y,\omega) = -j(U_+(\omega)e^{-jkx} - U_-(\omega)e^{jkx})\psi(y) \tag{5.9}$$

where $\phi(y)$ and $\psi(y)$ are yet to be determined functions. Substituting the above expressions for u and v in the wave equations (4.1) and (4.2), we obtain the following second-order ordinary differential equations for ϕ and ψ:

$$\phi'' = k_r\left(\frac{\lambda+G}{G}\right)\psi' + \left(\frac{(\lambda+2G)k_r^2 - \rho\omega^2}{G}\right)\phi \tag{5.10}$$

$$\psi'' = -k_r\left(\frac{\lambda+G}{\lambda+2G}\right)\phi' + \left(\frac{Gk_r^2 - \rho\omega^2}{\lambda+2G}\right)\psi \tag{5.11}$$

where primes denote the first derivative. Next we solve the above equations subject to the boundary conditions (4.4)–(4.7) to obtain the functions $\psi(y)$ and $\phi(y)$.

5.2.1 Energy Approach

In this section, we use the solutions for ϕ and ψ to determine the expressions for the stresses and strains in the foam. We then evaluate the energy dissipation W and peak potential energy U_p and substitute them into (5.1) to obtain an expression for the loss factor of the system.

Energy Dissipation

The normal stress σ_x can be evaluated for an isotropic continuum in a two-dimensional case using the following familiar expression (e.g., Timoshenko and Goodier [49])

$$\sigma_x(x,y,\omega) = (\lambda + 2G)\frac{\partial u}{\partial x}(x,y,\omega) + \lambda\frac{\partial v}{\partial y}(x,y,\omega) \tag{5.12}$$

The normal strain ϵ_x is defined as the partial derivative of the displacement u with respect to x. Making use of these definitions and similar ones for the other components and the expressions for foam displacements (5.8) and (5.9), we write the following expressions for stresses and strains in the foam:

$$\sigma_x = [k_r(\lambda + 2G)\phi + \lambda\psi']\,U'/k_r \quad ; \quad \epsilon_x = \phi U' \tag{5.13}$$

$$\sigma_y = [k_r\lambda\phi + (\lambda + 2G)\psi']\,U'/k_r \quad ; \quad \epsilon_y = \psi' U'/k_r \tag{5.14}$$

$$\tau_{xy} = G\,[\phi' - k_r\psi]\,U \quad ; \quad \gamma_{xy} = [\phi' - k_r\psi]\,U \tag{5.15}$$

Because the bar-foam system is of infinite extent and the associated motion is periodic in x, we compute the loss factor η by evaluating the energy dissipation W and peak potential energy U_p over a wavelength of the bar. Using (5.3), we write the energy dissipated W per harmonic cycle for the bar-foam systems as

$$W = \pi P\,\mathrm{Im}\left[\int_0^{h_f}\int_0^{2\pi/k_r} (\sigma_x\bar{\epsilon}_x + \sigma_y\bar{\epsilon}_y + \tau_{xy}\bar{\gamma}_{xy})\,dx\,dy\right] \tag{5.16}$$

Substituting the expressions for stresses and strains from (5.13)–(5.15) into the above equation (5.16), we obtain the following expression for the energy dissipated W over a wavelength of the beam and per cycle of harmonic motion:

$$\begin{aligned} W \;=\; & \left(4\pi^2 P U_+ U_-/k_r\right)\,\mathrm{Im}\left[\int_0^{h_f}\left[(\lambda+2G)(k_r^2|\phi|^2 + |\psi'|^2) + 2\lambda k_r \mathrm{Re}(\bar{\phi}\psi')\right.\right. \\ & \left.\left. + G(|\phi'|^2 + k_r^2|\psi|^2 - 2k_r\mathrm{Re}(\phi'\bar{\psi}))\right]\,dy\right] \end{aligned} \tag{5.17}$$

Peak Potential Energy and Loss Factor

The peak potential energy U_p of the bar-foam system in a harmonic cycle over a wavelength of the beam can be computed as a sum of the peak strain energy in the beam and that in the foam. The former can be obtained from the familiar

expressions for the strain energy in a bar (e.g., Crandall [11]) and the later from those of an isotropic continuum (e.g., Timoshenko and Goodier [49]). Using these expressions, we write the peak potential energy U_p of the system as

$$U_p = max \left[\frac{EA}{2} \int_0^{2\pi/k_r} \left[\mathrm{Re}(U'(x,\omega)e^{j\omega t}) \right]^2 dx \right.$$
$$\left. + \quad \frac{b}{2} \int_0^{h_f} \int_0^{2\pi/k_r} \sum \left[\mathrm{Re}(\sigma(x,y,\omega)e^{j\omega t}) \mathrm{Re}(\epsilon(x,y,\omega)e^{j\omega t}) \right] dx\, dy \right] \quad (5.18)$$

where the first and second terms denote the respective strain energies stored in the bar and foam over a wavelength of the bar and the summation in the second term is taken over all the components of stress and strain in the foam. Substituting for U from (5.6) and carrying out the summation in the second term, we obtain the following simpler form for U_p:

$$U_p = 2\pi EAk_r U_+ U_-$$
$$+\tfrac{b}{2} \int_0^{h_f} \int_0^{2\pi/k_r} \left[\mathrm{Re}(\sigma_x)\mathrm{Re}(\epsilon_x) + \mathrm{Re}(\sigma_y)\mathrm{Re}(\epsilon_y) + \mathrm{Re}(\tau_{xy})\mathrm{Re}(\gamma_{xy}) \right] dx\, dy \quad (5.19)$$

Substituting the above expression for the peak potential energy U_p and that of W given in (5.17) into (5.1), we obtain the loss factor η for the bar-foam systems. Finally, we plot this loss factor as a function of frequency in Figure 5.2 and compare it with the ones obtained from measurements and the modal expansion model presented in Chapter 4. We find from Figure 5.2 that the loss-factor predictions from the infinite-bar model follow the same trend as those of the full modal-expansion model and measured results and exhibit a broad band behavior. But the simplified model significantly underestimates the damping. In order to get a better agreement with measurements the material properties need to be measured to 10 kHz.

5.2.2 Complex-Wave-Number Approach

In Section 5.2.1, we found that the dynamic interaction between the bar and foam results in energy dissipation. Therefore, a longitudinal wave traveling in the bar decays in the direction of propagation and its wave number becomes complex. Hence we can use the definition given in (5.4) to compute the loss factor of the bar-foam system. We start by writing out the displacement U of

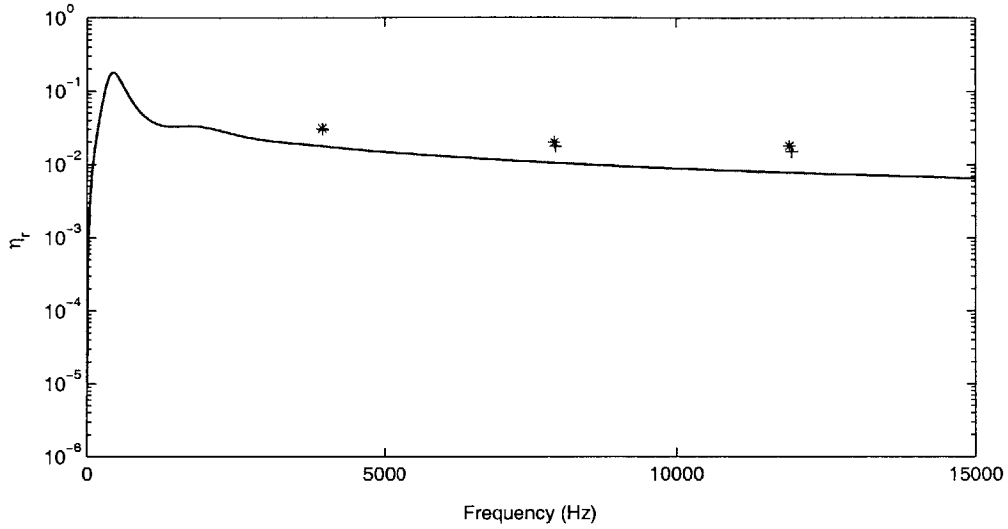

Figure 5.2: Comparison of loss factors for the bar-foam system: measurements (star signs) and full-modal-expansion model (plus signs) for the bar-foam system of Section 4.2 and infinite-bar model using energy approach (solid)

the damped bar in terms of the summation of forward and backward traveling waves as

$$U(x,\omega) = U_+(\omega)e^{-j\tilde{k}_r x} + U_-(\omega)e^{j\tilde{k}_r x} \tag{5.20}$$

where $\tilde{k}_r$ is the complex wave number associated with the longitudinal wave propagation in the damped bar. Next, we substitute the above expression for U and the estimate for the shear stress $\tau_{xy}(x,0,\omega)$ at the interface of the bar and foam given in (5.15) into the equation of motion for the bar (4.3) to obtain the following dispersion relation for the bar-foam system:

$$-EA\tilde{k}_r^2 + m\omega^2 + PG(\phi'(0,\omega) - k_r\psi(0,\omega)) = 0 \tag{5.21}$$

We then use (5.4) and write the following expression for the loss factor η_r of the bar-foam system

$$\eta = \frac{\mathrm{Im}(P\bar{G}\bar{\phi}'(0,\omega))}{m\omega^2 + \mathrm{Re}(P\bar{G}\bar{\phi}'(0,\omega))} \tag{5.22}$$

where we have dropped $\psi(0,\omega)$ because the displacement v vanishes at the interface of the bar and foam. Finally, we plot in Figure 5.3 the loss factor η_r

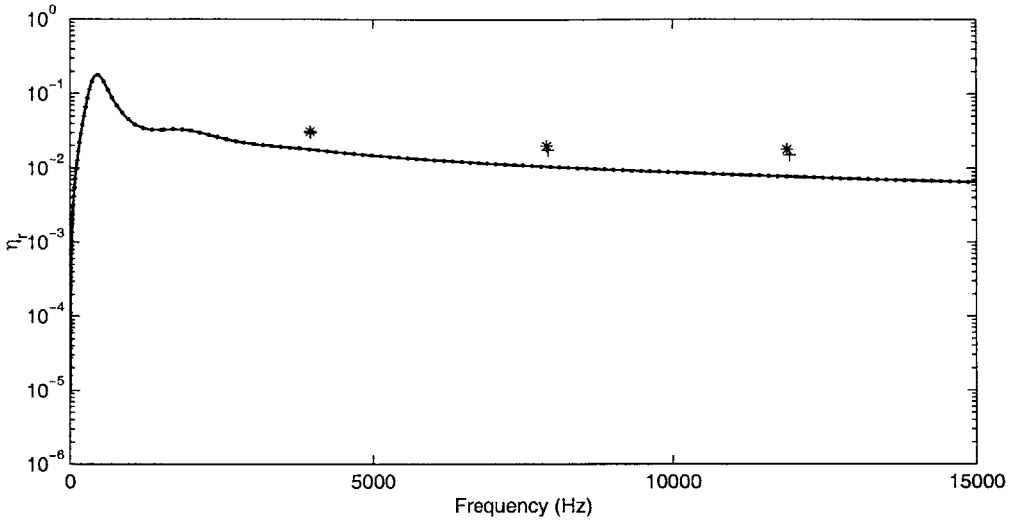

Figure 5.3: Comparison of loss factors for the bar-foam system: measurements (star signs) and full-modal-expansion model (plus signs) for the bar-foam system of Section 4.2 and infinite-bar model using complex-wave-number approach (solid) and energy approach (dotted)

obtained from the above equation and compare it to the ones obtained from the energy method, measurements, and full modal expansion model of Chapter 4. We find that the loss factor predictions from the energy and complex-wave-number approach are very close and exhibit a broadband behavior. We also notice that results from the measurements and the full model exhibit only qualitative agreement simplified approaches. In order to get a better agreement with measurements the material properties need to be measured to 10 kHz. The simplicity of the complex-wave-number approach over the energy approach makes it a better candidate for design.

5.3 Scaling for Bar-Foam Systems

In this section, we characterize the loss factor η_r in terms of certain non-dimensional parameters of the bar-foam system. Because the wavelength in the bar is an important characteristic length in the longitudinal direction, we scale the x coordinate by the wave number k_r of the undamped beam. This produces

the non-dimensional length-wise coordinate $\hat{x} = xk_r$. Similarly, we scale the transverse coordinate y using the wave number $k_f = \omega\sqrt{\rho/\mathrm{Re}(\lambda + 2G)}$ in the foam to obtain the non-dimensional coordinate $\hat{y} = yk_f$. Next, we rewrite the wave equations (5.10) and (5.11) in terms of the scaled coordinates as:

$$\phi'' = \left(\frac{\hat{k}_r}{1-2\nu}\right)\psi' + \frac{2(1-\nu)}{1-2\nu}\left(\hat{k}_r^2 - \frac{1}{1+j\eta_f}\right)\phi \tag{5.23}$$

$$\psi'' = -\left(\frac{\hat{k}_r}{2(1-\nu)}\right)\phi' + \left(\frac{\hat{k}_r^2(1-2\nu)}{2(1-\nu)} - \frac{1}{1+j\eta_f}\right)\psi \tag{5.24}$$

where the prime indicates derivative with respect to $\hat{y}$ and we have assumed the loss factor in dilatation and shear to be equal to η_f. Further, it is interesting to note that the eigenvalues and eigenvectors of the above set of equations are independent of the frequency and depend only on the Poisson ratio ν, loss factor η_f of the foam, and the ratio of the speeds of sound $\hat{k}_r$ in the foam to that in the bar. We then solve the above equations subject to the boundary conditions (4.4) and (4.7) to obtain solutions for ϕ and ψ.

5.3.1 Energy Approach

As described in Section 5.2.1, we use the solutions for ϕ and ψ to compute the stresses and strains in the foam and substitute them into (5.17) to obtain the energy dissipated W per a period of harmonic cycle. Because the peak potential energy in the bar is significantly larger than that in the foam, we neglect the second term in (5.19) to simplify the expression for the loss factor η_r which takes the following form:

$$\frac{\eta_r}{m_r} = \frac{1}{\hat{h}_f}\mathrm{Im}\left[\int_0^{\hat{h}_f}(1+j\eta_f)\left[\hat{k}_r^2|\phi|^2 + |\psi'|^2 + \frac{2\nu\hat{k}_r}{1-\nu}\mathrm{Re}(\bar{\phi}\psi') + \frac{1-2\nu}{2(1-\nu)}\left(|\phi'|^2 + \hat{k}_r^2|\psi|^2 - 2\hat{k}_r\mathrm{Re}(\phi'\bar{\psi})\right)\right]d\hat{y}\right] \tag{5.25}$$

where m_r is the ratio of the mass of the foam to that of the bar and $\hat{h}_f = k_f h_f$ is the non-dimensional wave number in the foam. In the above expression the sums of the first and last three terms are respectively, the contributions to the loss factor from dilatation and shear.

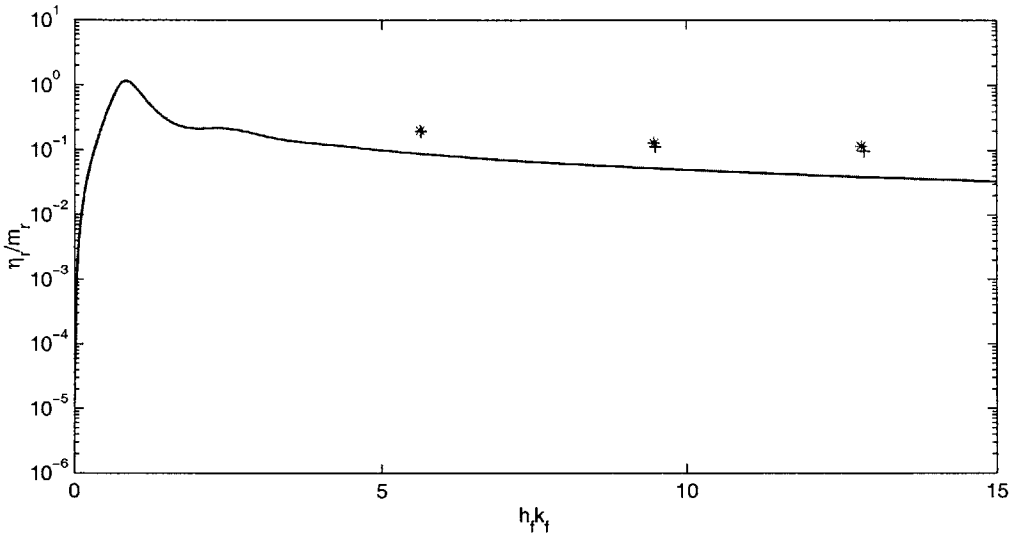

Figure 5.4: η_r/m_r versus non-dimensional foam thickness $\hat{h}_f$: infinite-bar model using energy approach (solid), full-modal-expansion model (plus signs), and measurements (star signs)

5.3.2 Complex-Wave-Number Approach

By scaling the derivative of $\bar{\phi}$ appropriately and neglecting the second term in the denominator of (5.22) in comparison with the first (inertia term of the bar), we obtain the following simple expression for the loss factor of the bar-foam systems via the complex-wave-number approach outlined in Section 5.2.2

$$\frac{\eta_r}{m_r} = \frac{(1-2\nu)}{2(1-\nu)\hat{h}_f} \mathrm{Im}\left[(1-j\eta_f)\bar{\phi}'(0,\hat{h}_f)\right] \tag{5.26}$$

Next, we plot the ratio η_r/m_r given in the above expression against $\hat{h}_f$ in Figure 5.5 and compare it with that of energy approach shown in 5.4. We find that the results from both the approaches are very close and compare well with the measurements and modal expansion model. Next, we note that η_r/m_r is significant whenever $\hat{h}_f$ is roughly more than unity; thus confirming that the damping arises from a strong coupling between the bar and foam via the establishment of standing waves in foam. Finally, we observe from (5.25) and (5.26) that the expression for loss factor obtained via the complex-wave-number approach is much simpler than the one from the energy approach.

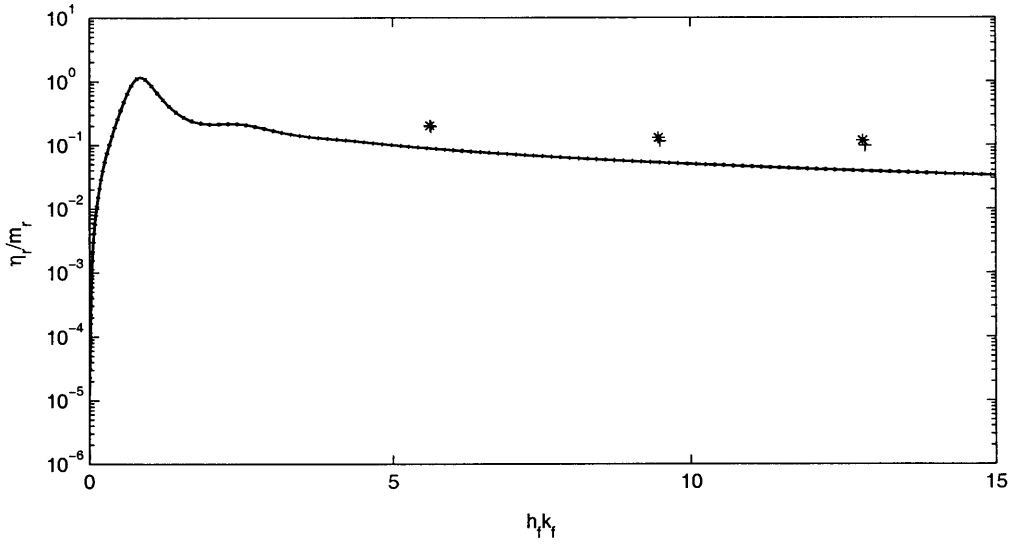

Figure 5.5: η_r/m_r versus non-dimensional wave number $\hat{h}_f$: infinite-bar model using complex-wave-number approach (dotted) and energy approach (solid), full-modal-expansion model (plus signs), and measurements (star signs)

5.3.3 Parametric Studies on the Loss Factor

In this section, we study the effect of the several parameters such as

- m_r: ratio of mass of foam to that of bar
- η_f: loss factor of foam
- ν: Poisson ratio of foam
- $\hat{k}_r$: ratio of the wave numbers (or alternately ratio of the speeds of sound)
- $\hat{h}_f$: non-dimensional wave number

on the loss factor η_r of the bar-foam system. From (5.25) and (5.26), we find that the loss factor η_r is directly proportional to the mass ratio m_r whereas the dependence on the other parameters is not as straight forward. Hence, we produce certain trend plots as shown in Figures 5.6–5.8 using (5.26) (because of its simplicity over (5.25)) to study the effect of the other parameters over the ratio η_r/m_r.

In Figure 5.6, we plot the ratio η_r/m_r against $\hat{h}_f$ for several values of η_f while keeping the other parameters constant. We find that as the loss factor of the foam increases the ratio η_r/m_r becomes more broadband whereas its maximum value decreases. Next we increase the Poisson ratio ν while keeping other parameters constant and find in Figure 5.7 that the maximum of η_r/m_r moves to the left. This can be readily explained by the increase in the speed of shear waves in foam. Finally, from Figure 5.8, we observe that η_r/m_r is weakly dependent on the ratio of wave numbers $\hat{k}_r$ (or equivalently, ratio of speeds of sound). However, it is important that the speed of sound in the foam be low in order to lower the cut-off frequencies above which the damping is significant.

5.4 Simplified Model for Beam-Foam Systems

In this section, we derive expressions for the loss factor of the beam-foam systems using the energy and complex-wave-number approaches. The analysis presented in this section closely parallels that of the the bar-foam systems. Consider beam-foam systems of infinite length extending from $x = -\infty$ to $x = +\infty$ (as shown in Figure 5.9) and undergoing steady harmonic motion

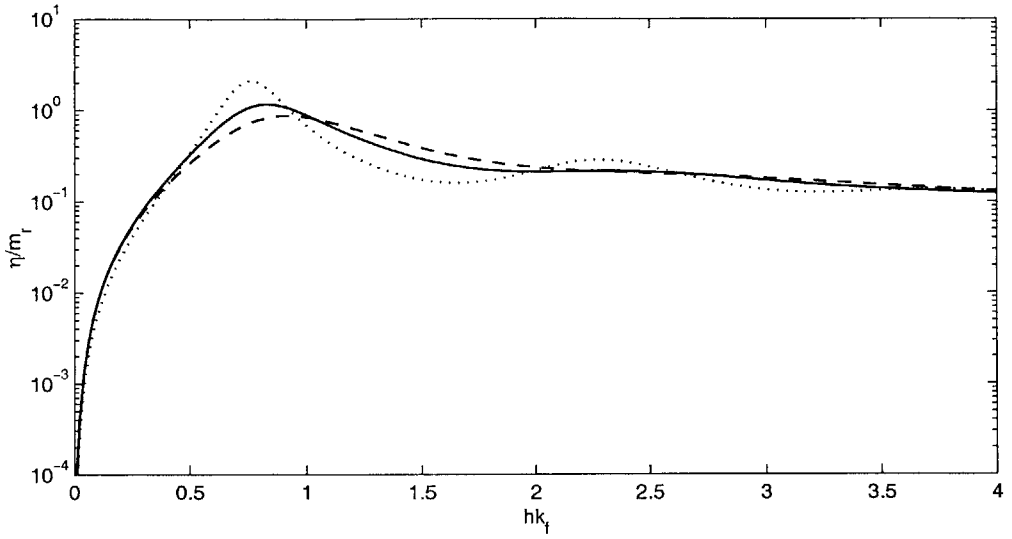

Figure 5.6: η/m_r versus $\hat{h_f}$ for $\hat{k}_r = 0.0063$, $\nu = 0.36$, and various values of η_f: 0.4 (dotted), 0.8 (solid), and 1.2 (dashed)

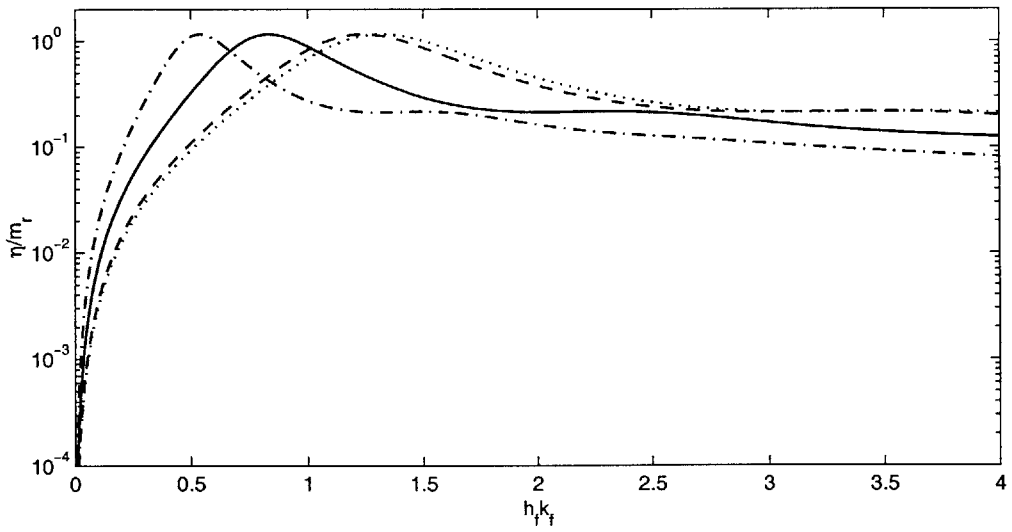

Figure 5.7: η/m_r versus $\hat{h_f}$ for $\hat{c} = 0.0063$, $\eta_f = 0.8$, and various values of ν: -0.1 (dotted), 0.036 (solid), 0.36 (dashed), and 0.45 (dash-dot)

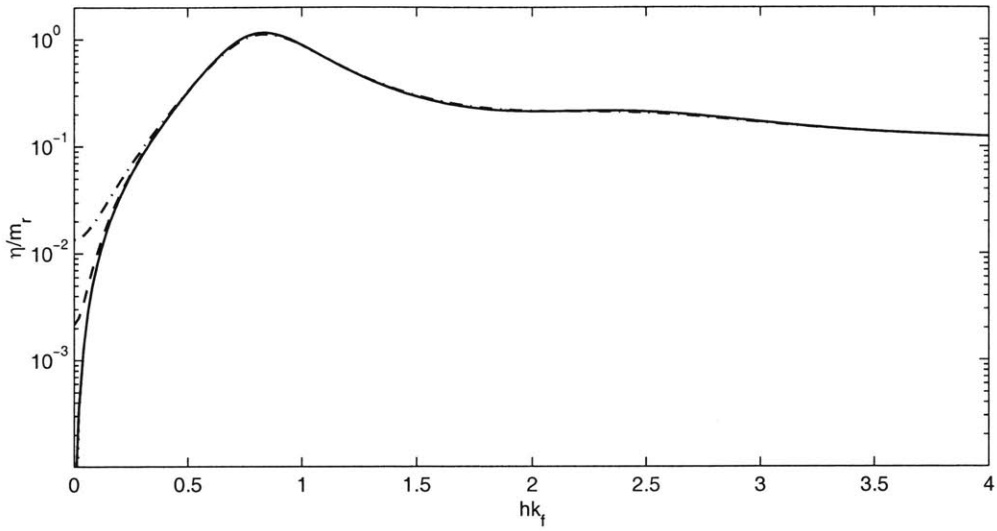

Figure 5.8: η/m_r versus $\hat{h_f}$ for $\eta_f = 0.8$, $\nu = 0.36$, and various values of $\hat{c}$: 0.00063 (dotted), 0.0063 (solid), 0.063 (dashed), and 0.16

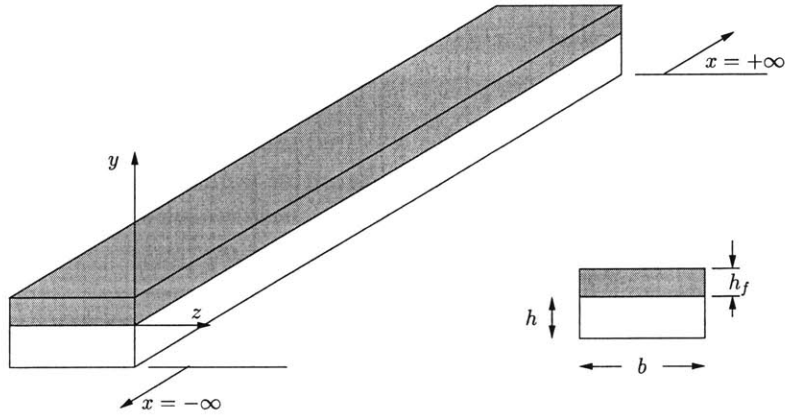

Figure 5.9: Schematic of the infinite beam-foam system

at a frequency ω in the y direction. As described in Chapter 3, we denote the vibratory deflection of the beam by $\mathrm{Re}(V(x,\omega)e^{j\omega t})$ and the displacements in the foam in the x and y directions by $\mathrm{Re}(u(x,\omega)e^{j\omega t})$ and $\mathrm{Re}(v(x,\omega)e^{j\omega t})$, respectively. To obtain estimates for damping, we need to solve the coupled wave equations (3.1) and (3.2) subject to the boundary conditions (3.4)–(3.7). As in the case of bar-foam systems of Section 5.2, closed-form solutions are difficult to obtain and therefore we seek approximate solutions. To this end, we write the deflection V of the beam in terms of the solutions of an undamped beam of infinite length as

$$V(x,\omega) = V_+(\omega)e^{-jk_b x} + V_-(\omega)e^{jk_b x} \tag{5.27}$$

where the first and second terms represent forward and backward traveling flexural waves in the beam and k_b is the associated wave number. It is given by the following familiar dispersion relation of the beam:

$$k_b^4 = \frac{\omega^2 m}{EI} \tag{5.28}$$

where m is the mass per unit length and EI is the flexural stiffness of the beam. Next we write compatible displacements in the foam as

$$v(x,y,\omega) = (V_+(\omega)e^{-jkx} + V_-(\omega)e^{jkx})\psi(y) \tag{5.29}$$

$$u(x,y,\omega) = -j(V_+(\omega)e^{-jkx} - V_-(\omega)e^{jkx})\phi(y) \tag{5.30}$$

where $\psi(y)$ and $\phi(y)$ are yet to be determined functions. Substituting the above expressions for u and v in the wave equations (3.1) and (3.2), we obtain the following second-order ordinary differential equations for ψ and ϕ:

$$\psi'' = k_b\left(\frac{\lambda+G}{\lambda+2G}\right)\phi' + \left(\frac{Gk_b^2 - \rho\omega^2}{\lambda+2G}\right)\psi \tag{5.31}$$

$$\phi'' = -k_b\left(\frac{\lambda+G}{G}\right)\psi' + \left(\frac{(\lambda+2G)k_b^2 - \rho\omega^2}{G}\right)\phi \tag{5.32}$$

where prime denotes the first derivative. Next we solve the above equations subject to (3.4)–(3.7) and obtain the functions $\psi(y)$ and $\phi(y)$. We then use these solutions along with the definitions for stress and strain of a two-dimensional continuum (e.g., Timoshenko and Goodier [49]; (5.12)) to obtain

the following expressions for the components of stress and strain in the foam:

$$\sigma_x = [-k(\lambda+2G)\phi + \lambda\psi']\,V \quad ; \quad \epsilon_x = -k\phi V \tag{5.33}$$

$$\sigma_y = [-k\lambda\phi + (\lambda+2G)\psi']\,V \quad ; \quad \epsilon_y = \psi' V \tag{5.34}$$

$$\tau_{xy} = G\,[\phi' + k\psi]\,V'/k \quad ; \quad \gamma_{xy} = [\phi' + k\psi]\,V'/k \tag{5.35}$$

5.4.1 Energy Approach

As in the case of the bar-foam system of Section 5.2, the beam-foam system is of infinite extent and the associated motion is periodic in x. Therefore, we compute the loss factor η_b by evaluating the energy dissipation W and peak potential energy U over a wavelength of the beam. Using (5.3), we write the energy dissipated W per harmonic cycle for the beam-foam systems as

$$W = \pi b\,\mathrm{Im}\left[\int_0^{h_f}\int_0^{2\pi/k} (\sigma_x\bar{\epsilon}_x + \sigma_y\bar{\epsilon}_y + \tau_{xy}\bar{\gamma}_{xy})\;dx\,dy\right] \tag{5.36}$$

Substituting the expressions for stresses and strains from (5.33)–(5.35) into the above equation (5.36), we obtain the following expression for the energy dissipated W over a wavelength of the beam and per cycle of harmonic motion:

$$\begin{aligned} W \;=\; & \left(4\pi^2 b V_+ V_-/k\right)\,\mathrm{Im}\left[\int_0^{h_f}\left[(\lambda+2G)(k^2|\phi|^2 + |\psi'|^2) - 2\lambda k\mathrm{Re}(\bar{\phi}\psi')\right.\right. \\ & \left.\left. +G(|\phi'|^2 + k^2|\psi|^2 + 2k\mathrm{Re}(\phi'\bar{\psi}))\right]\;dy\right] \end{aligned} \tag{5.37}$$

Next, we evaluate the peak potential energy U_p of the beam-foam system in a harmonic cycle over a wavelength of the beam as a sum of the peak strain energy in the beam and that in the foam. The former can be obtained from the familiar expressions for the strain energy in a beam (e.g., Crandall [11]) and the later from those of an isotropic continuum (e.g., Timoshenko and Goodier [49]). Using these expressions, we write the peak potential energy U_p of the system as

$$\begin{aligned} U_p = \;& max\left[\frac{EI}{2}\int_0^{2\pi/k}\left[\mathrm{Re}(V''(x,\omega)e^{j\omega t})\right]^2\,dx\right. \\ + \;& \left.\frac{b}{2}\int_0^{h_f}\int_0^{2\pi/k}\sum\left[\mathrm{Re}(\sigma(x,y,\omega)e^{j\omega t})\mathrm{Re}(\epsilon(x,y,\omega)e^{j\omega t})\right]\,dx\,dy\right] \end{aligned} \tag{5.38}$$

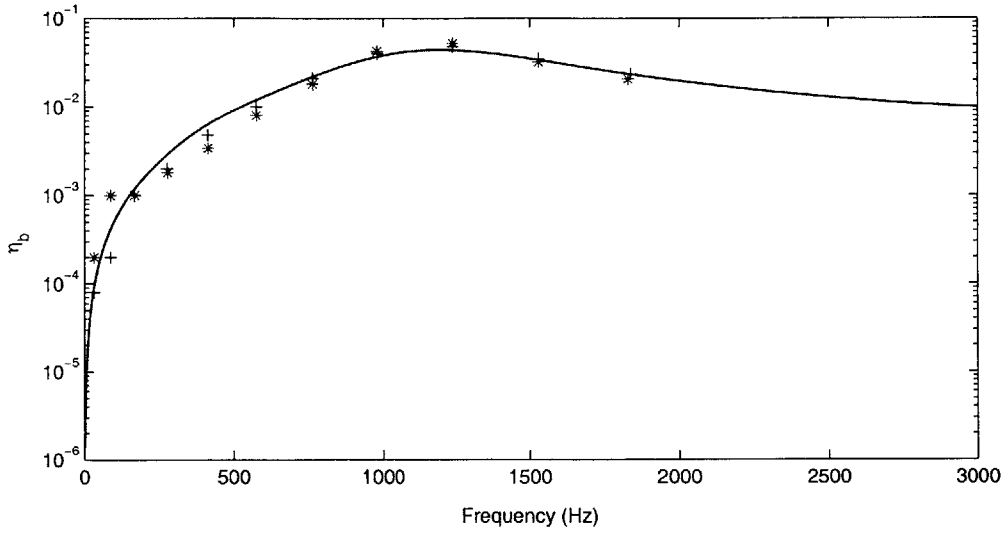

Figure 5.10: Comparison of loss factors for the beam-foam system: measurements (star signs) and full-modal-expansion model (plus signs) for the beam described in Chapter 3 (aluminum beam of length 1448 mm) and infinite-beam model using energy approach (solid)

where the first and second terms denote the respective strain energies stored in the beam and foam over a wavelength of the beam and the summation in the second term is taken over all the components of stress and strain in the foam. Substituting for V from (5.27) and carrying out the summation in the second term, we obtain the following simpler form for U_p:

$$U_p = 2\pi EIk^3 V_+ V_- \\ + \frac{b}{2} \int_0^{h_f} \int_0^{2\pi/k} [\mathrm{Re}(\sigma_x)\mathrm{Re}(\epsilon_x) + \mathrm{Re}(\sigma_y)\mathrm{Re}(\epsilon_y) + \mathrm{Re}(\tau_{xy})\mathrm{Re}(\gamma_{xy})]\, dx\, dy \quad (5.39)$$

Substituting the above expression for the peak potential energy U_p and that for W given by (5.37) into (5.1), we obtain the loss factor η_b for beam-foam systems. Finally, we plot this loss factor as a function of frequency in Figure 5.10 and compare it with those obtained from measurements and the modal expansion model presented in Chapter 3. We find from Figure 5.10 that the loss-factor predictions from the infinite-beam model are in good agreement with the previous results and exhibits a broadband behavior.

5.4.2 Complex-Wave-Number Approach

As in the case of the bar-foam systems, the dynamic interaction between the foam and beam results in the decay of flexural waves traveling in the beam and causes the associated wave numbers to become complex. Hence we can use the definition given in (5.5) to compute the loss factor of the beam-foam system. We start by writing out the deflection V of the damped beam in terms of the summation of forward and backward traveling waves as

$$V(x,\omega) = V_+(\omega)e^{-j\tilde{k}_b x} + V_-(\omega)e^{j\tilde{k}_b x} \tag{5.40}$$

where $\tilde{k}_b$ is the complex wave number associated with the flexural wave propagation in the damped beam. Next, we substitute the above expression for V and the estimate for the normal stress $\sigma_y(x,0,\omega)$ and shear stress $\tau_{xy}(x,0,\omega)$ at the beam-foam interface given in (5.34) and (5.35) into the equation of motion for the beam (3.3) to obtain the following dispersion relation for the beam-foam system:

$$EI\tilde{k}_b^4 - m\omega^2 - b\left[-\lambda k_b\phi(0) + (\lambda+2G)\psi'(0) - \frac{Ghk_b}{2}(\phi'(0) + k_b\psi(0))\right] = 0 \tag{5.41}$$

We then use (5.5) and write the following expression for the loss factor η_b of the beam-foam system

$$\eta_b = \frac{b\,\mathrm{Im}\left[(\bar{\lambda}-\bar{G})k_b^2h/2 + (\bar{\lambda}+2\bar{G})\bar{\psi}'(0) - \bar{G}\bar{\phi}'(0)k_bh/2\right]}{m\omega^2 + b\,\mathrm{Re}\left[(\bar{\lambda}-\bar{G})k_b^2h/2 + (\bar{\lambda}+2\bar{G})\bar{\psi}'(0) - \bar{G}\bar{\phi}'(0)k_bh/2\right]} \tag{5.42}$$

where we have used the boundary conditions on the foam displacements at the beam-foam interface to determine $\phi(0)$ and $\psi(0)$. Finally, we plot in Figure 5.11 the loss factor η_b obtained from the above equation and compare it to the ones obtained from the energy method, measurements, and full modal expansion model of Chapter 3. As in the case of the bar-foam systems, we find that the loss factor predictions from the energy and complex-wave-number approach are very close and exhibit a broadband behavior. We also notice that results from the measurements and the full model are in agreement with the simplified approaches.

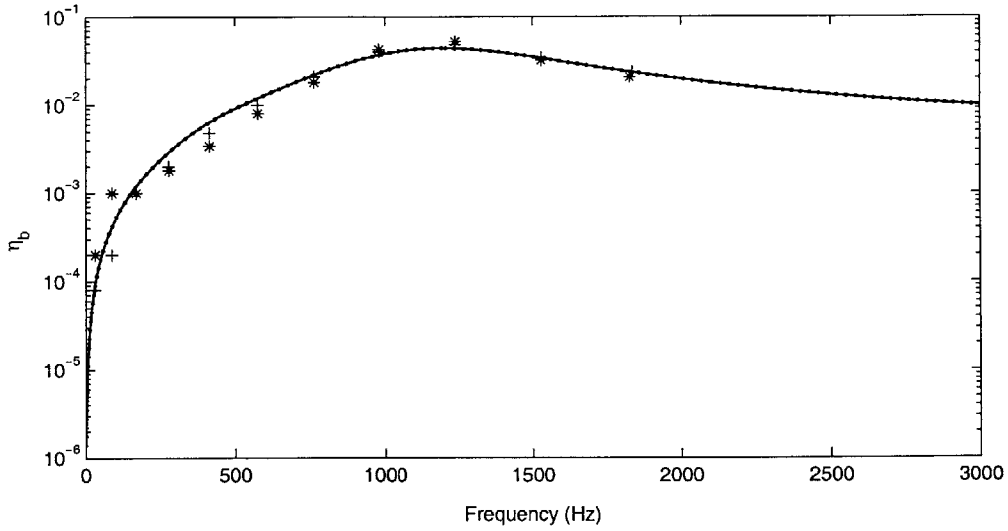

Figure 5.11: Comparison of loss factors for the beam-foam system: measurements (star signs) and full-modal-expansion model (plus signs) for the beam described in Chapter 3 (aluminum beam of length 1448 mm); infinite-beam model using complex-wave-number approach (solid) and energy approach (dotted)

5.5 Scaling Laws for Beam-Foam Systems

In this section, we obtain a non-dimensional form for the loss factor η_b of the beam-foam system in a manner similar to that of the bar-foam system. We start by scaling the x coordinate using the wave number k_b of the undamped beam because the wavelength of the beam is an important characteristic dimension in the length-wise direction. This produces the non-dimensional coordinate $\hat{x} = xk_b$. As in the foam-bar system, we scale the transverse coordinate y using the wave number k_f in the foam to obtain the non-dimensional coordinate $\hat{y} = yk_f$. Next, we rewrite the wave equations (5.32) and (5.31) in terms of the scaled coordinates as:

$$\psi'' = \left(\frac{\hat{k}_b}{2(1-\nu)}\right)\phi' + \left(\frac{\hat{k}_b^2(1-2\nu)}{2(1-\nu)} - \frac{1}{1+j\eta_f}\right)\psi \tag{5.43}$$

$$\phi'' = -\left(\frac{\hat{k}_b}{1-2\nu}\right)\psi' + \frac{2(1-\nu)}{1-2\nu}\left(\hat{k}_b^2 - \frac{1}{1+j\eta_f}\right)\phi \tag{5.44}$$

where the prime indicates derivative with respect to $\hat{y}$ and we have assumed the loss factor in dilatation and shear to be equal to η_f. Note that unlike the case of the bar-foam systems the eigen properties of the above set of equations depend on the frequency because of the non-linear dispersion relation of the beam. We solve the above equations subject to the boundary conditions (3.4) and (3.7) to obtain solutions for ψ and ϕ.

5.5.1 Energy Approach

As described in Section 5.4.1, we use the solutions for ϕ and ψ to compute the stresses and strains in the foam and substitute them into (5.37) to obtain the energy dissipated W per period of harmonic motion. Because the peak potential energy in the beam is significantly larger than that in the foam, we neglect the second term in (5.39) to simplify the expression for the loss factor η_b, which takes the following form:

$$\frac{\eta_r}{m_r} = \frac{1}{\hat{h}_f}\mathrm{Im}\left[\int_0^{\hat{h}_f}(1+j\eta_f)\left[\hat{k}_b^2|\phi|^2 + |\psi'|^2 - \frac{2\nu\hat{k}_b}{1-\nu}\mathrm{Re}(\bar{\phi}\psi') + \frac{1-2\nu}{2(1-\nu)}\left(|\phi'|^2 + \hat{k}_b^2|\psi|^2 + 2\hat{k}_b\mathrm{Re}(\phi'\bar{\psi})\right)\right] d\hat{y}\right] \tag{5.45}$$

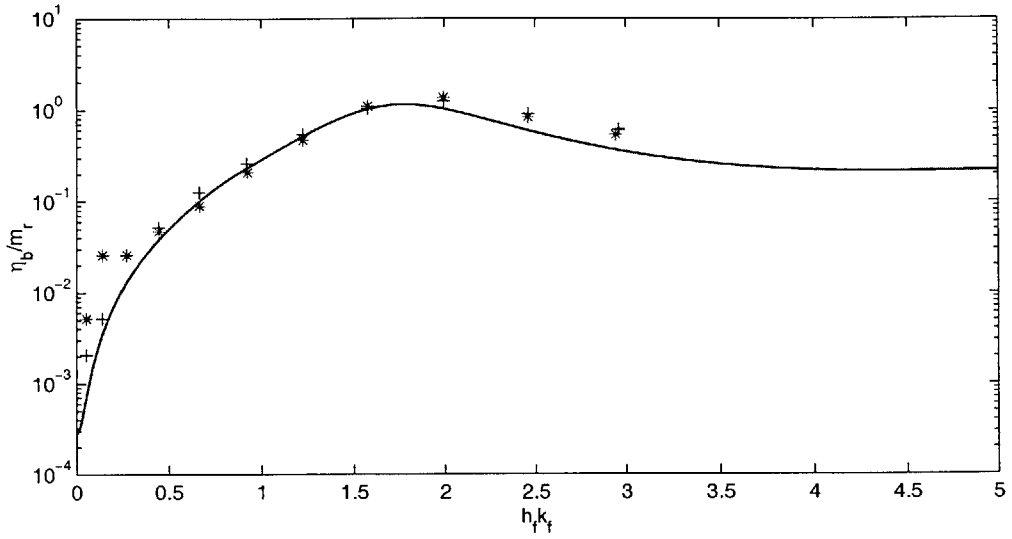

Figure 5.12: η_r/m_r versus non-dimensional foam thickness $\hat{h}_f$: infinite-beam model using energy approach (solid), full-modal-expansion model (plus signs), and measurements (star signs)

where $\hat{h}_f = k_f h_f$ is the non-dimensional wave number in foam. We note that the above expression has a similar form as the bar-foam system given in (5.25). However, as we shall see later the dependence of damping on the ratio of the wave numbers is more pronounced in beam-foam systems than in bar-foam systems.

5.5.2 Complex-Wave-Number Approach

By scaling the derivatives of $\bar{\phi}$ and $\bar{\psi}$ appropriately and neglecting the second term in the denominator of (5.42) in comparison with the first (inertia term of the beam), and using the complex-wave-number approach outlined in Section 5.4.2, we obtain the following simple expression for the loss factor of the beam-foam systems

$$\frac{\eta_r}{m_r} = \mathrm{Im}\left[(1 - j\eta_f)\left(\frac{\bar{\psi}'(0)}{\hat{h}_f} - \frac{(1-2\nu)}{4(1-\nu)}\hat{k}_b\hat{h}\bar{\phi}'(0) + \frac{4\nu - 1}{4(1-\nu)}\hat{k}_b^2\hat{h}\right)\right] \quad (5.46)$$

where $\hat{h} = h/h_f$ is the non-dimensional thickness of the beam. Because of the non-linear dispersion relation for the beam the parameter $\hat{k}_b$ is dependent on frequency unlike its counterpart $\hat{k}_r$ of the bar-foam system ($\hat{k}_r$ is essentially the ratio of the speeds of sound in the foam and bar). In order to understand the parametric dependence of η_r/m_r on the properties of the foam and beam, we find it convenient to introduce the following scaling for the wave-number ratio $\hat{k}_b$:

$$\hat{k}_b^2 \sim \frac{\hat{c}}{\hat{h}\hat{h}_f} \tag{5.47}$$

where $\hat{c}$ is the ratio of the speeds of sound in the foam and beam and is given by

$$\hat{c}^2 = \frac{\rho_b \mathrm{Re}(\lambda + 2G)}{\rho E} \tag{5.48}$$

where ρ_b is the density of the material of the beam. Next, we plot the ratio η_r/m_r given in (5.46) against $\hat{h}_f$ in Figure 5.13 and compare it with that obtained in 5.45 using the energy approach. We find that the results from both the approaches are very close and are in agreement with the measurements and modal expansion model. We note that η_r/m_r is significant whenever $\hat{h}_f$ is about unity or greater; thus confirming that the damping arises from a strong coupling between the beam and foam via the establishment of standing waves in foam. Finally, we observe from (5.45) and (5.46) that the expression for loss factor obtained via the complex-wave-number approach is much simpler than that obtained from the energy approach.

5.5.3 Parametric Studies on the Loss Factor

In this section, we study the effect of the several parameters such as the mass ratio m_r, loss factor η_f and Poisson ratio ν of the foam, ratio of speeds of sound $\hat{c}$, and the non-dimensional wave number $\hat{h}_f$ on the loss factor η_b of the beam-foam system. As in the bar-foam system, we find (from (5.45) and (5.46)) linear dependence of the loss factor η_b on the mass ratio m_r. Next, we find from Figure 5.14 that the influence of the loss factor η_f of the foam on η_b/m_r is similar to that of η_f on η_r/m_r (e.g., Figure 5.6): an increase in η_f reduces the peak of η_b/m_r while making it more broadband.

In Figure 5.15, we plot η_b/m_r against $\hat{h}_f$ for several values of the Poisson ratio ν. Unlike the bar-foam system, we find that the loss factor has a very weak dependence on the Poisson ratio ν. Finally, we observe from Figure 5.16

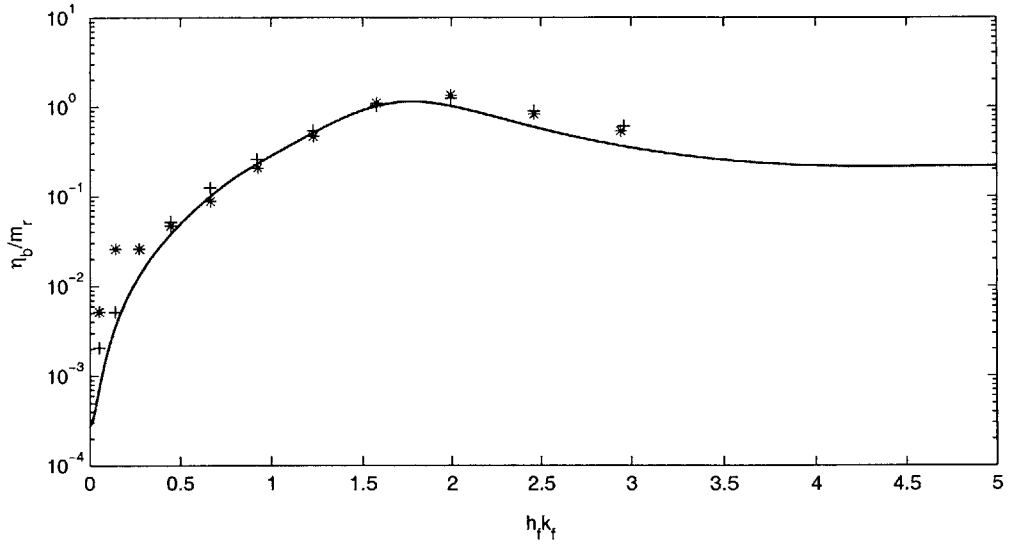

Figure 5.13: η_r/m_r versus non-dimensional wave number $\hat{h}_f$: infinite-beam model using complex-wave-number approach (dotted) and energy approach (solid), full modal expansion model (plus signs), and measurements (star signs)

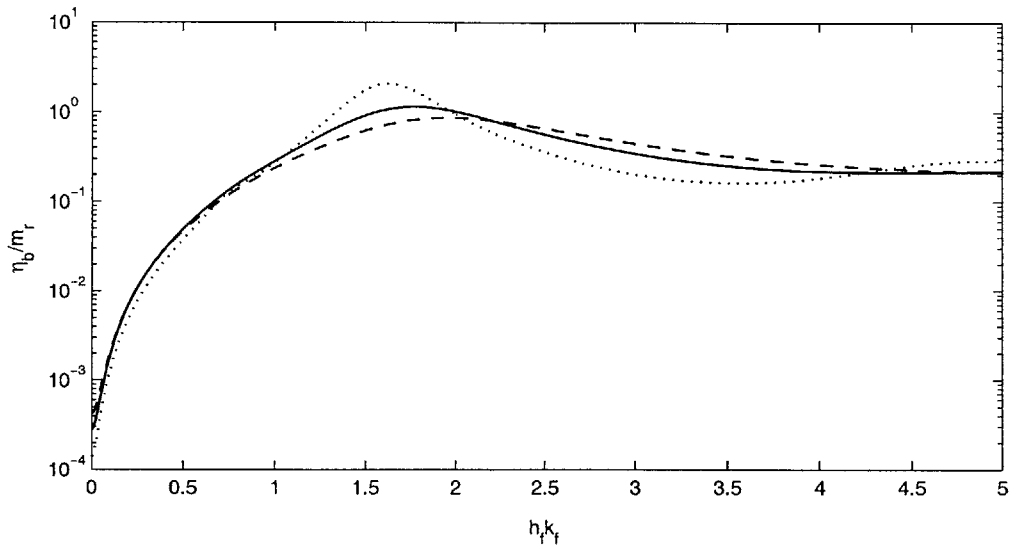

Figure 5.14: η_b/m_r versus $\hat{h_f}$ for $\hat{k_b} = 0.0063$, $\nu = 0.36$, and various values of η_f: 0.4 (dotted), 0.8 (solid), and 1.2 (dashed)

that η_b/m_r is weakly dependent on the ratio of the speeds of sound $\hat{c}$. However it is important that the speed of sound in the foam medium be low in order to lower the cut-off frequencies above which the damping is significant.

5.6 Chapter Summary

This chapter provides simplified analysis of the low-wave-speed damping phenomenon based on energy and complex-wave-number approaches. The analysis shows the damping is directly proportional to the mass ratio and is significant whenever the non-dimensional wave number $(h_f k_f)$ is greater than a "cut-off" value of about unity. Therefore the speed of sound in the medium must be low to achieve damping at lower frequencies.

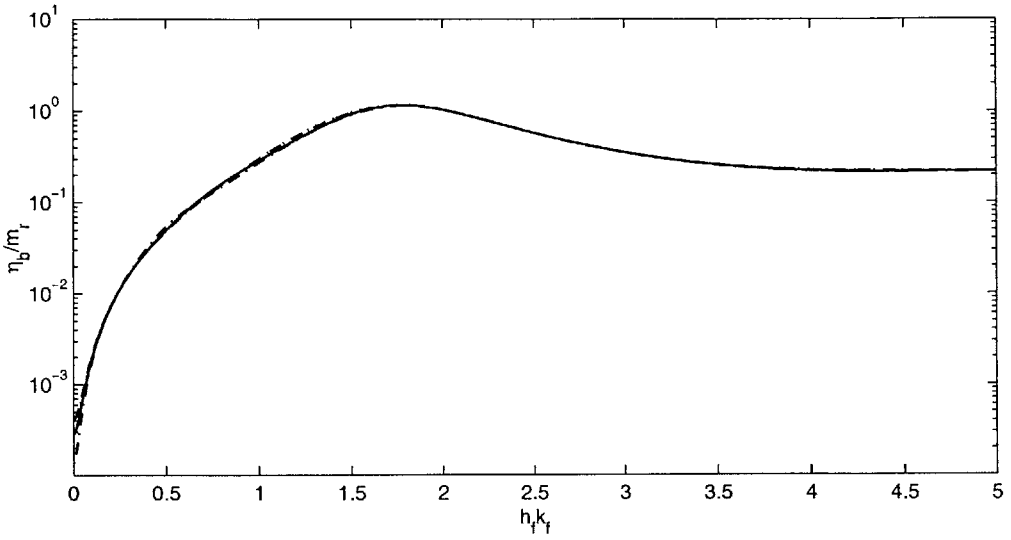

Figure 5.15: η_b/m_r versus $\hat{h_f}$ for $\hat{c} = 0.0063$, $\eta_f = 0.8$, and various values of ν: -0.1 (dotted), 0.036 (solid), 0.36 (dashed), and 0.45 (dash-dot)

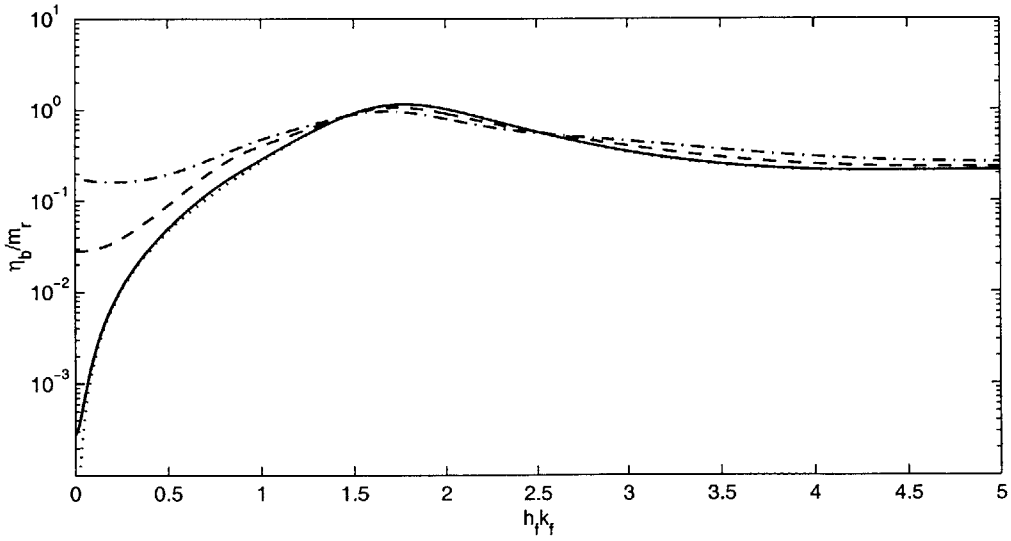

Figure 5.16: η/m_r versus $\hat{h_f}$ for $\eta_f = 0.8$, $\nu = 0.36$, and various values of $\hat{c}$: 0.00063 (dotted), 0.0.0063 (solid), 0.063 (dashed), and 0.16

CHAPTER 6

Enhancing the Dynamics of Belt-Driven Motion Systems using Low-Wave-Speed Media

6.1 Introduction

Flat steel belt drives are attractive for high-speed, high-acceleration, precision positioning systems because they can incorporate a drive reduction with low inertia and very smooth power transmission (e.g., Anon [5]). But because of belt "creep" or "microslip," (e.g., Johnson [23]) it is almost always necessary to employ a feedback sensor located on the "driven" or "output" component of the system. This makes the system susceptible to instabilities at high feedback gains. In particular, the longitudinal (axial) compliance of the belt gives rise to a resonance in which the driving and driven components of the system oscillate with different phases (e.g., Abrate [3]). This resonance imposes severe constraints on the closed-loop bandwidth. In this chapter, we show that by coupling a low-wave-speed medium (Varanasi and Nayfeh [54, 53]) to the belt, significant damping can be introduced into the axial and transverse modes, thereby substantially improving the closed-loop performance of the system.

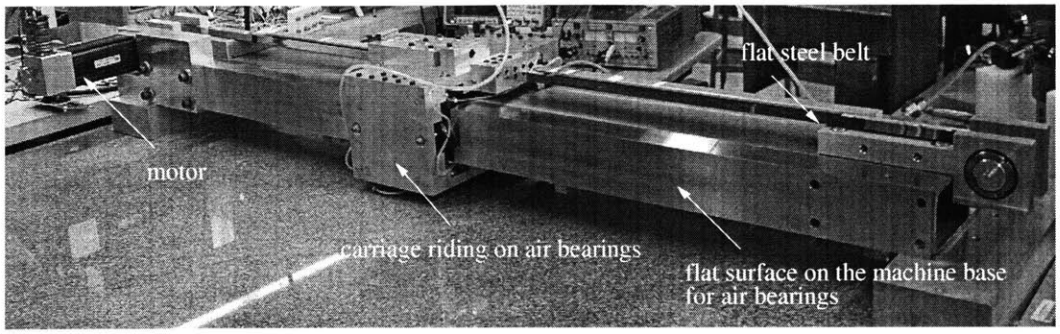

Figure 6.1: Photograph of the belt drive showing the machine base, carriage, motor, belt, and pulleys

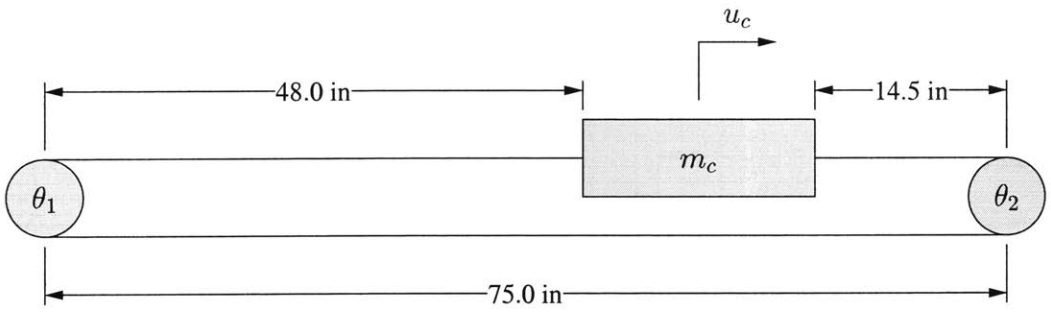

Figure 6.2: Schematic of the belt drive showing some length parameters used in measurements

6.2 Experiments

In this section, we describe measurements in which the damping of a belt drive is enhanced by coupling a layer of low-density low-wave-speed foam to the belt. The belt drive shown in Figure 6.1 moves a carriage weighing approximately 22.1 kg through a travel of 1270 mm. The carriage is mounted onto the stage via New Way porous graphite air bearings ([35]). The drive includes a spring-steel belt of thickness 0.10 mm and width 50.8 mm, the ends of which are clamped to the carriage. A brushless servomotor (Aerotech BM500 [4]) is attached to the shaft of the drive pulley by means of a bellows-type coupling (R+W BK2 [45]). The drive and idler pulleys are mounted onto the machine base via angular contact bearings. A Heidenhain LS403 linear encoder mea-

Table 6.1: Important parameters of the belt drive shown in Figure 6.1

Belt thickness	0.10 mm
Belt width	50.8 mm
Mass of Carriage	22.1 kg
Inertia of Motor	$13.9 \times 10^{-5}\,\mathrm{kgm}^2$
Inertia of Pulley	$1.2 \times 10^{-4}\,\mathrm{kgm}^2$
Radius r of the Pulleys	28.5 mm
Torsional stiffness of coupling	6800 Nm

sures the position of the carriage whereas the motor has an inbuilt rotary encoder to measure its rotation. The important details of the stage are given in Table 6.1 and Figure 6.2.

In Section 6.2.1, we detail sine-sweep experiments for the measurement of the transfer functions from the motor torque to motor and carriage positions. Next, in Section 6.2.2 we describe modal experiments conducted on the stage to determine the mode shape associated with the drive resonance. In all of these experiments the carriage is located near the end of its travel at a distance of 1219 mm from the axis of the drive pulley.

6.2.1 Transfer Functions

The transfer functions from the motor torque to motor and carriage positions are measured by exciting the motor with a sinusoidal torque and measuring the response from the motor encoder and linear encoder, respectively. A schematic of the experimental set-up is shown in Figure 6.3. The stage is set up under closed-loop control using a PC-based DSP board (dSPACE DS1103 [13]), and a disturbance signal is input to the system at a summing junction formed at the input terminal of the power amplifier of the motor. An HP35670A signal analyzer is used to generate a sinusoidal disturbance, measure the input and output signals, and determine their relative magnitude and phase.

In Figure 6.4, we plot the frequency response from motor torque to motor encoder with and without foam layers attached to the belt. In the absence of the foam layer, we find that the resonant mode arising from the compliance of the belt combined with the inertias of the carriage, pulleys, and the motor

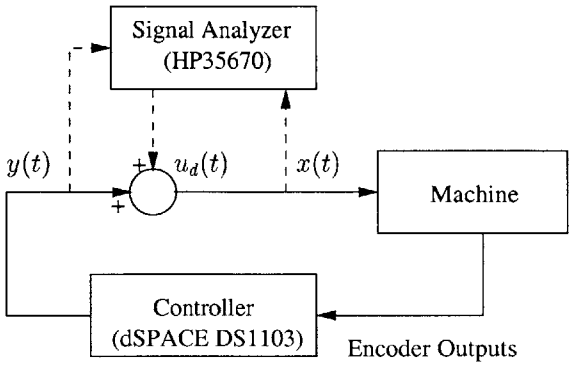

Figure 6.3: Schematic of sine-sweep experiments. The signals $x(t)$, $y(t)$, and $u_d(t)$ are the power amplifier input, DAC output, and swept sine disturbance, respectively. The required transfer function is $Y(s)/X(s)$.

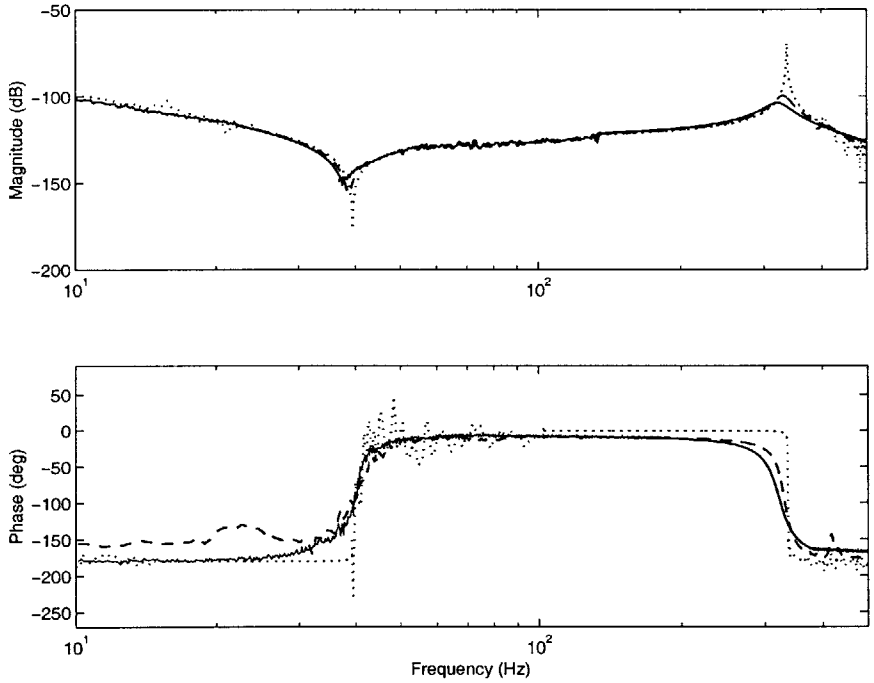

Figure 6.4: Measured frequency response from motor torque to motor position for the belt drive of Figure 6.1: without foam (dotted), with quarter-inch thick C3001 foam (dashed), and with half-inch thick C3201 foam (solid)

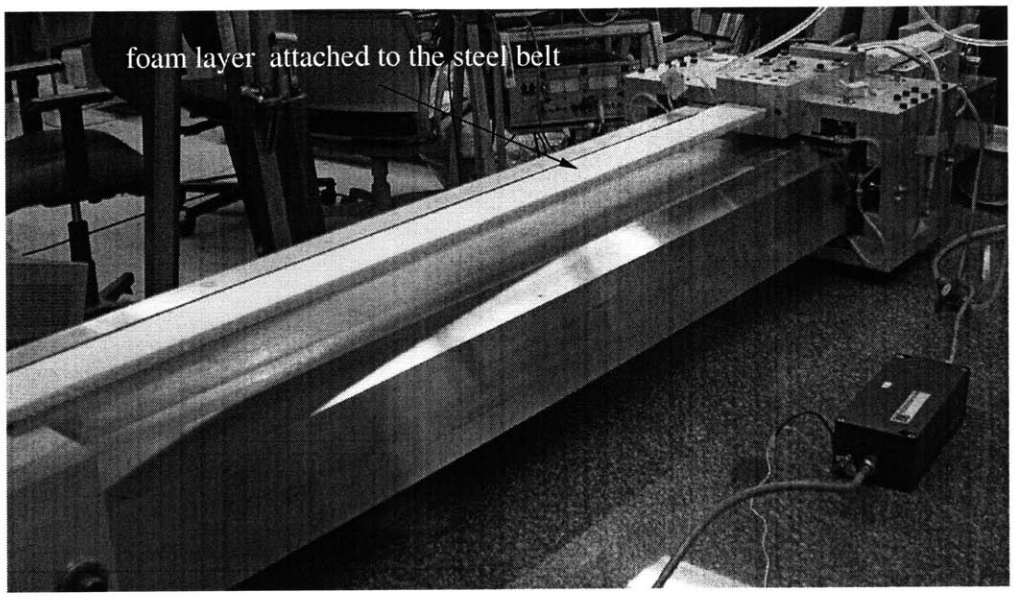

Figure 6.5: Photograph of the belt drive with 12.7 mm C3201 EAR [14] foam attached to the belt

exhibits little damping (damping ratio $\zeta = 0.001$). Likewise, we find the complex zeros arising from the compliance of the belt and the inertias of the carriage and the idler pulley are also lightly damped. But when layers of 12.7 mm EAR C3201 and 6.35 mm EAR C3001 [14] foams are each individually attached to the belt as shown in Figures 6.5 and 6.6, respectively, we observe significant damping in the resonant and zero modes. The damping ratios of the resonant mode are found to be 6.0% and 3.5% for the 12.7 mm C3201 and 6.35 mm C3001 foams, respectively.

Next, in Figure 6.7, we plot the frequency response from motor torque to linear encoder with and without foam layers. As in the case of the previous measurement, we find that addition of foam layers results in significant damping ($\zeta = 6.0\%$ and 3.5%) in the drive resonance. We also note that the next higher mode which corresponds to a yaw mode (Section 6.2.2) of the carriage is also damped.

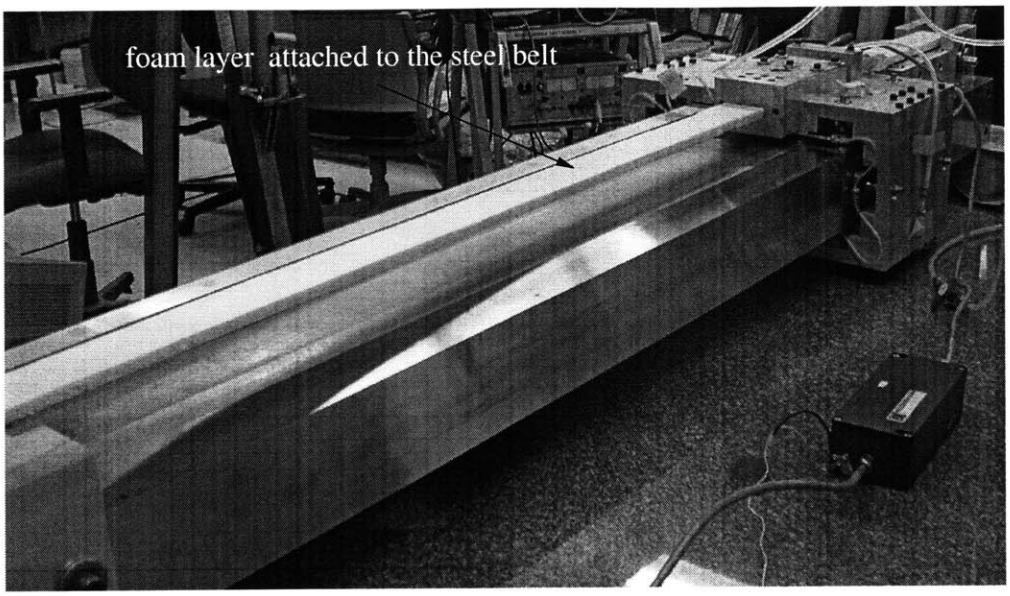

Figure 6.6: Photograph of the belt drive with 6.35 mm C3001 EAR [14] foam attached to the belt

6.2.2 Modal Tests

In Figure 6.8, we show the location of the excitation and measurement positions employed in modal tests of the machine. An impulsive excitation is imparted close to point 1 using an impact hammer (PCB333A30 [40]) and the response is measured using a three-axis accelerometer (PCB 356B08 [40]) at each of the other nineteen points shown in Figure 6.8. The points 2 through 13 are located on the carriage, 14 through 21 on the machine base. The impact hammer and the accelerometer are connected to a signal analyzer (HP35670A) to obtain the force-to-acceleration transfer functions. Next, we use standard modal-curve-fitting software such as Star Modal [46] to extract the values of resonant frequencies, damping ratios, and the associated mode shapes.

In Figure 6.9, we show (in plan view) a series of snapshots of the first flexible mode of the system starting from the undeformed position. From the figure, we see that this mode corresponds to the axial motion of the carriage accompanied by stretch of the belt. We also find that the measured resonant frequency and damping ratio closely match those obtained from the sine-sweep experiments. In Figure 6.10, we show snapshots of the yaw mode of the carriage which

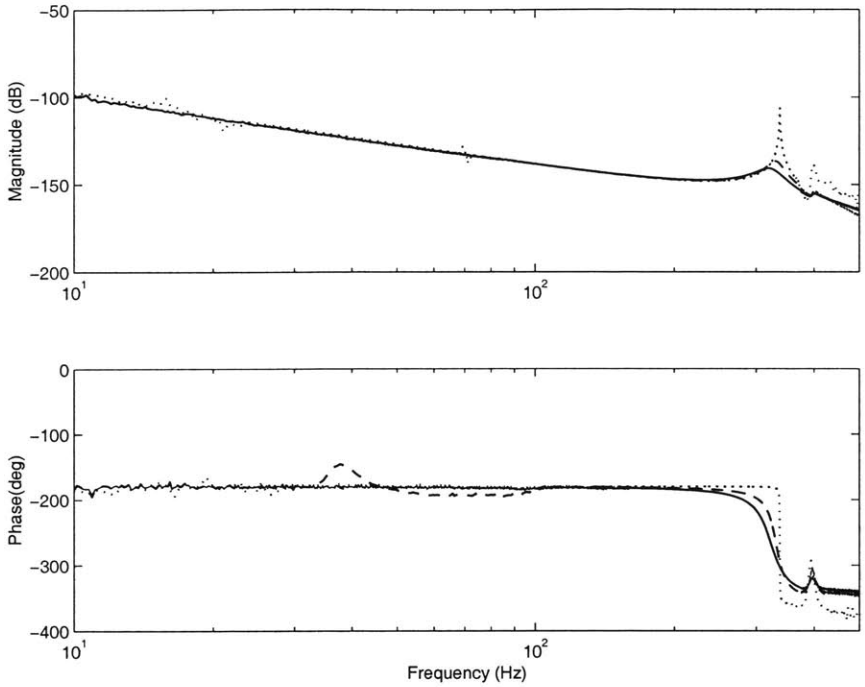

Figure 6.7: Measured frequency response from motor torque to carriage position for the belt drive of Figure 6.1: without foam (dotted), with quarter-inch thick C3001 foam (dashed), and with half-inch thick C3201 foam (solid)

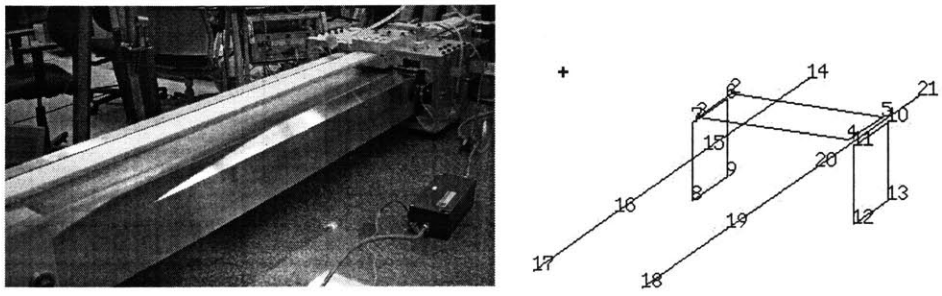

Figure 6.8: Drawing of the belt drive showing measurement positions for modal experiment

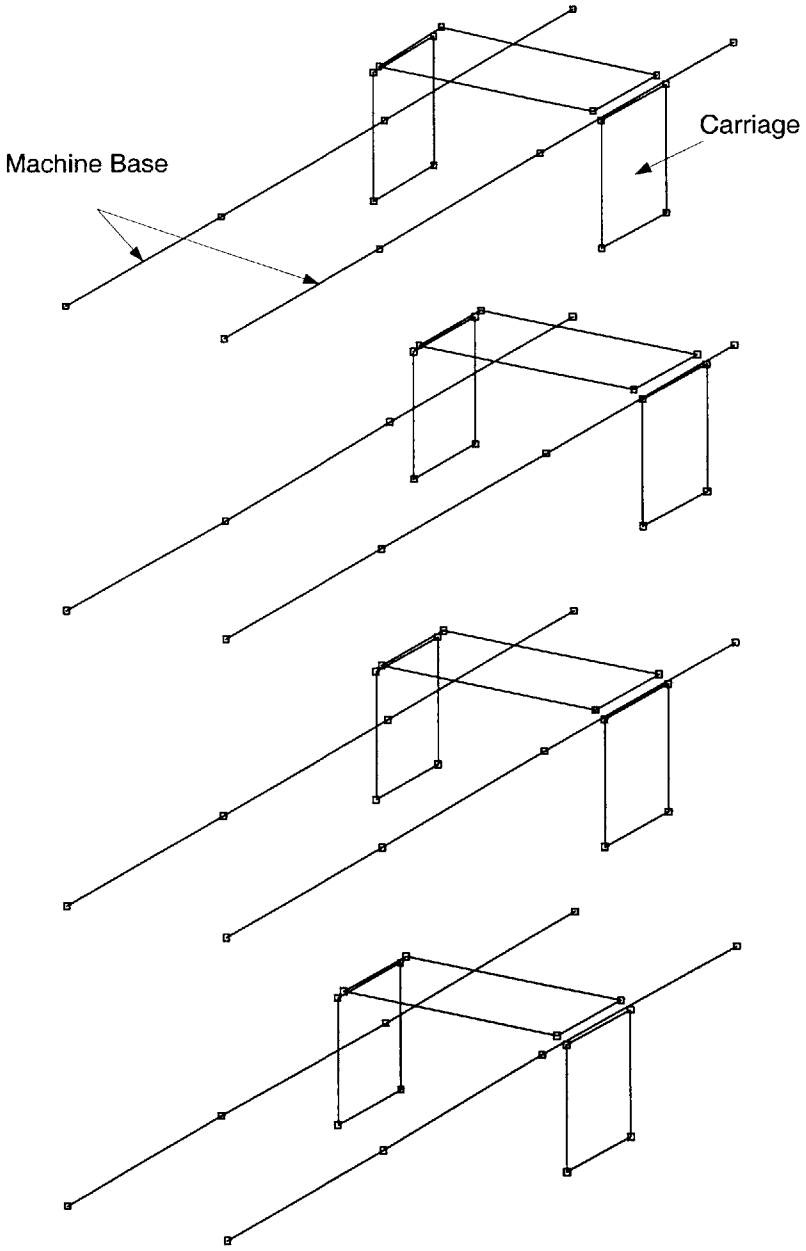

Figure 6.9: Measured axial mode shape of the belt drive at 337 Hz with damping ratio of 0.001. The figure shows snapshots of the mode starting from undeformed position. The small squares indicate measurement locations.

appears on the transfer function between motor torque and carriage position (Figure 6.7).

6.3 Model

In this section we derive a model for the belt drive from which the measured responses (Section 6.2) can be predicted. Consider steady harmonic vibration of the belt drive shown in Figure 6.1 at a frequency ω, where the vibratory displacement of the carriage is given by $\mathrm{Re}(u_c(\omega)e^{j\omega t})$ and the angle of rotation the motor is given by $\mathrm{Re}(\theta_m(\omega)e^{j\omega t})$. The complex variables $u_c(\omega)$ and $\theta_m(\omega)$ each represent the magnitude and the phase of motion as a function of the frequency ω. The longitudinal displacements on the top and bottom portions of the belt vary along the length of the belt and hence are written as $\mathrm{Re}(u_b(x,\omega)e^{j\omega t})$ and $\mathrm{Re}(\hat{u}_b(x,\omega)e^{j\omega t})$, respectively.

6.3.1 Distributed-Parameter Model

Belt

As described in Section 4.5, the longitudinal displacements of the belt $u_b(x,\omega)$ and $\hat{u}_b(x,\omega)$ are each governed by a second-order wave equation given by

$$EAu_b'' + m\omega^2 u_b + b\tau(x,\omega) = 0 \quad (6.1)$$

$$EA\hat{u}_b'' + m\omega^2 \hat{u}_b + b\hat{\tau}(x,\omega) = 0 \quad (6.2)$$

where E, A, m, and b are respectively, the Young's modulus, area of cross section, mass per unit length, and width of the belt, and $\tau(x,\omega)$ and $\hat{\tau}(x,\omega)$ are respectively the shear stresses at belt-foam interface on the top and bottom portions of the belt.

Foam

As described in earlier sections such as Section 4.3, we treat the foam as a lossy and isotropic continuum and write the wave equations governing the x-direction displacement u and transverse displacement v in the frequency domain as:

$$(\lambda + 2G)u_{xx} + Gu_{yy} + (\lambda + G)v_{xy} + \rho\omega^2 u = 0 \quad (6.3)$$

$$Gv_{xx} + (\lambda + 2G)v_{yy} + (\lambda + G)u_{xy} + \rho\omega^2 v = 0 \quad (6.4)$$

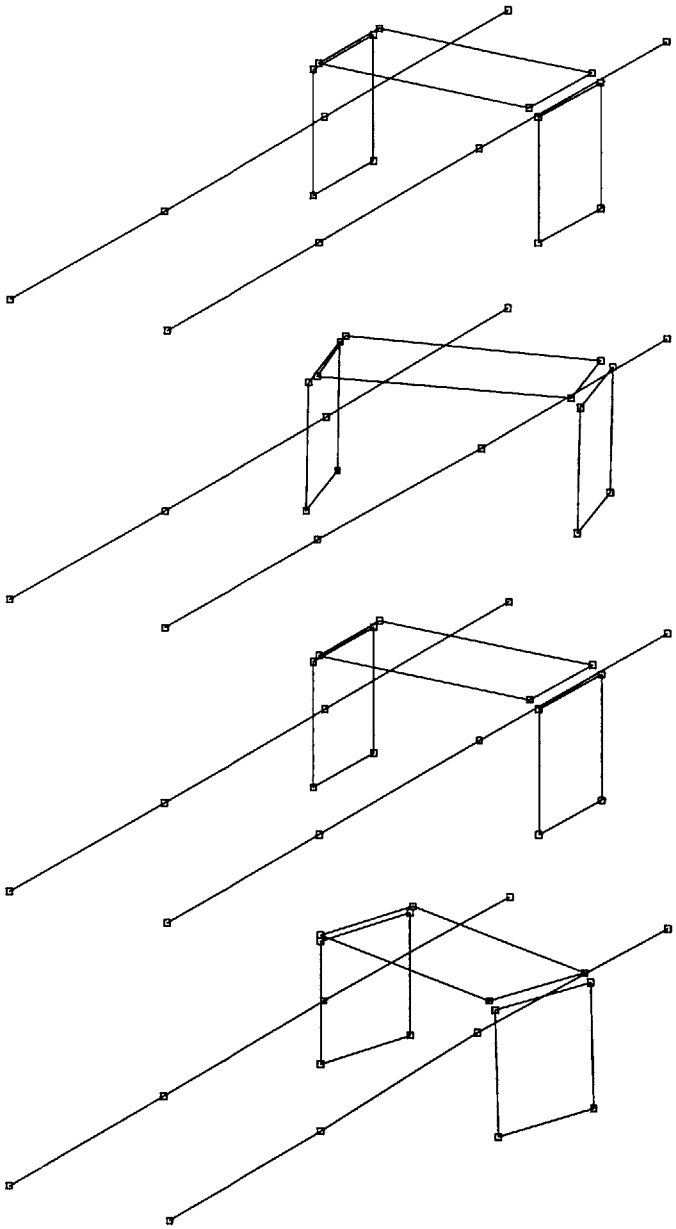

Figure 6.10: Measured yaw mode shape of the belt drive at 394 Hz. The figure shows snapshots of the mode starting from undeformed position. The small squares indicate measurement locations.

where the subscripts denote partial differentiation, y is the local transverse coordinate and ρ, $\lambda = \nu E_f/(1+\nu)(1-2\nu)$, and G are respectively, the density, complex Lame constant, and complex shear modulus of the material of the foam.

The boundary conditions for foam resemble the ones for the belt-foam systems of Section 4.5. At the interface between the foam and belt (at $y = 0$), the displacements in the foam must match those of the surface of the belt (as stated in Section 4.5.1). Hence we obtain

$$u(x, 0, \omega) = u_b(x, \omega) \tag{6.5}$$
$$v(x, 0, \omega) = 0 \tag{6.6}$$

At the free surface of the foam (at $y = h_f$), the normal and shear stresses must vanish. Hence we have

$$\lambda u_x(x, h_f, \omega) + (\lambda + 2G) v_y(x, h_f, \omega) = 0 \tag{6.7}$$
$$G(u_y(x, h_f, \omega) + v_x(x, h_f, \omega)) = 0 \tag{6.8}$$

Carriage, Motor and Pulleys

The carriage is subject to the force exerted by the belt (at $x = x_c$ and $x = x_c + w$) in addition to a disturbance force $F_c(\omega)$ and an effective viscous damping force $j\omega C_c u_c(\omega)$. Therefore the equation of motion for the carriage takes the form

$$-m_c\omega^2 u_c(\omega) + j\omega C_c u_c(\omega) + EA\left[u_b'(x_c, \omega) - u_b'(x_c + w, \omega)\right] = F_c(\omega) \tag{6.9}$$

where m_c is the mass of the carriage.

The motor armature is subject to the twisting moment imposed by the drive pulley on the coupling in addition to the actuation torque $T_m(\omega)$ and an effective viscous damping torque $j\omega C_m\theta_m(\omega)$. The equation of motion of the motor armature therefore takes the form

$$-\omega^2 J_m\theta_m + j\omega C_m\theta_m(\omega) + \kappa_c\left[\theta_m(\omega) - \theta_1(\omega)\right] = T_m(\omega) \tag{6.10}$$

where κ_c is the torsional stiffness of the coupling and $\theta_1(\omega)$ is the angle of rotation of the drive pulley.

The drive pulley is subject to a moment imposed by the motor on the coupling in addition to a moment from the belt and an effective viscous damping

torque $j\omega C_1\theta_1(\omega)$. Likewise, the idler pulley is subject to a moment from the belt in addition to an effective viscous damping torque $j\omega C_2\theta_2(\omega)$. Denoting the inertias of the drive and idler pulleys by J_1 and J_2, we write the equations governing their motion as

$$\begin{aligned} -\omega^2 J_1\theta_1(\omega) + j\omega C_1\theta_1(\omega) + \kappa_c\left[\theta_1(\omega) - \theta_m(\omega)\right] & \\ -rEA\left[u_b'(0,\omega) + \hat{u}_b'(0,\omega)\right] &= 0 \quad (6.11) \\ -\omega^2 J_2\theta_2(\omega) + j\omega C_2\theta_2(\omega) + rEA\left[u_b'(L,\omega) + \hat{u}_b'(L,\omega)\right] &= 0 \quad (6.12) \end{aligned}$$

where $\theta_2(\omega)$ is the angle of rotation of the idler pulley, r and L are respectively, the radius and distance between the pulleys.

6.3.2 Simplified Lumped-Parameter Model

In this section, we simplify the model of the previous section to obtain a lumped-parameter model that can reasonably predict the frequency and damping of the drive resonance at which the motion of the carriage is out of phase with that of the motor. Because the frequency of the drive resonance is much lower than that of the longitudinal wave propagation in the belt, we use the analysis presented in the Section 4.5.3 to formulate the dynamics of the drive. Using the derivation presented in Section 4.5.3 (in particular (4.38) and (4.39)), we obtain the force exerted by the belt on the carriage in terms of the carriage displacement $u_c(\omega)$, and the rotation of the pulleys $\theta_1(\omega)$ and $\theta_2(\omega)$ and rewrite the equation of motion of the carriage (6.9) as

$$\begin{aligned} -m_c\omega^2 u_c(\omega) + j\omega C_c u_c(\omega) + k_1\left[u_c(\omega) - r\theta_1(\omega)\right] - \hat{k}_1\left[u_c(\omega) + r\theta_1(\omega)\right] & \\ +k_3\left[u_c(\omega) - r\theta_2(\omega)\right] - \hat{k}_3\left[u_c(\omega) + r\theta_2(\omega)\right] = F_c(\omega) \quad (6.13) \end{aligned}$$

The sum of the third and fourth terms in the above equation represents the force exerted on the carriage by the segment of the belt between the drive pulley and the carriage. Likewise, the sum of the fifth and sixth terms represents the force exerted on the carriage by the segment of the belt between the idler pulley and the carriage. The value of k's and $\hat{k}$'s in the above equation can be obtained from (4.36)–(4.37) and are given by

$$k_i = \frac{EA}{\ell_i} - \frac{bG\phi'(0)\ell_i}{12} \; ; \; i = 1,2,3 \quad (6.14)$$

$$\hat{k}_i = \frac{Gk_s b\ell_i \tan(k_s h_f)}{4} \; ; \; i = 1,2,3 \quad (6.15)$$

where the function $\phi(y,\omega)$ is defined in (4.29), k_s is the wave number associated with the propagation of shear waves in the foam, and the subscript i refers to the various segments of the belt: i=1, 2, and 3 are the portions of the belt between the drive pulley and carriage, drive and idler pulleys, and carriage and idler pulley, respectively. Next we rewrite the equations of motion for the pulleys (6.11) and (6.12) in a similar manner as

$$\begin{aligned} -\omega^2 J_1\theta_1(\omega) + j\omega C_1\theta_1(\omega) + \kappa_c\left[\theta_1(\omega) - \theta_m(\omega)\right] & \\ +rk_2\left[\theta_1(\omega) - \theta_2(\omega)\right] - r\hat{k}_2\left[\theta_1(\omega) + \theta_2(\omega)\right] &= 0 \quad (6.16) \\ -\omega^2 J_2\theta_2(\omega) + j\omega C_2\theta_2(\omega) & \\ +rk_2\left[\theta_2(\omega) - \theta_1(\omega)\right] - r\hat{k}_2\left[\theta_2(\omega) + \theta_1(\omega)\right] &= 0 \quad (6.17) \end{aligned}$$

Unless packaging constraints are severe it is usually possible to choose the coupling to be much stiffer than the belt and hence we can neglect its compliance in (6.10) and (6.16). When the carriage is at the end of travel close to the idler pulley, we can neglect the compliance of the belt between them in comparison to the other segments. Hence, we can further simplify the model by lumping the inertia of the idler pulley into the carriage to obtain a two-degree-of-freedom model with the motor rotation $\theta_m(\omega)$ and carriage displacement $u_c(\omega)$ as generalized coordinates. These simplified equations of motion take the following form:

$$\begin{aligned} -\omega^2\left[(J_m + J_1)/r^2\right]u_m(\omega) + j\omega C_m u_m(\omega) & \\ +(k_1+k_2)\left[u_m(\omega) - u_c(\omega)\right] - (\hat{k}_1+\hat{k}_2)\left[u_m(\omega) + u_c(\omega)\right] &= F_m(\omega) \quad (6.18) \\ -\omega^2\left[m_c + J_2/r^2\right]u_c(\omega) + j\omega C_c u_c(\omega) & \\ +(k_1+k_2)\left[u_c(\omega) - u_m(\omega)\right] - (\hat{k}_1+\hat{k}_2)\left[u_c(\omega) + u_m(\omega)\right] &= F_c(\omega) \quad (6.19) \end{aligned}$$

where we have introduced an equivalent motor displacement $u_m = r\theta_m$, an equivalent motor force $F_m = T_m/r$, lumped the viscous damping into C_m and C_c, and neglected the compliance and damping arising out of the segment of the belt between the carriage and the idler pulley.

Next, we plot in Figures 6.11 and 6.12 the predicted frequency responses from motor torque to motor and carriage positions for the case when there is no foam attached to the belt. In such a case it is generally difficult to predict the damping of the drive from first principles. Hence we assume a damping ratio of 0.0001 for the drive resonance to generate the plots of Figures 6.11 and 6.12. We observe from these figures that the predicted pole and zero

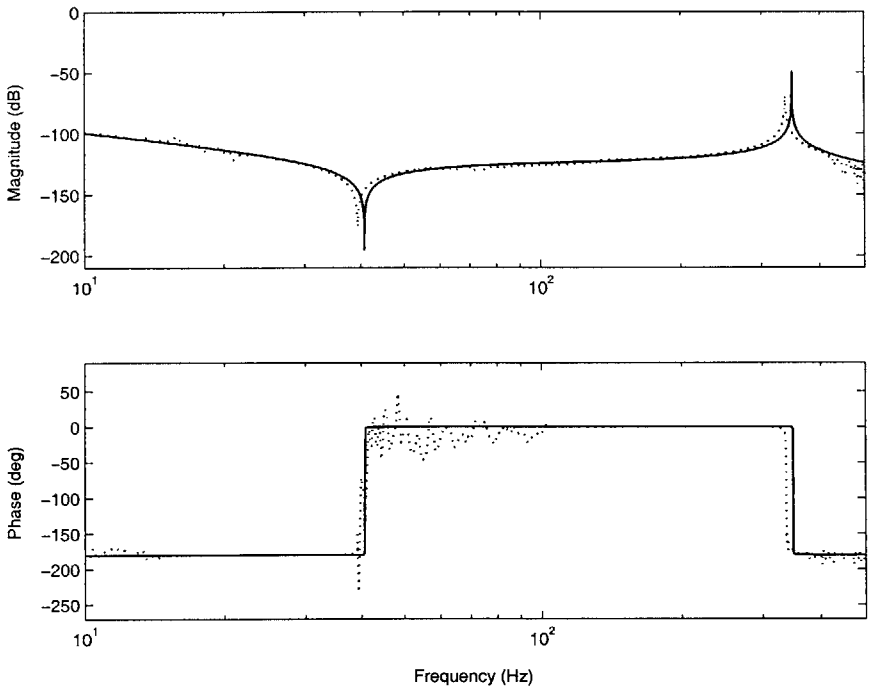

Figure 6.11: Comparison of the measured and predicted frequency responses from motor torque to motor position without foam: measured (dotted) and predicted (solid)

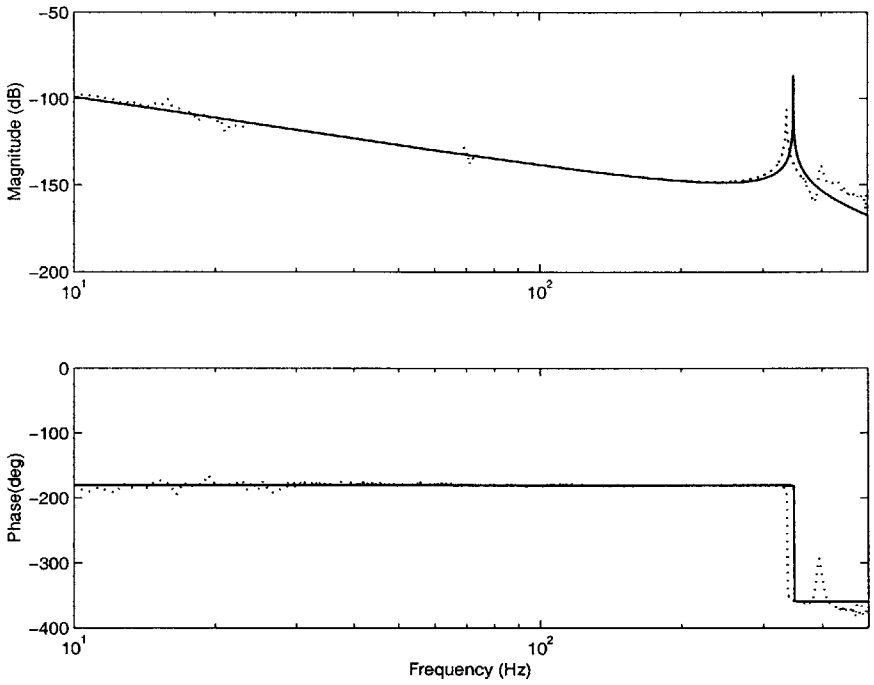

Figure 6.12: Comparison of the measured and predicted frequency responses from motor torque to carriage position without foam: measured (dotted) and predicted (solid)

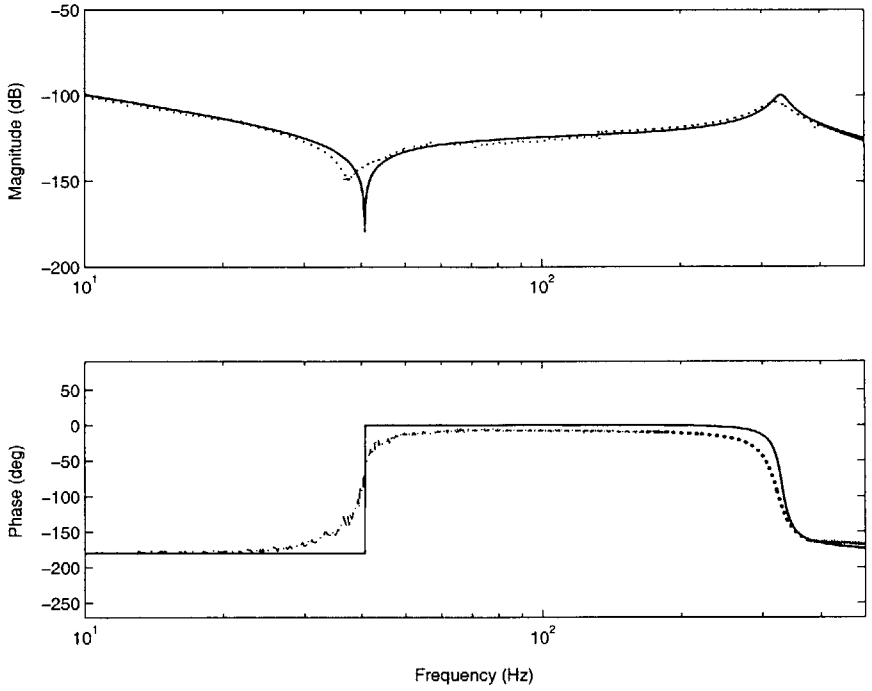

Figure 6.13: Comparison of the measured and predicted frequency responses from motor torque to motor position with foam: measured (dotted) and predicted (solid)

frequencies are in agreement with the measurements. Finally, we compare the predicted transfer functions for the drive with foam against the measurements in Figures 6.13 and 6.14. The results for the resonant frequency and damping are summarized in Table 6.2.

Discussion

The simplified two-degree-of-freedom model provided in the previous section reasonably captures the dynamics of the drive resonance as can be seen from Table 6.2. However, the model does not account for the damping arising from the segments of the belt between the carriage and idler pulley and those wrapped around the pulleys, and is moreover not suited for segments of the foam that are not much longer than their thickness. These approximations may account for the differences between theory and experiment. Figure 6.13

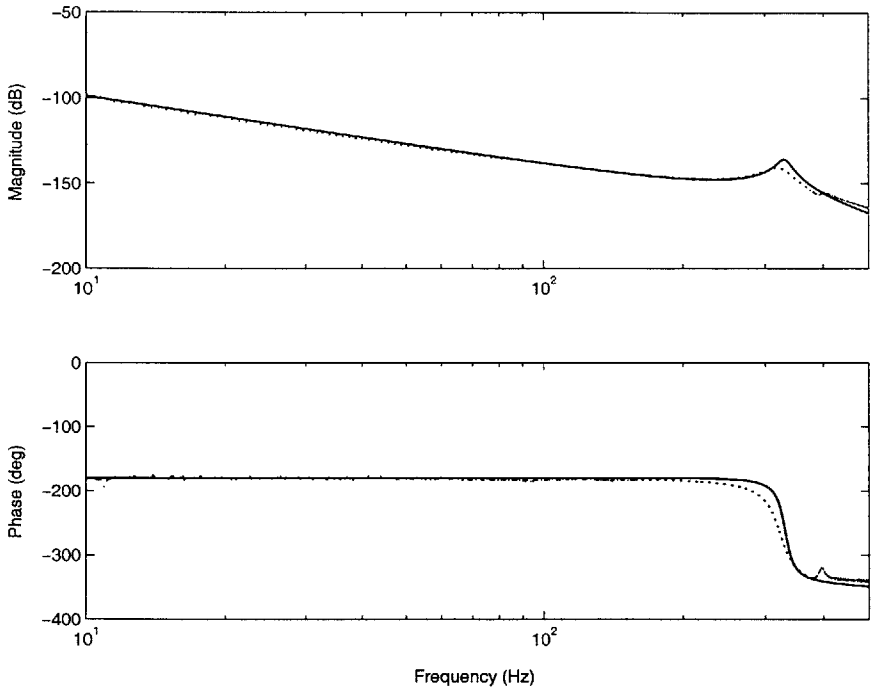

Figure 6.14: Comparison of the measured and predicted frequency responses from motor torque to carriage position with foam: measured (dotted) and predicted (solid)

Table 6.2: Predicted and measured frequencies and damping ratios for the drive resonance

	predicted		measured	
	frequency (Hz)	ζ	frequency (Hz)	ζ
without foam	348.0	–	337.0	0.001
0.5" C3201 foam	330.0	0.04	322.0	0.06

shows that the model has not captured the high damping of the complex zeros as measured in experiments. We attribute this significant low-frequency damping to regions of the belt-foam system where the length-wise boundary conditions in the foam become important. In the present configuration such regions include the segments of the belt wrapped around the pulleys and the one between the carriage and idler pulley.

As the carriage moves close to the motor, the frequency of drive resonance increases while the frequency of the mode in which the motion of the carriage is out of phase with that of the idler pulley decreases. This is because the compliance of the belt between the carriage and the motor decreases while the one between the carriage and idler pulley increases. However, the compliance of the belt between the two pulleys dominates over the one in segment 3 and therefore, the model described in (6.18) and (6.19) can still give good predictions for the drive resonance. But one must include the effect of the belt-foam segment between the carriage and idler pulley to get good estimates for damping.

Unlike the drive resonance, the mode in which the motion of the carriage is out of phase with the idler pulley does not drop phase in the transfer function from the motor torque to carriage position. Hence such a mode is not as detrimental for the feedback control control of the carriage (e.g., Varanasi [51]) and can be safely neglected in the model for simplicity. However, we can obtain good predictions for such a mode by augmenting the degrees of freedom in (6.18) and (6.19) with the rotation $\theta_2(\omega)$ of the idler pulley.

6.4 Chapter Summary

The results described in this chapter show that coupling a belt to a low-wave-speed medium is a low-cost method to provide predictable and relatively high damping in belt-driven positioning systems. Further, the foam medium can accomodate large strains and is so compliant that it introduces little creep into the structure. Experiments conducted on a belt-driven positioning stage incorporating a flat steel belt show significant increase in the damping of the drive resonance when a layer of foam is attached to the belt. Finally, a simple model is developed that is adequate for many purposes, especially that of designing a given amount of damping into the system.

CHAPTER 7

Design of Flexure Mechanisms for Dynamic Performance

7.1 Introduction

Flexures are mechanical elements which utilize the inherent elasticity of a material to provide smooth and precise motion. In contrast to conventional slideways, flexure mechanisms are free of wear and friction. Hence they are used in several precision engineering applications such as positioning stages, precision bearings, couplings, interferometers, optical scanners, and so on. They are also used to form "exact constraint" mounts for delicate objects (such as optical elements, instruments, and so on). However, such systems suffer from very lightly damped modes. In this study, we use a low-wave-speed medium to damp the vibratory modes of flexure assemblies in both the compliant and stiff directions.

Consider the flexure mechanisms sketched in Figures 7.1 and 7.2. It is common to operate such mechanisms under closed-loop control for precision positioning applications. But the presence of lightly-damped resonances and zeros affect the performance and stability of the stage (e.g., Varanasi [51]). In Section 7.2.1, we detail experiments on the single and double-parallelogram

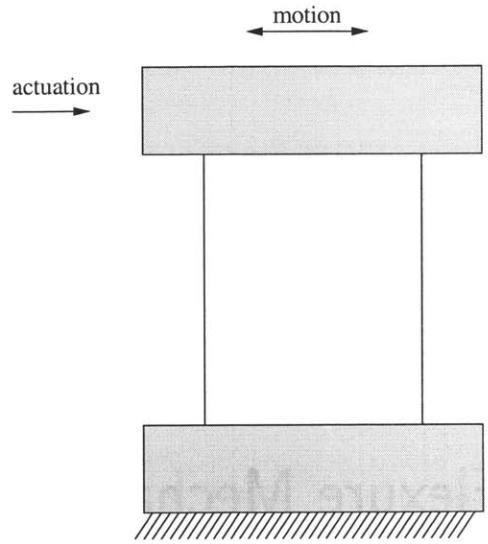

Figure 7.1: Schematic of the single-parallelogram flexure stage

flexure stages of Figures 7.3 and 7.8 and find that, by coupling the flexure blades with foam, relatively high and predictable damping can be introduced into most of the modes of the stage.

7.2 Flexures Coupled to Low-Wave-Speed Foams: Experiments and Design Guidelines

7.2.1 Experiments

In this section, we detail measurements on a pair of flexure mechanisms sketched in Figures 7.1 and 7.2. For each of the two stages we measure force-to-acceleration frequency responses by exciting the main mass using an impact hammer and measuring the response using an accelerometer. For the double-parallelogram stage we perform a set of modal tests to determine the mode shapes associated with the resonances of the stage.

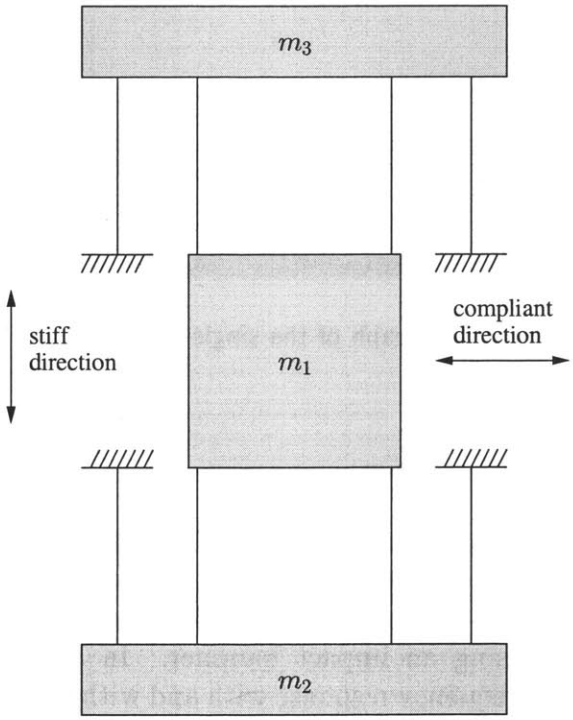

Figure 7.2: Schematic of the double-parallelogram flexure stage

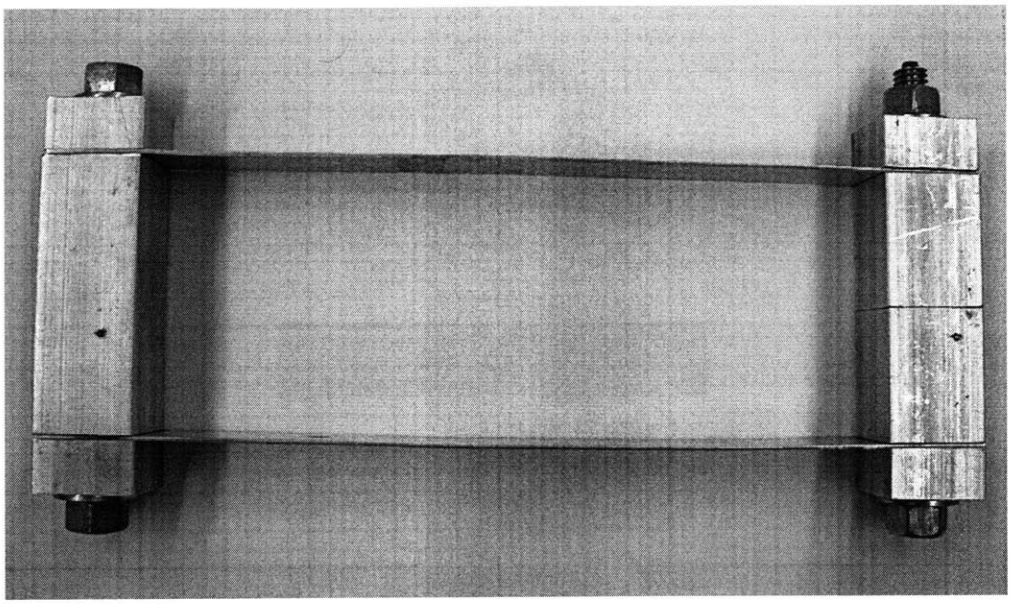

Figure 7.3: Photograph of the single-parallelogram flexure

Single-Parallelogram Flexure Stage

The single-parallelogram stage sketched in Figure 7.1 consists of aluminum blades of thickness 1 mm. A photograph of the stage is shown in Figure 7.3. The base of the stage is clamped to ground and the mass is excited in the compliant direction using an impact hammer. In Figure 7.4, we plot the force-to-acceleration frequency response with and without foam layers attached to the flexure blades. In the absence of foam layers, we find that the first resonance of the system arising from the compliance of the blades coupled with the inertia of the stage exhibits little damping ($\zeta < 0.0005$). Likewise, we find the higher modes (such as the out-of-plane and flexible modes of the blades) are also lightly damped. But when foam layers are attached to the blades as sketched in Figure 7.5 there is a significant increase in the damping of high-frequency modes. For example, the damping coefficient of the primary mode (first resonance) increases to 10.5% when 1.0 inch thick C3001 is attached to the blades.

Next, we fill the entire volume between the blades with foam as shown in Figure 7.6 and find that the damping of the first mode is further increased

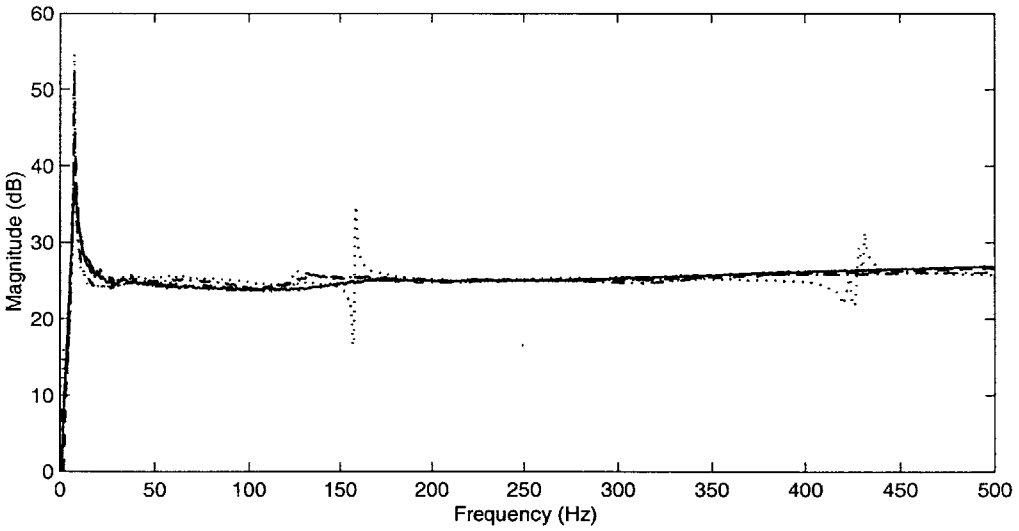

Figure 7.4: Measured force-to-acceleration frequency responses for single-parallelogram flexure: dotted (without foam), 0.5 inch thick C3201 foam attached to the blades (dash-dot), 0.5 inch thick C3001 foam attached to the blades (dashed), and 1 inch thick C3001 foam attached to the blades (solid)

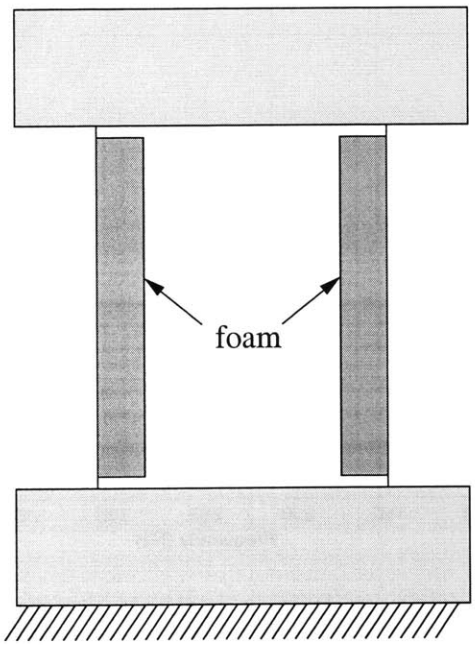

Figure 7.5: Schematic of the single-parallelogram flexure stage with foam layers attached to the blades

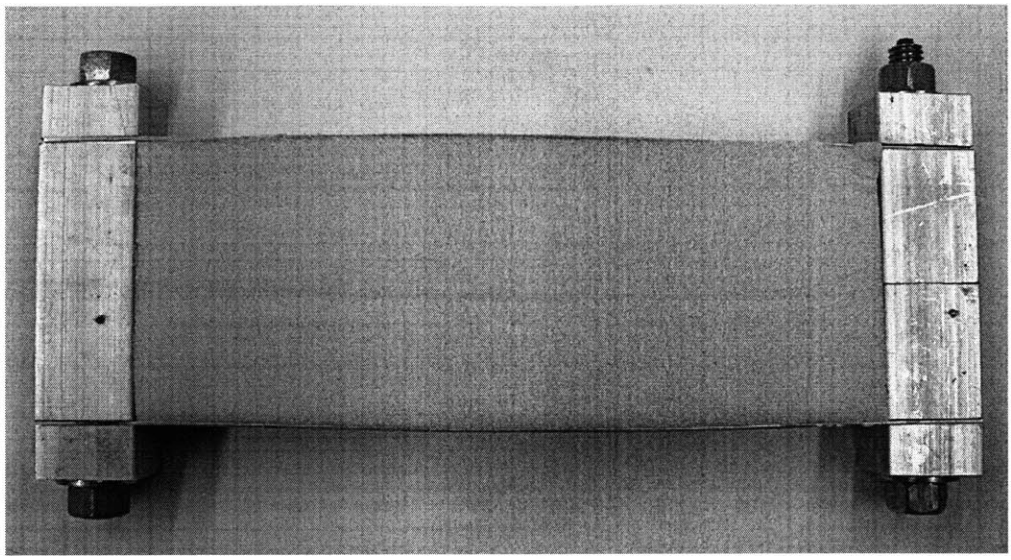

Figure 7.6: Photograph of the single-parallelogram flexure filled with foam

(as shown in Figure 7.7). This is accompanied by an increase in the static stiffness as can be noticed from the increase in the natural frequency of the mode. However, the range of travel is unaffected because the foam is very compliant and can tolerate large strains.

Double-Parallelogram Flexure Stage

In this section, we describe experiments conducted on the double parallelogram stage of Figure 7.2. A photograph of the stage is shown in Figure 7.8. The main mass m_1 is excited both in the compliant and stiff directions using an impact hammer and the response is measured using an accelerometer located at the center of the main mass m_1. We then plot the corresponding force-to-acceleration frequency responses in Figures 7.9 and 7.10. As expected, the stage exhibits very little damping in all of it modes. Next, we conduct modal tests on the stage to obtain the mode shapes associated with these resonances. In Figure 7.11, we show the location of the excitation and measurement positions employed for these tests. The points 2 through 5 are located at the four corners of the main mass m_1, 6 through 8 on the mass m_2, 9 through 11 on the mass m_3, and 12 through 15 on the base that is rigidly clamped to ground.

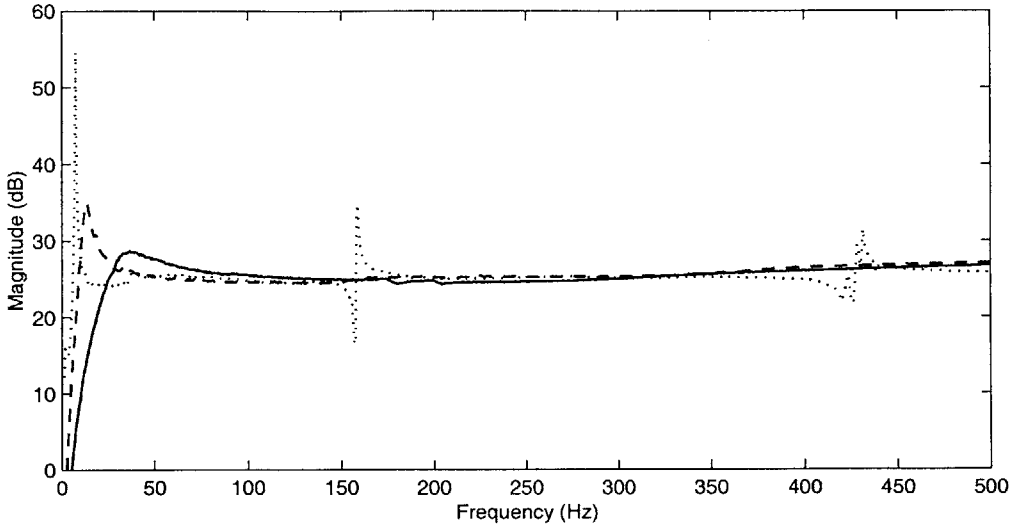

Figure 7.7: Measured force-to-acceleration frequency responses for single-parallelogram flexure: dotted (without foam), volume between blades filled with C3201 foam (dashed), volume between blades filled with C3201 foam (solid)

In Figures 7.12–7.14, we show a series of snapshots of several modes of the stage. The first and second resonances in the compliant direction correspond to modes in which the main mass m_1 moves in and out of phase with masses m_2 and m_3, respectively, as can be seen in Figures 7.12 and 7.13. Figure 7.14 shows one of the modes of the stage in which the mass m_1 exhibits out-of-plane motion.

When layers of foam are attached to the flexure blades as sketched in Figure 7.15, we see a significant increase in damping of the high-frequency modes of the stage (as shown in the frequency-response plots of Figures 7.16). The damping ratios of the first two modes in the compliant direction with and without foam layers are presented in Table 7.1. Next, we explore the configurations sketched in Figures 7.17–7.22 in which the volumes between the blades are filled with foam. As in the case of the single-parallelogram flexure, this leads to an increase in damping and static stiffness of the stage. However, this increase in static stiffness does not severely effect the range of travel of the main mass m_1.

In Figure 7.19, we plot the force-to-acceleration frequency response when

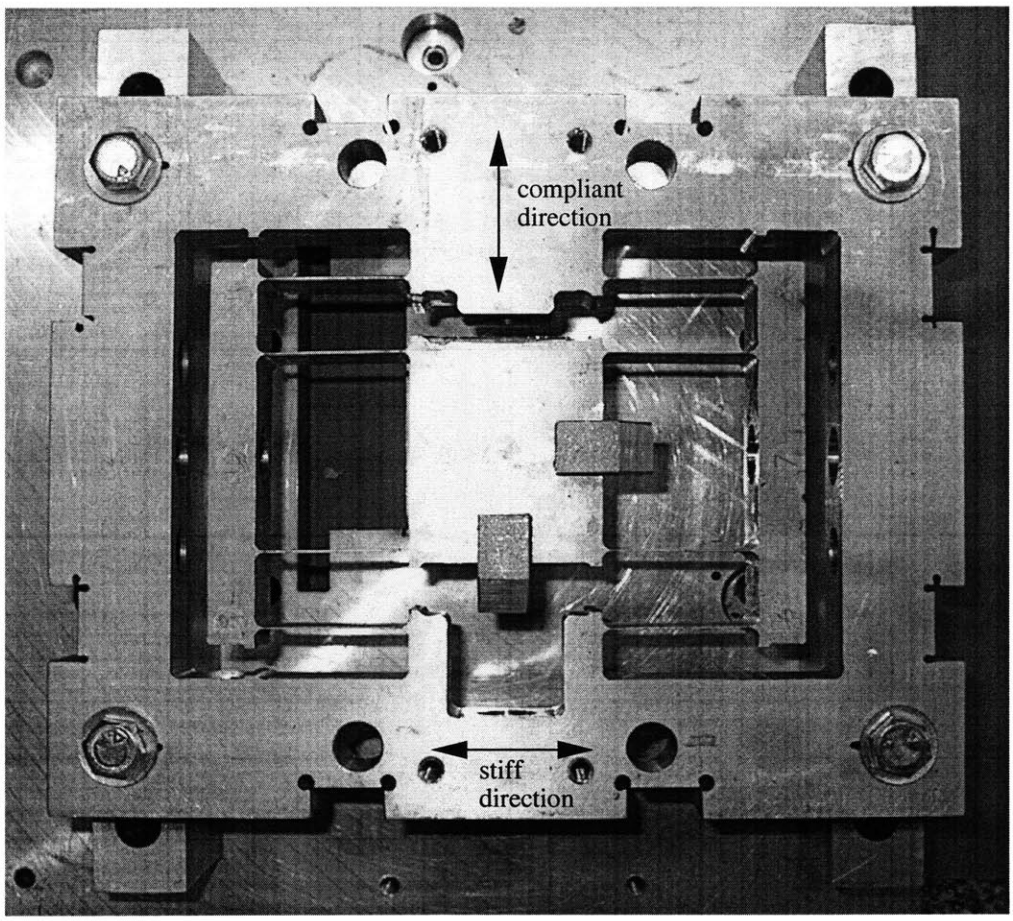

Figure 7.8: Photograph of the double-parallelogram flexure

Table 7.1: Comparison of damping ratios for the first two modes in the compliant direction with and without foam layers

	without foam	0.5" C3201	0.5" C3001
ζ of mode 1	0.3%	3%	3%
ζ of mode 2	0.3%	3.5%	4.6%

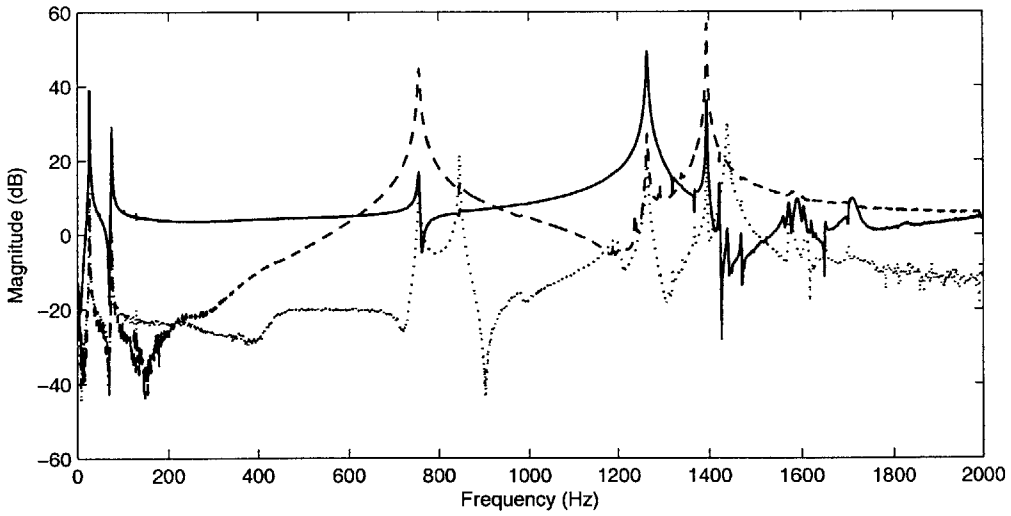

Figure 7.9: Measured force-to-acceleration frequency responses of the double-parallelogram stage when the main mass m_1 is excited in the compliant direction and the response is measured in compliant (solid), stiff (dashed), and out-of-plane directions (dotted).

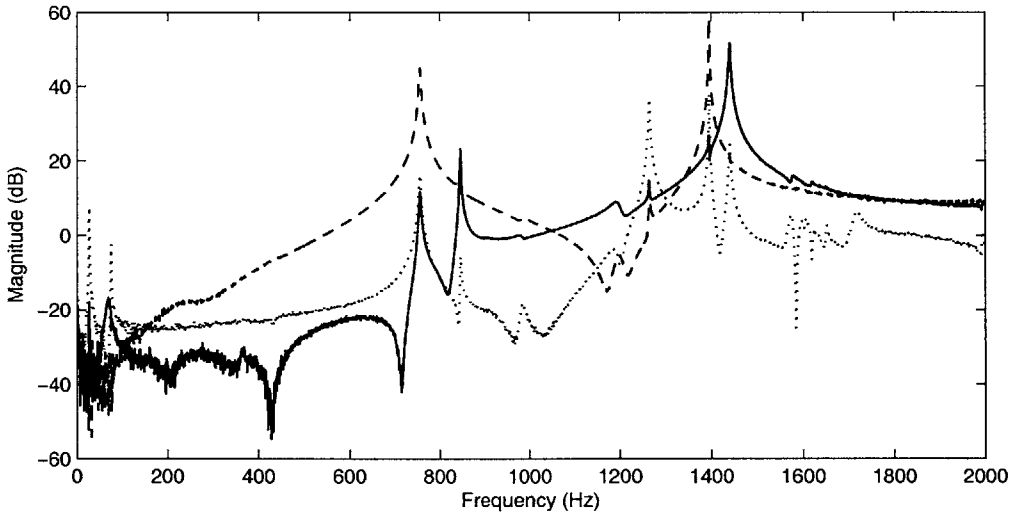

Figure 7.10: Measured force-to-acceleration frequency responses of the double-parallelogram stage when the main mass m_1 is excited in the stiff direction and the response is measured in stiff (solid), compliant (dashed), and out-of-plane directions (dotted).

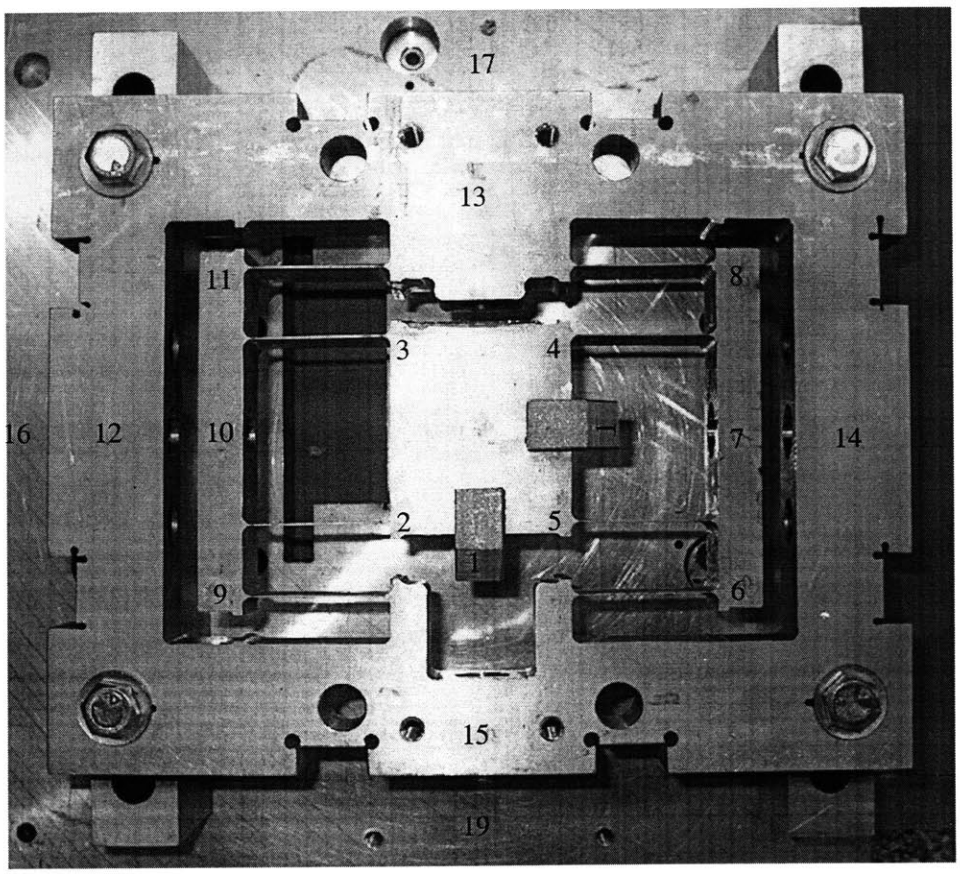

Figure 7.11: Photograph of the double-parallelogram flexure showing the excitation and accelerometer locations

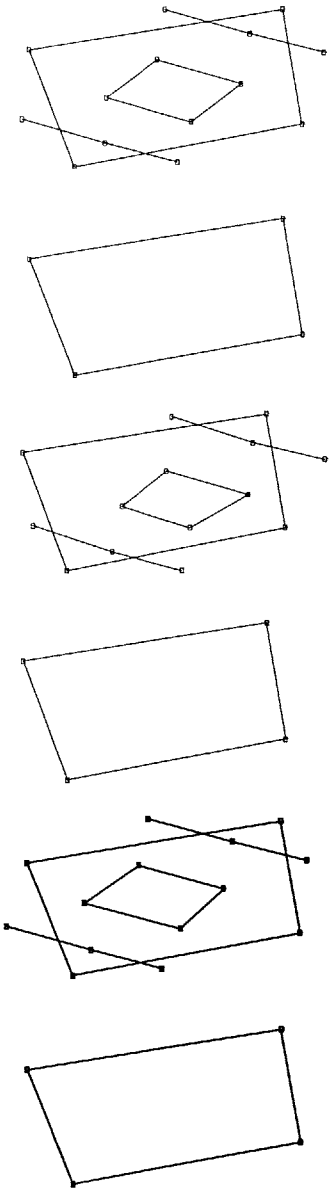

Figure 7.12: Measured mode shape of the stage at 27 Hz. The figure shows snapshots of the in-phase motion of m_1 with m_2 and m_3 starting from the undeformed position. The small squares indicate measurement positions.

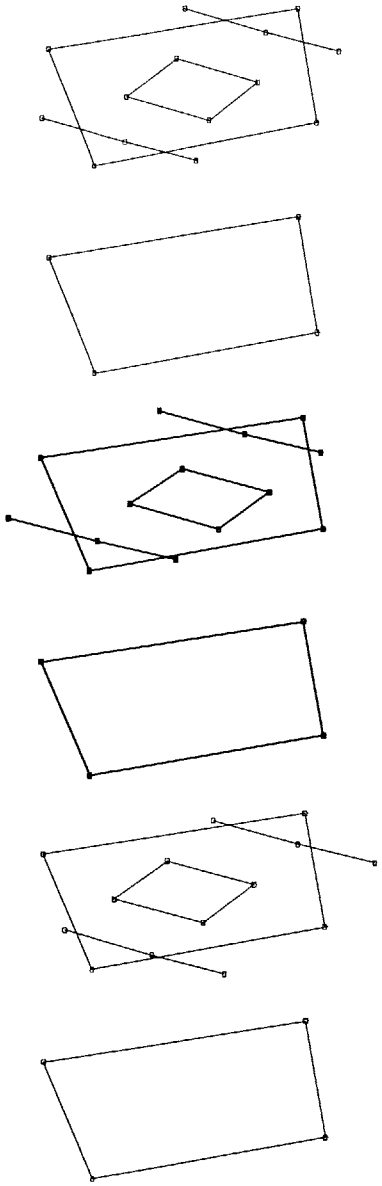

Figure 7.13: Measured mode shape of the stage at 75 Hz. The figure shows snapshots of the out-of-phase motion of m_1 with m_2 and m_3 starting from the undeformed position. The small squares indicate measurement positions.

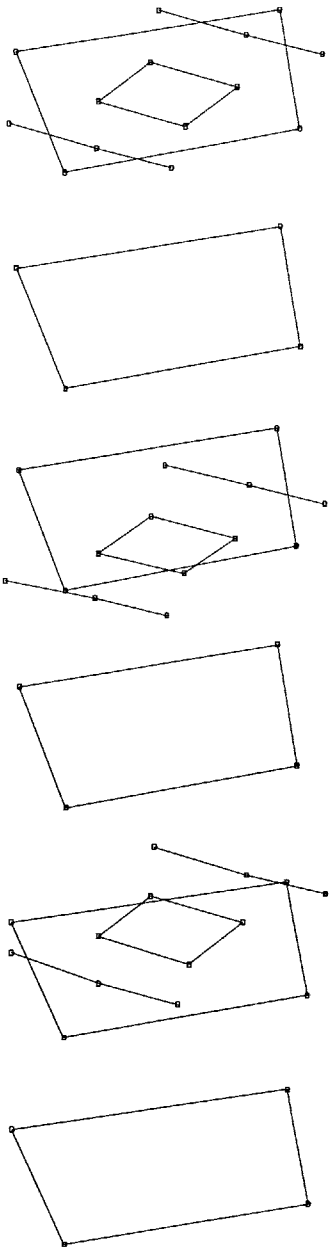

Figure 7.14: Measured mode shape of the stage at 780 Hz. The figure shows snapshots of the out-of-plane motion of the masses m_1, m_2, and m_3 starting from the undeformed position. The small squares indicate measurement positions.

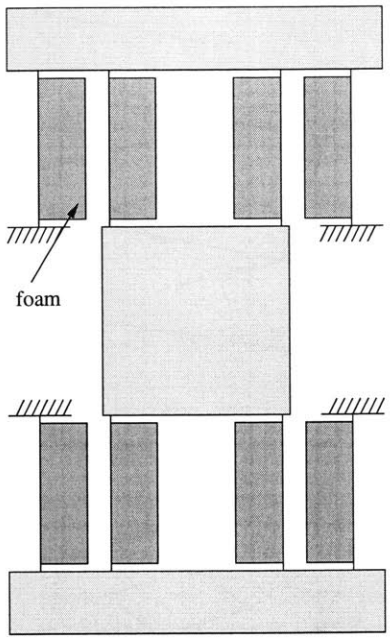

Figure 7.15: Schematic of the double-parallelogram flexure stage with foam layers attached to the blades

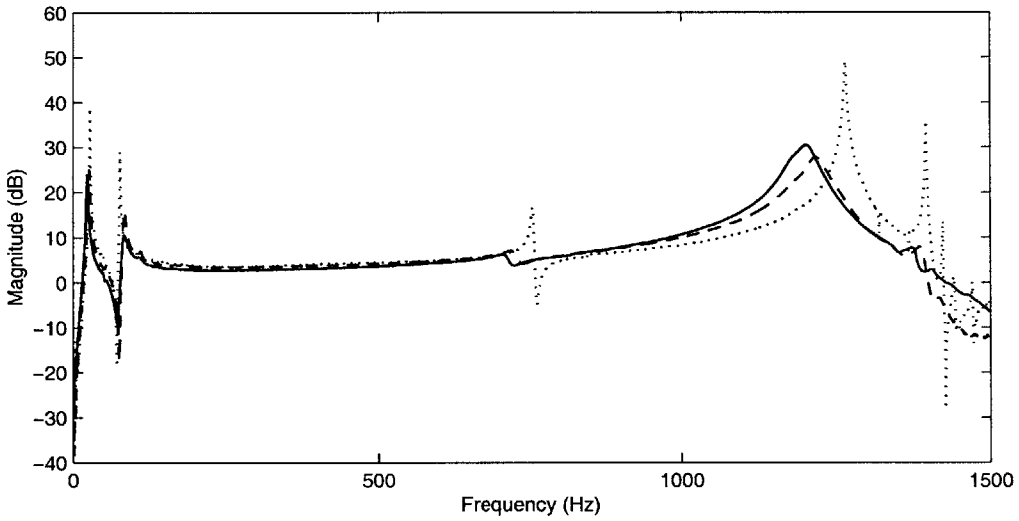

Figure 7.16: Measured force-to-acceleration frequency response of the double-parallelogram stage when the excitation and response are in the compliant direction: without foam (dotted), with 0.5 inch C3201 foam (dashed), and with 0.5 inch C3001 foam (solid)

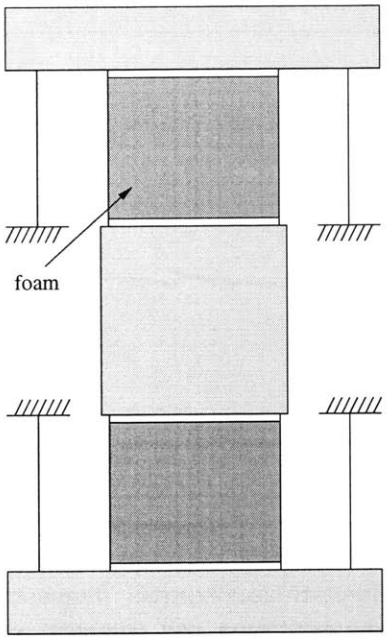

Figure 7.17: Schematic of the double-parallelogram flexure stage when the volume between the interior blades is filled with foam

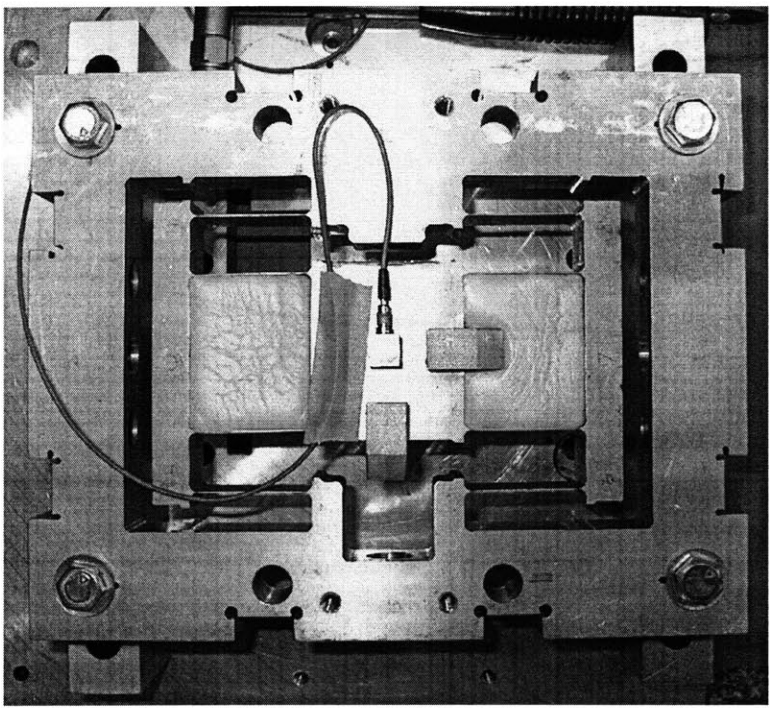

Figure 7.18: Photograph of the double-parallelogram flexure stage when the volume between the interior blades is filled with foam

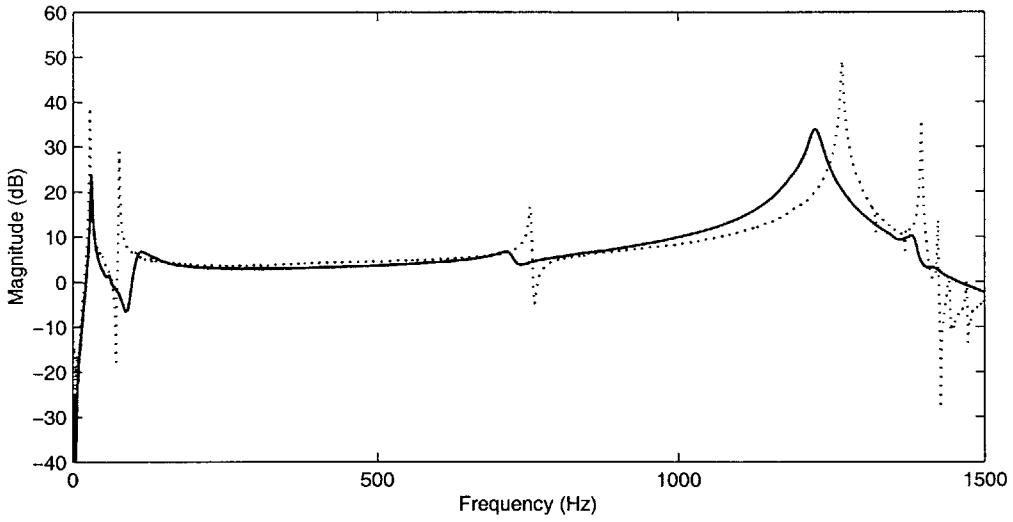

Figure 7.19: Measured force-to-acceleration frequency response of the double-parallelogram stage when the excitation and response are in the compliant direction: without foam (dotted) and when the volume between the interior blades is filled with C3201 foam (solid)

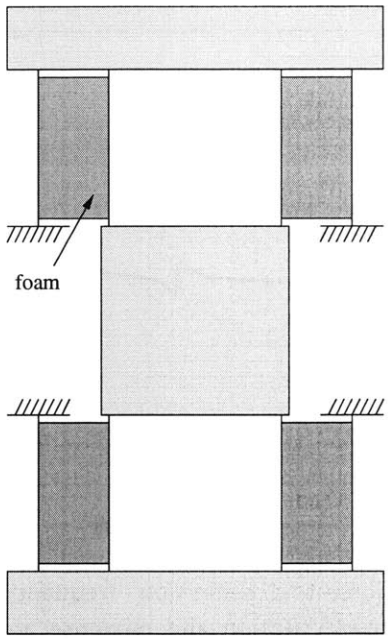

Figure 7.20: Schematic of the double-parallelogram flexure stage when the volume between the interior and exterior blades alone is filled with foam

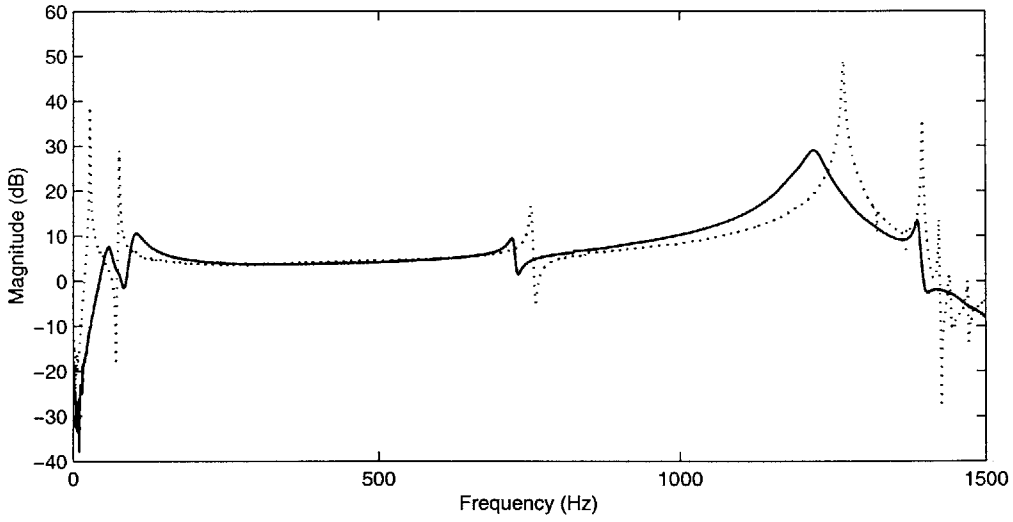

Figure 7.21: Measured force-to-acceleration frequency response of the double-parallelogram stage when the excitation and response are in the compliant direction: without foam (dotted) and when the volume between the interior and exterior blades alone is filled with C3201 foam (solid)

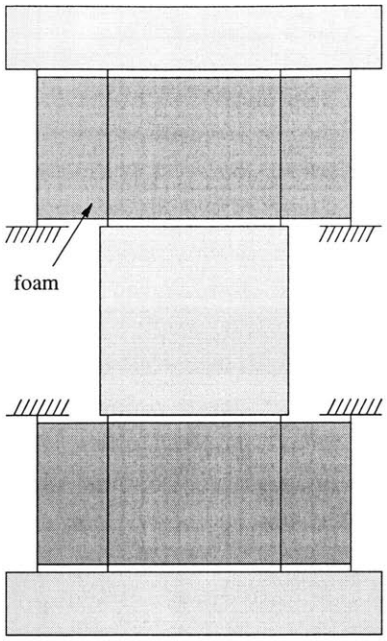

Figure 7.22: Schematic of the double-parallelogram flexure stage when the entire volume between the blades is filled with foam

the entire volume between the interior blades is filled with foam (as shown in Figures 7.17 and 7.18). Because there is no significant coupling in the first mode, we do not obtain high damping. However, we observe significant damping in the second mode as the motion of the mass m_1 is out of phase with that of m_2 and m_3. When foam is filled in the volume between the interior and exterior blades alone (as shown in Figure 7.20) , we find high damping in both modes as shown in Figure 7.21 because of the aforementioned reasons. Finally, the entire volume between the blades is filled (as shown in Figures 7.22 and 7.23), leading to significant damping in all modes of the stage as seen in the frequency response plot of Figure 7.24. As mentioned earlier, these configurations do not reduce the range of motion because the foam is compliant and can accommodate large strains.

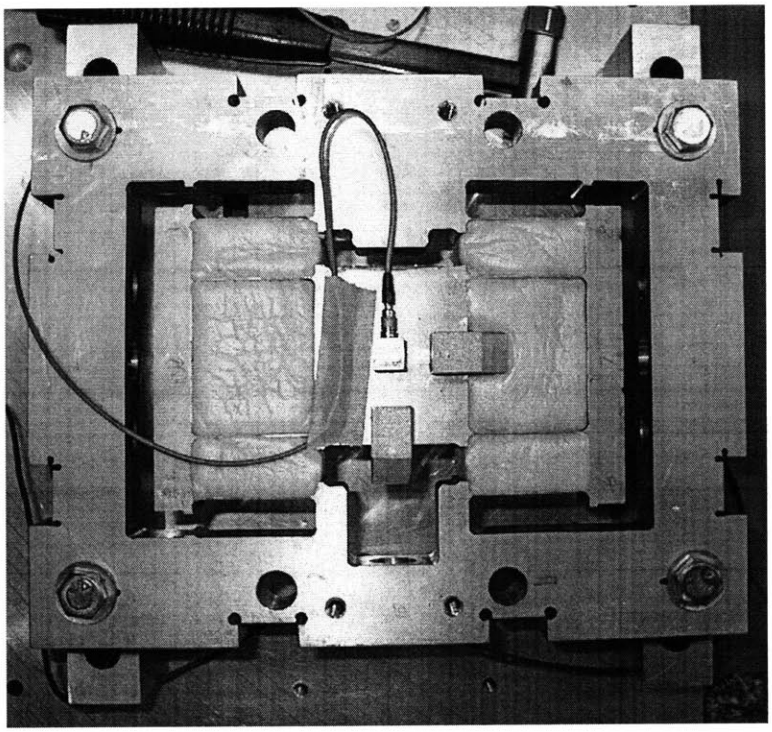

Figure 7.23: Photograph of the double-parallelogram flexure stage when the entire volume between the blades is filled with foam

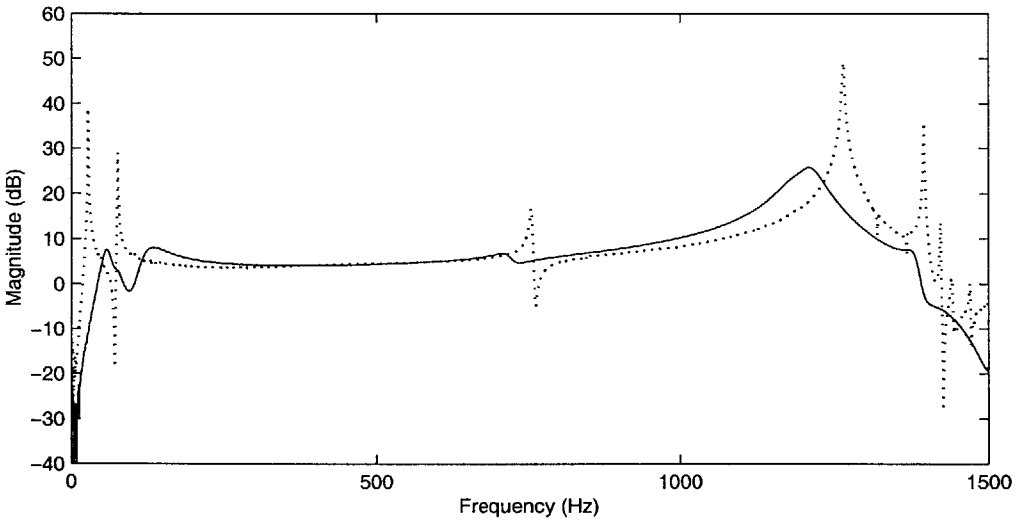

Figure 7.24: Measured force-to-acceleration frequency response of the double-parallelogram stage when the excitation and response are in the compliant direction: without foam (dotted) and when the entire volume between the blades is filled with foam (solid)

7.2.2 Discussion

Flexure mechanisms are usually operated under closed-loop control for precision-positioning applications. For the flexure stages described in the previous sections (Figures 7.1 and 7.2), the actuation and the feedback sensor locations lie on the same rigid body. Under this so-called collocated feedback the primary resonances can be easily compensated via closed-loop control. However, the higher modes (such as the out-of-plane modes, flexible blade modes and so on) can potentially affect stability and performance of the stage because it is difficult to robustly compensate for these modes using feedback control. From the experimental studies in the previous sections and chapters, we find that the low-wave-speed damping is well suited to solve this problem. Other important limitations for collocated control arise from lightly damped zeros in the transfer function (e.g., Varanasi [51]), and foam layers increase damping in the zeros of the system as well. For non-collocated applications, the drive resonance limits the achievable bandwidth (e.g., Varanasi [51]). Once again, low-wave-speed damping can be useful to increase the damping in such modes and significantly improve performance of the positioning stages.

In some of the experiments, particularly ones in which entire volumes between the blades are filled with foam, we notice an increase in the static stiffness. This would ordinarily give rise to creeping deflections. But as these stages are usually operated under closed-loop control, any creep introduced in this manner can be eliminated. Likewise, for applications in which flexures are used as kinematic mounts the creeping deflections that may be introduced in the compliant direction for a given flexure are counteracted by the constraints imposed by other flexures in that direction.

7.2.3 Estimates for Damping

In order to obtain estimates for the loss factor of the various modes of the stage, we can use approaches similar to the ones outlined in the previous chapters. Depending on the mode shape we can obtain compatible displacements in foam (for example, by expanding displacements in terms of a Fourier series or eigenfunctions), solve for the wave propagation in foam and combine it with the dynamics of the stage to obtain estimates for damping. For example, by using the dimensional analysis provided in Chapter 5, we find that the product of the wave number k_f and thickness h_f of the foam should be around unity

to maximize the damping. Under such conditions we find the loss factor to be

$$\eta/m_r \approx 0.3 \; ; \; h_f k_f \approx 1 \tag{7.1}$$

Likewise, we can use the models derived in Chapters 4 and 5 (Section5.2) to obtain estimates for the loss factors of the longitudinal modes of the system. In particular, the model for the belt-foam systems (Section 4.5) can be used to obtain the damping introduced into the stretching modes of the blades.

7.3 Chapter Summary

This chapter shows that damping can be introduced into flexures in a very effective manner using low-wave-speed media. The method is tested on two flexure configurations and several experiments have been documented. The results show that above a "cut-off" frequency relatively high and predictable damping can be introduced into several modes of the stage. Also depending on the thickness, density, and speed of sound of the medium, even the lowest modes can be damped without affecting the range of travel of the stage.

CHAPTER 8

Closure

8.1 Findings

Our studies in this thesis show that significant damping can be attained with little added mass by coupling a structure to a lossy medium with low density and low speed of sound. We find that whenever the frequencies lie in a certain favorable range governed by the wave propagation in the low-wave-speed medium, strong interaction between the vibrating structure and medium occurs, resulting in high damping. Such damping treatments (whether the low-wave-speed medium is powder, foam, or some other material) offer a low-cost method of attaining broad-band damping in structures and machines. Further, these materials can accommodate large strains and are so compliant that they introduce little creep into a structure.

We have developed simple linear models that can predict the damping phenomenon with reasonable accuracy. Approximate solutions are developed by expanding the displacement of the structure in terms of its mode shapes, solving for compatible vibration in the low-wave-speed medium, and thence computing the response of the combined system. The results are found to be in close agreement with measured responses. We have also presented simplified models and characterized the damping in terms of the important non-dimensional parameters of the system. Finally, we have applied this approach

to belt drives and flexure mechanisms to improve their performance.

8.2 Future Work

The results described in this thesis suggest that any form of vibration can be damped if the appropriate coupling between the structure and low-wave-speed medium can be achieved. Hence a natural extension would be to use this approach to damp torsional modes of a structure.

It has been shown by Ruiji [43] that an effective method to shield radiative heat transfer from and to a structure is to cover it with a thin layer of aluminum and maintain an air gap in between them. We intend to use a similar approach, but instead fill the air gap with a low-wave-speed medium. This approach then yields a good thermal shield as well as a vibration damper. Further, any acoustic radiation onto the structure is also shielded because of the lossy low-wave-speed medium. In Figure 8.1, we show a schematic of this combined acoustic, thermal, and vibration damper applied to precision assemblies. This approach has been applied to a periscope stage for the LIGO (Laser Interferometer Gravity Wave Observatory) project. A photograph of the periscope stage is shown in Figure 8.2. An accelerometer mounted on the stage is used to record the power spectrum from ambient ground vibrations. These measurements are shown in Figure 8.3 with and without foam layers. We see that there is a reduction in the peak by a factor of five when a layer of foam along with a thin sheet of steel shield is attached to the stage. In the future we would like to study further this combined acoustic, thermal and vibration damper.

Next, we would like to explore means to excite other kinds of waves in these systems. For example, by making a "cut" in the foam as shown in Figure 8.4, we find an increase in damping of the beam. In Figure 8.5, we compare the force-to-acceleration frequency response of the usual beam-foam system (of Figure 3.4) to that of the system sketched in Figure 8.4 and find that there is a significant increase in damping in the first mode due to the cut. This suggests that the cut has resulted in the establishment of lower-frequency waves in foam. Other configurations of interest would be segmentation of the foam in the length-wise direction. This would possibly help set up standing waves in the length-wise direction and help increase damping at lower frequencies, particularly in longitudinal modes. In the future, we wish to study other configurations to couple waves between the low-wave-speed medium and the

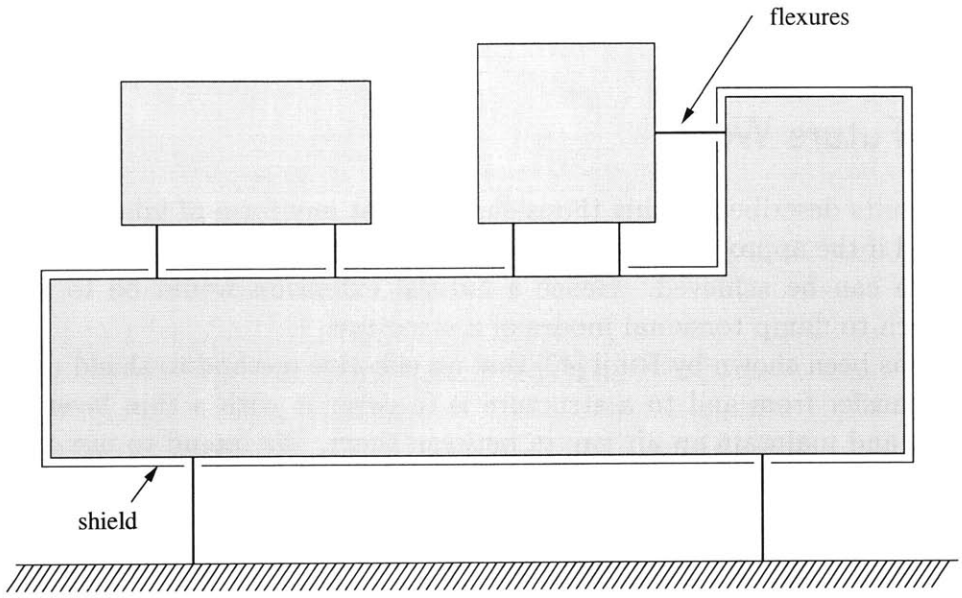

Figure 8.1: Schematic of the combined acoustic, thermal, and vibration damper. The gap between the shield and the structure is filled with a low-wave-speed medium

structure.

In the area of low-density granular materials, more detailed studies are required to understand the linearity of the damping phenomenon and the effect of "packing" on attainable damping. It may be that, by packing the powder more densely, shear waves can be coupled into it and the behavior of powder will approach that of a foam.

Other studies of interest would include: fundamental physics of wave propagation in materials with feature lengths comparable to that of wavelength; guiding waves by creating gradients in the material properties and its effect on the attainable damping; use of magnetic or electrical coupling via magnetic or dielectric particles in powder or foams to enhance the dynamic interaction between the structure and low-wave-speed medium; effect of anisotropy of materials on damping; other materials (e.g., for high-temperature applications one could use steel wool; vacuum compatible materials), and so on. We find that this area is rich and that there are innumerable possibilities for future research.

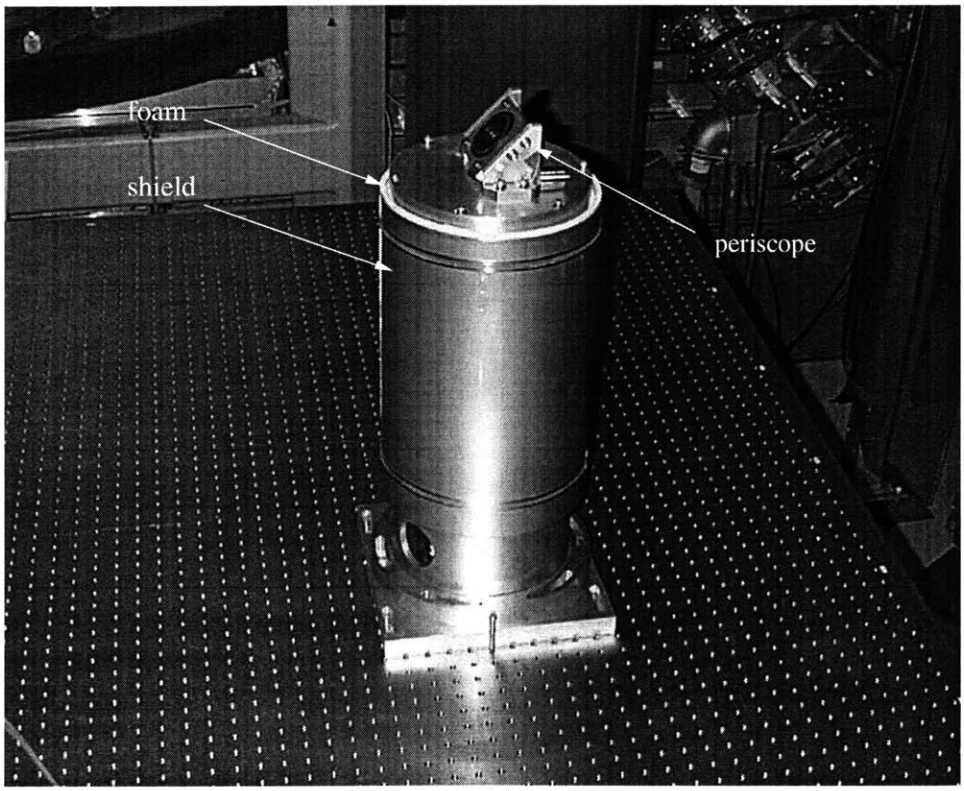

Figure 8.2: Photograph of the LIGO periscope stage

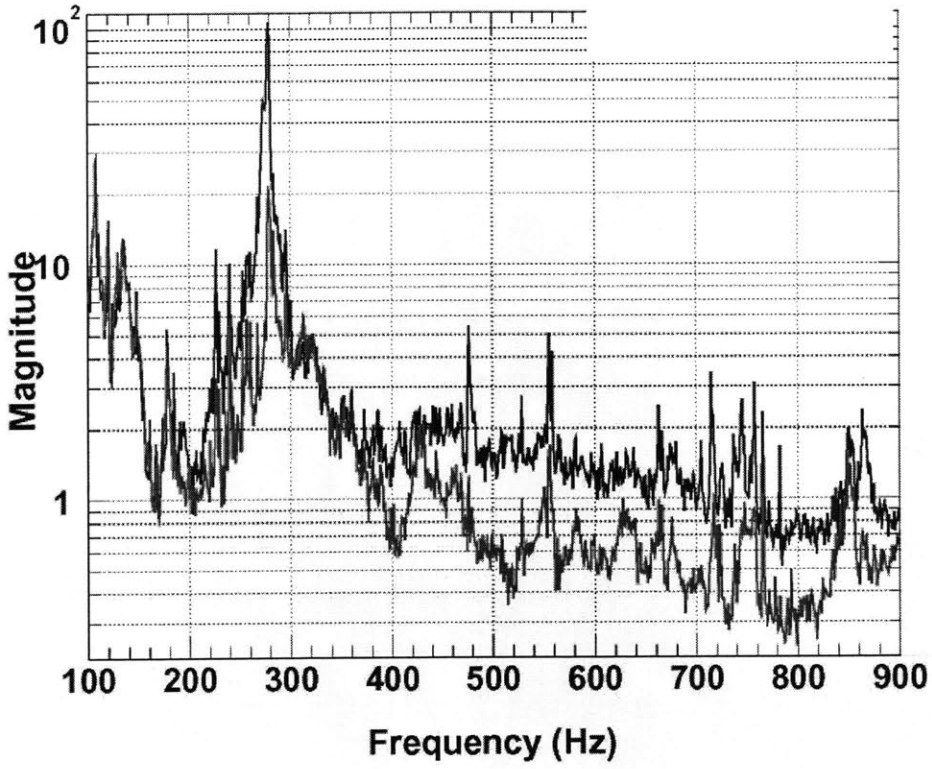

Figure 8.3: Measured power spectra for the LIGO stage under ambient vibrations: without foam (blue) and with foam (red). When the structure is wrapped in foam there is reduction in the peak by about a factor of five

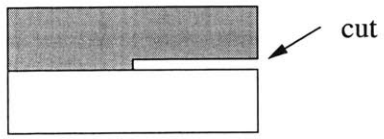

Figure 8.4: Schematic of the "cut" made in foam

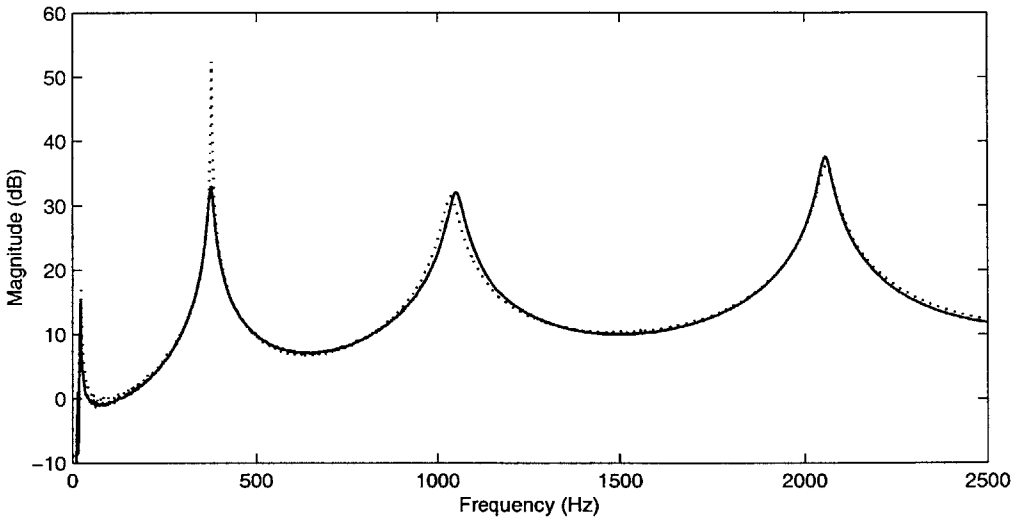

Figure 8.5: Comparison of the force-to-acceleration transfer functions for an aluminum beam of length 584.8 mm: foam (dotted) and foam with a cut as shown in Figure 8.4 (solid)

Appendix A

Measuring the Speed of Sound in Powder

In this section, we document a set of experiments in which we determine the speed of sound and loss factor of the granular medium employed in this paper. The experimental set up consists of a powder-filled acrylic tube whose cross section is shown schematically in Figure A.1. At one end of the tube (at $x = 0$) a plunger is used to impose a displacement on the powder. The plunger is driven using an electromagnetic shaker via an accelerometer. At the other end of the tube (at $x = L$), a plunger is held against a rigid support by means of a force transducer to simulate a fixed end. A photograph of the experimental set up is shown in Figure A.2. Next, by imposing a sinusoidal displacement at the free end and varying its frequency, we obtain transfer functions between the acceleration at the free end and the force at the fixed end. Because of the free-fixed boundary conditions, we expect resonances to occur in the acceleration-to-force transfer function at frequencies where the length of the tube is an integer multiple of half the wave length in the powder.

In Figure A.3, we plot the measured acceleration-to-force transfer function for a tube whose length and diameter are 254 mm and 22.8 mm, respectively. We find that the primary resonance occurs at 114 Hz and the resonance frequencies occur in the ratio of 1:2.02:3.02:4.03, which is close to that expected

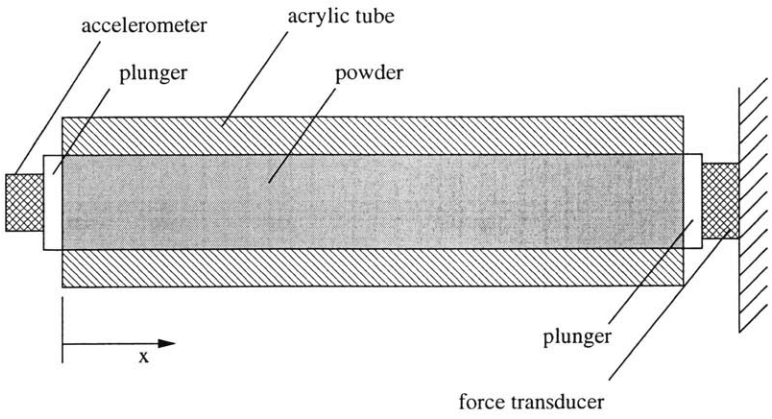

Figure A.1: Schematic of the experiment employed to determine the properties of powder

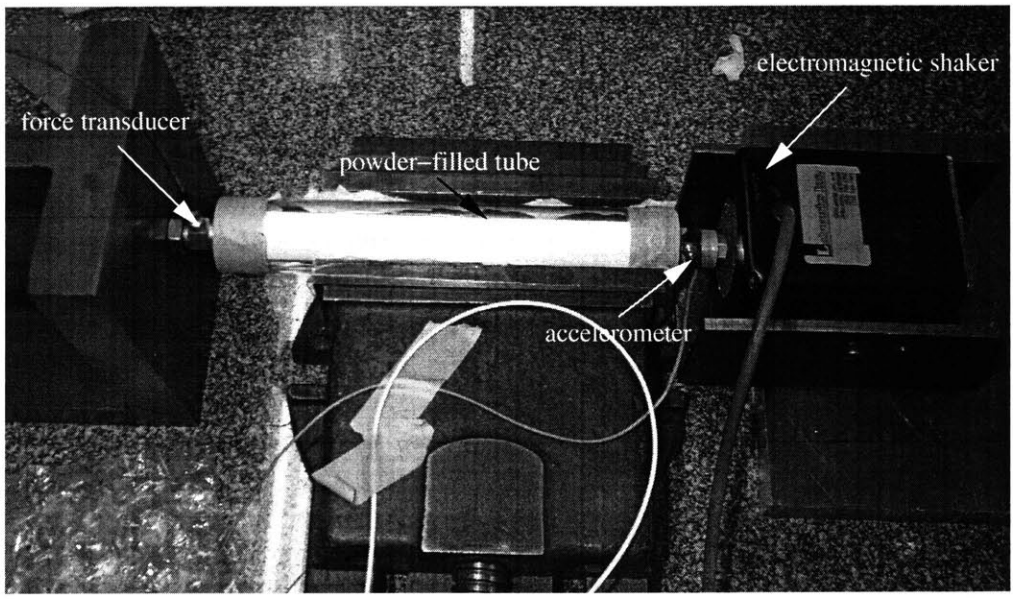

Figure A.2: Photograph of the experiment employed to determine the properties of powder. The picture shows the powder-filled tube, electromagnetic shaker, and the transducers.

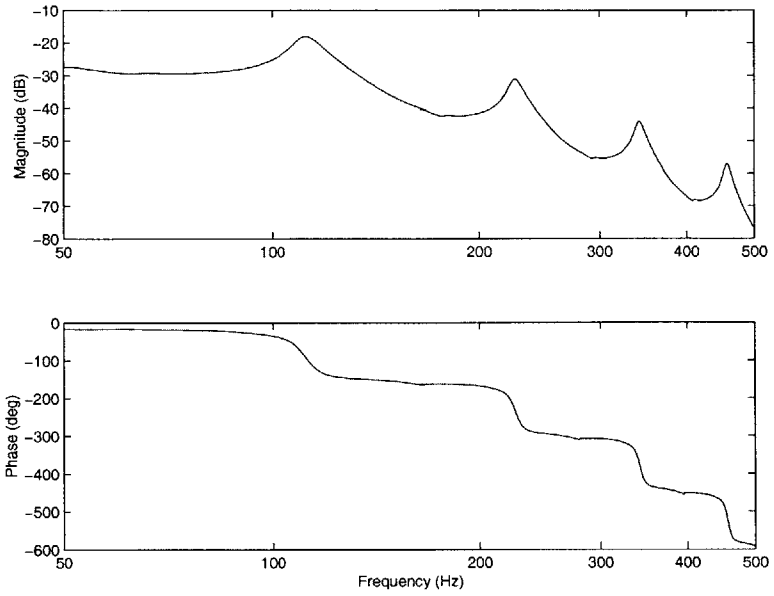

Figure A.3: Measured acceleration-to-force frequency response of the system shown in Figure A.1 employed to determine the properties of powder. The length of the tube is 254 mm

from theory. Based on the values of these resonance frequencies, we compute the speed of sound in the powder to be approximately 58 m/s. Next, we obtain the loss factor for the various modes in this transfer function using standard modal curve-fitting software such as Star Modal (Spectral Dynamics [46]). We find that the loss factor is independent of frequency and has a value of approximately 0.20.

Appendix B

Material Properties of Foam

In this section, we document a set of experiments conducted to determine the elastic moduli and loss factor of the foam. The extensional modulus is determined by exciting a layer of foam sandwiched between two aluminium discs as shown in Figure B.1. One of these discs is driven using an electromagnetic shaker to impose a displacement which is measured using an accelerometer on the foam where as the other disc is held against a rigid support by means of a force transducer to simulate a fixed end. Next, by imposing a sinusoidal displacement at the free end and varying its frequency, we obtain the frequency response between the acceleration at the free end and the force at the fixed end as shown in Figure B.2. Noting that the magnitude of the response $M(\omega)$ has no resonance peaks and the phase $\theta(\omega)$ is more or less constant, we conclude that for the range of frequency used in the experiments, there is no significant wave propagation in the layer of foam. We therefore conclude that the layer of foam behaves as a simple hysteretic spring (e.g., Crandall [11]; Nashif *et.al.*[31]) and obtain its complex extensional modulus $\hat{E}_f(\omega)(1 + j\eta_e(\omega))$ from

$$\hat{E}_f(\omega)(1 + j\eta_e(\omega)) = \frac{\omega^2 M(\omega)(1 - j\tan\theta(\omega))}{\sqrt{1 + (\tan\theta(\omega))^2}} \frac{t}{A} \tag{B.1}$$

where t and A are respectively, the thickness and the cross-sectional area of the layer of foam. In Figure B.3, we plot the real part of the modulus E_f as

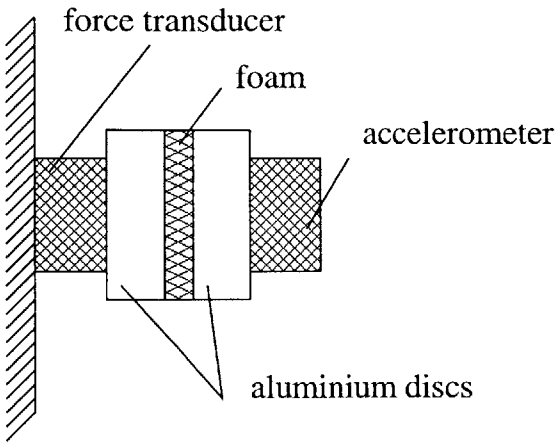

Figure B.1: Schematic of the experiment employed to determine the extensional modulus of foam

a function of frequency and find that the extensional modulus is proportional to the square root of the frequency. Next, as the phase of the acceleration-to-force transfer function is approximately -140^o over the given frequeny range, we compute the loss factor of the material of the foam in extension to be approximately 0.8.

Next, we conduct a similar experiment to determine the shear modulus of the foam material. The experiment consists of a rectangular aluminium block mounted onto a U-shaped block via a pair of layers of foam ($15.5\times15.5\times3.2$ mm) as sketched in Figure B.4. The rectangular aluminium block is driven using an electromagnetic shaker via an accelelrometer to impose a displacement on the layers of the foam. The U-shaped block is held against a rigid support via a force transducer to simulate a fixed end. Because of the symmetry in this arrangement the foam layers are in pure shear as the rectangular block undergoes harmonic motion. As in the extensional case, we find from the frequency response between the acceleration at the free end and the force at the fixed end (plotted in Figure B.5) that the the layers of foam behave as hysteretic springs. Next, we compute the complex shear modulus of the foam in a manner similar to the one described for the extensional case. Finally, we plot the real part of the shear modulus $\hat{G}_f$ in Figure B.6. We find that the shear modulus is proportional to the square root of the frequency whereas the loss factor is approximately 0.8. Becasue the extensional and shear moduli

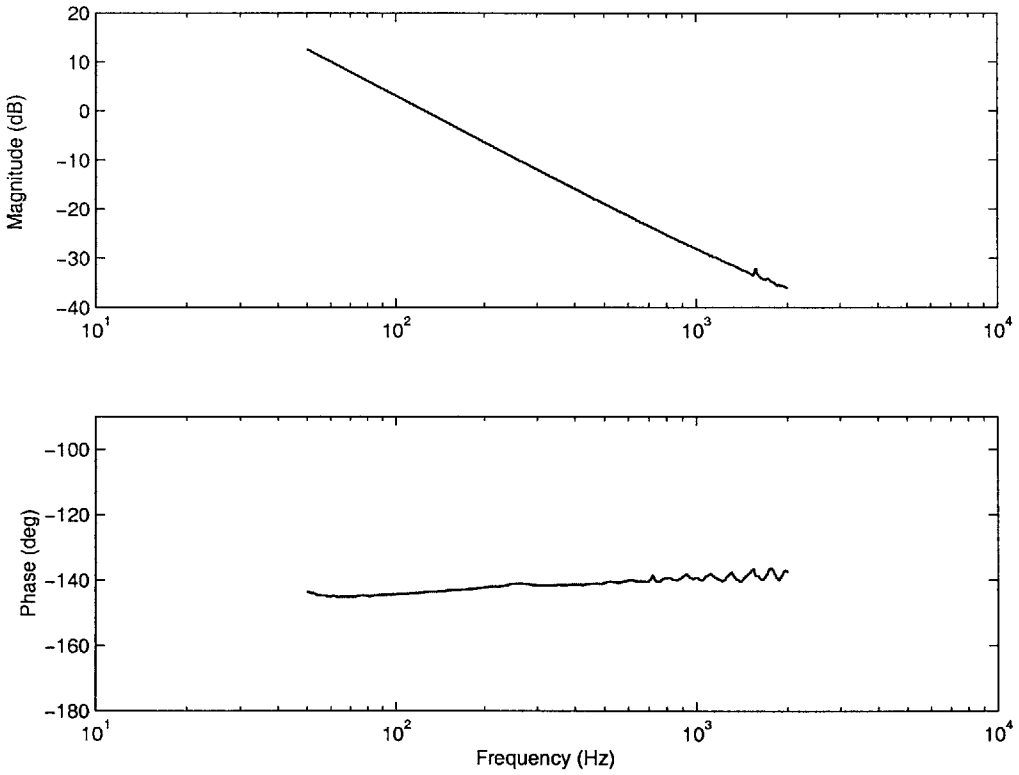

Figure B.2: Measured acceleration-to-force frequency response of the system shown in Figure B.1 employed to determine the extensional modulus of the foam

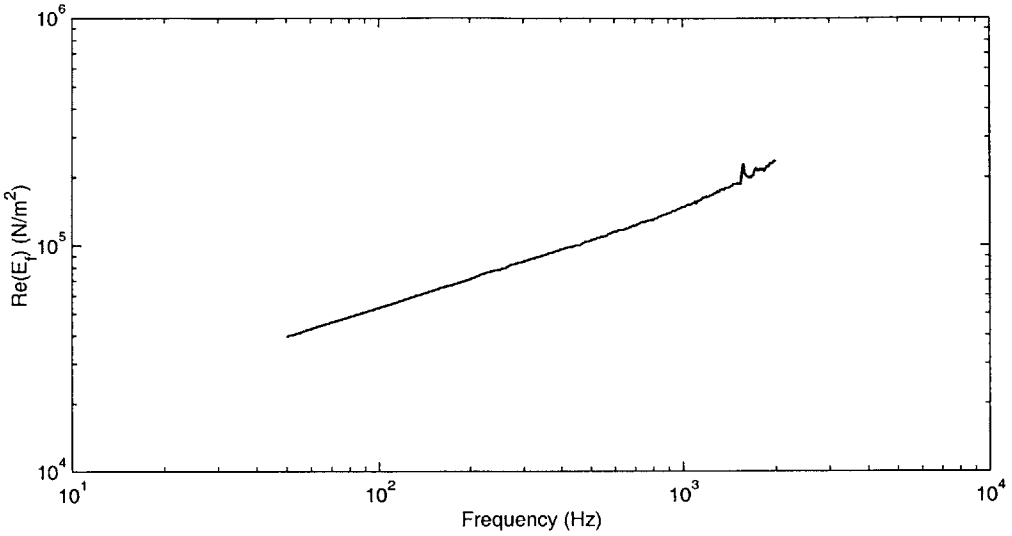

Figure B.3: Measured real part of the extensional modulus and the loss factor

vary in a similar manner with frequency, we conclude that the poisson ratio of the foam is independent of frequency and is approximately 0.36.

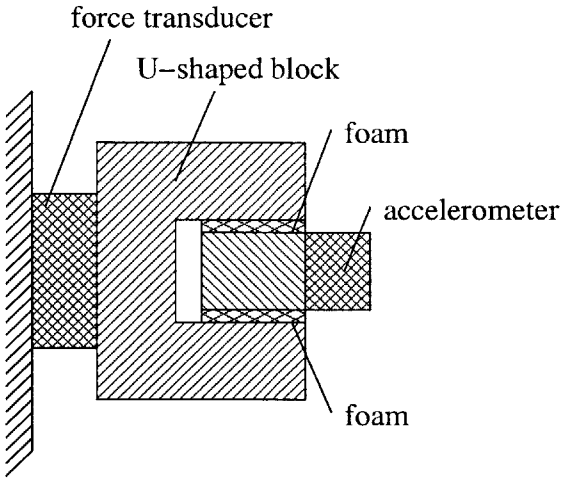

Figure B.4: Schematic of the experiment employed to determine the shear modulus of foam

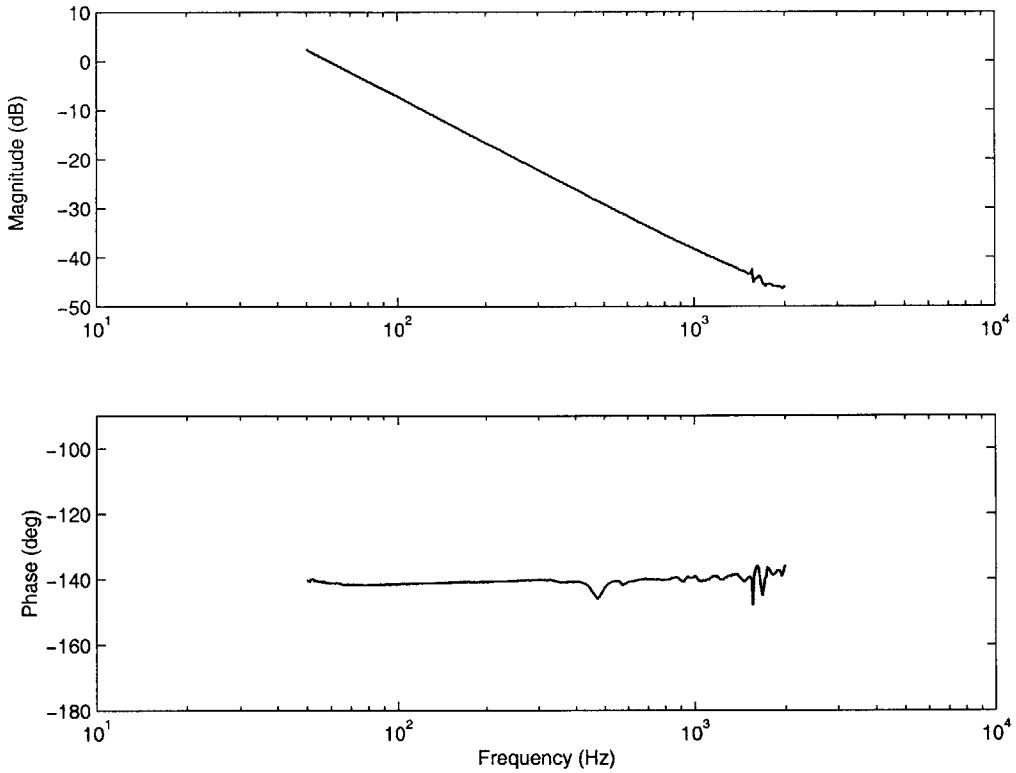

Figure B.5: Measured acceleration-to-force frequency response of the system shown in Figure B.4 employed to determine the shear modulus of the foam

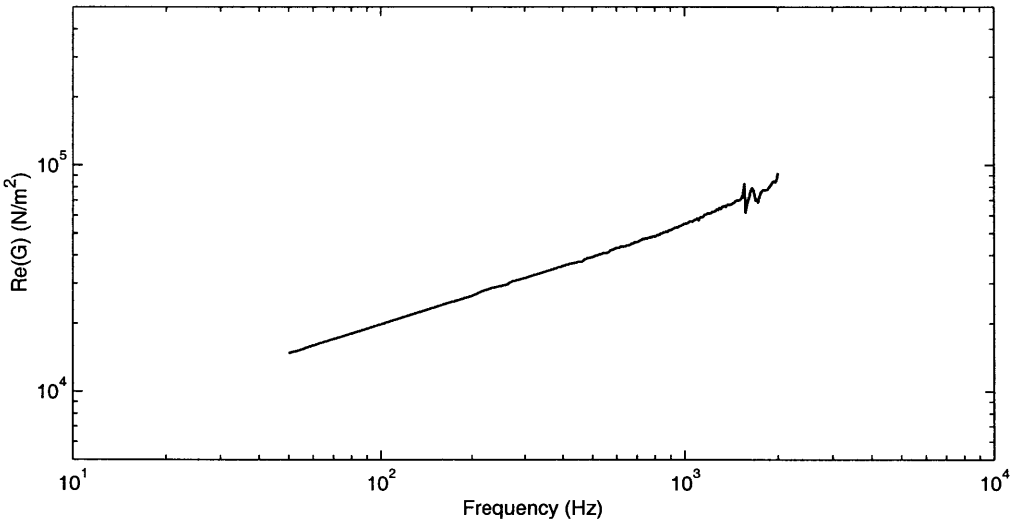

Figure B.6: Measured real part of the shear modulus and the loss factor in shear of the foam

Bibliography

[1] 3M Adhesives, St. Paul, MN 55144. *Adhesive Data Sheet.*

[2] 3M Speciality Materials, St. Paul, MN. *3M Microspheres Selection Guide.*

[3] S. Abrate. Vibration of belts and belt drives. *Mechanism and Machine Theory*, 27(6):645–659, 1992.

[4] Aerotech Inc., Pittsburgh, Pennsylvania. *Motor Catalog.*

[5] Anon. Stainless steel belts for robotic handling in semi-conductor industry. *Assembly Automation*, 22(2):176–176, 2002.

[6] L. Beranek and L. Ver. *Noise and Vibration Control Engineering: Principles and Applications.* Wiley, New York, 1992.

[7] M.A. Biot. Theory of propagation of elastic waves in a fluid-saturated porous solid. I. low-frequency range. II. higher frequency range. *Journal of the Acoustical Society of America*, 28:168–191, 1956.

[8] J.S. Bolton, N.M. Shiau, and Y.J. Kang. Sound transmission through multi-panel structures lined with elastic porous materials. *Journal of Sound and Vibration*, 191(3):22–27, 1996.

[9] W.J. Book. Controlled motion in an elastic world. *ASME Transactions: Journal of Dynamic Systems, Measurement and Control*, 115:252–261, 1993.

[10] J.M. Bourinet and D. Le Houedec. A dynamic stiffness analysis of damped tubes filled with granular material. *Computers and Structures*, 73:395–406, 1999.

[11] S.H. Crandall. The hysteretic damping model in vibration theory. *Journal of Mechanical Engineering Science*, 25:23–28, 1991.

[12] L. Cremer and M. Heckl. *Structure-Borne Sound.* Springer-Verlag, 1973.

[13] dSPACE Inc., Novi, Michigan. *dSPACE 1103 User's Manual.*

[14] E-A-R Speciality Composites, 7911 Zionsville Road, Indianapolis, IN 46268. *EAR Technical Data Sheet.*

[15] P. Evesque. Shaking dry powders and grains. *Contemporary Physics*, 33(4):245–261, 1992.

[16] Bryce L. Fowler, Eric M. Flint, and Steven E. Olson. Effectiveness and predictablility of particle damping. In *Smart Structures and Materials 2000: Damping and Isolation*, volume 3989, pages 356–367. SPIE, 2000.

[17] J.R. Fricke. Lodengraf damping—an advanced vibration damping technology. *Sound and Vibration*, pages 22–27, July 2000.

[18] R. Gueler, A.H. von Flowtow, and D.W. Vos. Passive damping for robust feedback control of flexible structures. *Journal of Guidance, Control, and Dynamics*, 16(4):662–667, 1993.

[19] N.W. Hagood, W.H. Chung, and A. Von Flowtow. Modelling of piezoelectric actuator dynamics for active structural control. *Journal of Intelligent Material Systems and Structures*, 1(3):327–354, July 1990.

[20] N.W. Hagood and von Flotow. Damping of structural vibrations with piezoelectric materials and passive electrical networks. *Journal of Sound and Vibration*, 146(1), April 1991.

[21] K. Hutter and K.R. Rajagopal. On flows of granular materials. *Continuum Mechanics and Thermodynamics*, 6:81–139, 1994. Review article.

[22] C.D. Johnson. Design of passive damping systems. *Transactions of ASME: Journal of Mechanical Design*, 117:171–176, June 1995.

[23] K.L. Johnson. *Contact Mechanics.* Cambridge University Press, first edition, 1985.

[24] E.M. Kerwin. Damping of flexural waves by a constrained viscoelastic layer. *Journal of Acoustical Society of America*, 31(7):952–962, 1959.

[25] Y.S. Kim, K.W. Wang, and H.S. Lee. Feedbak control of er-fluid-based structures for vibration suppression. *Smart Materials and Structures*, 1(2):139–145, June 1992.

[26] L.E. Kinsler, A.R. Frey, A.B. Coppens, and J.V. Sanders. *Fundamentals of Acoustics.* John-Wiley, 2000.

[27] B.J. Lazan. *Damping of Materials and Members in Structural Mechanics.* Pergammon Press, London, 1968.

[28] J.M. Lighthill. *Waves in Fluids.* Cambridge University Press, first edition, 1979.

[29] E.R. Marsh and A.H. Slocum. An integrated approach to structural damping. *Precision Engineering*, 18(3):103–109, 1996.

[30] D.J. Mead and S. Markus. The forced vibration of a three-layer, damped sandwich beam with arbitrary boundary conditions. *Journal of Sound and Vibration*, 10(2):163–175, 1969.

[31] A.D. Nashif, D.I.G. Jones, and J.P. Henderson. *Vibration Damping.* John Wiley, New York, 1985.

[32] S.A. Nayfeh. *Design and Applications of Damped Machine Elements.* PhD thesis, Massachusetts Institute of Technology, Cambridge, Massachusetts, June 1998.

[33] S.A. Nayfeh and K.K. Varanasi. A model for the damping of torsional vibration in thin-walled tubes with constrained viscoelastic layers. *Journal of Sound and Vibration*, in press.

[34] S.A. Nayfeh, J.M. Verdirame, and K.K. Varanasi. Damping of flexural vibration by coupling to low-density granular materials. In G. Agnes, editor, *Smart Structures and Materials 2002: Damping and Isolation*, volume 4697, pages 158–167. SPIE, March 2002.

[35] New Way Air Bearings, Aston, Pennsylvania. *www.newwaybearings.com.*

[36] H.V. Panossian. Structural damping enhancement via non-obstructive particle damping technique. *Journal of Vibration and Acoustics*, 114(1):101–105, 1992.

[37] H.V. Panossian. Non-obstructive particle damping experience and capabilities. In *Proceedings of IMAC-XX: A Conference on Structural Dynamics*, volume 4753, pages 936–941, Los Angeles,CA, February 2002. SPIE.

[38] A. Papalou and S. Masri. Response of impact dampers with granular materials under random excitation. *Earthquake Engineering and Structural Dynamics*, 25:2530–67, 1996.

[39] A. Papalou and S. Masri. An experimental investigation of particle dampers under harmonic excitation. *Journal of Vibration and Control*, 4:361–379, 1998.

[40] PCB Piezotronics, 3425 Walden Avenue, Depew NY 14043. *Shock and Vibration Sensors Catalog.*

[41] E.J. Richards and A. Lenzi. On the prediction of impact noise, VII: the structural damping of machinery. *Journal of Sound and Vibration*, 97(4):549–586, 1984.

[42] D. Ross, E. Ungar, and E.M. Kerwin. Damping of plate flexural vibrations by means of viscoelastic laminae. In J.E. Ruzicka, editor, *Structural Damping*, pages 49–88. ASME, New York, 1959.

[43] T. Ruiji. *Ultra Precision Coordinate Measuring Machine.* PhD thesis, Eindhoven University, The Netherlands, 2001.

[44] J.E. Ruzicka. Damping structural resosnances using viscoelastic shear-damping mechanisms. *Journal of Engineering for Industry*, B-83(4):414–424, 1961.

[45] R+W Coupling Technology, Bensenville, Illinois. *www.rw-america.com.*

[46] Spectral Dynamics, Inc., 1010 Timothy Dr., San Jose, CA 95133. *The STAR System Reference Manual.*

[47] B.F. Spencer, J.D. Carlson, M.K. Sain, and G. Yang. On the current status of magnetorheological dampers: Seismic protection of full-scale structures. In *Proceedings of the 1997 American Control Conference*, volume 1, pages 458–462, 1997.

[48] J.C. Sun, H.B. Sun, L.C. Chow, and E.J. Richards. Predictions of total loss factors of structures, Part II: Loss factors of sand-filled structure. *Journal of Sound and Vibration*, 104(2):243–257, 1986.

[49] S.P. Timoshenko and J.N. Goodier. *Theory of Elasticity.* McGraw-Hill, third edition, 1970.

[50] P.J. Torvik. The analysis and design of constrained layer damping treatments. In *Damping Applications for Vibration Control*, volume AMD-38. ASME, 1980.

[51] K.K. Varanasi. On the design of a precision machine for closed-loop performance. Master's thesis, Massachusetts Institute of Technology, Cambridge, Massachusetts, February 2002.

[52] K.K. Varanasi and S.A. Nayfeh. The dynamics of lead-screw drives: Low-order modeling and experiments. Accepted for publication in the *ASME Journal of Dynamic Systems, Measurement, and Control.*

[53] K.K. Varanasi and S.A. Nayfeh. Damping of flexural vibration using low-density foams and granular materials. In *DETC03, ASME Design Engineering Technical Conferences*, September 2003.

[54] K.K. Varanasi and S.A. Nayfeh. Vibration damping by coupling to lossy low-wave-speed media. In Agnes and Wang, editors, *Smart Structures and Materials 2003: Damping and Isolation*, volume 4697. SPIE, March 2003.